

FIRST PRINCIPLES STUDY OF SILICATE MINERALS

Thesis submitted for the degree of
Doctor of Philosophy (Science)

in

Physics (Theoretical)

by

Swastika Chatterjee

Department of Physics
University of Calcutta
August 2012

To my family

Acknowledgments

It has been five long years that I have spent at S. N. Bose Centre to pursue my PhD degree, and it is needless to say that there have been many a people who have helped and influenced me during this period.

The first name that comes to my mind is very obvious, and that is my supervisor, Tanusri Ma'am. When I look back into the years I spent with her, I find her like a guardian, helping and guiding us with a rather strict hand, with the sole aim of making us strong enough to face the outer scientific world. We as a group have been more than like a family, and today when I leave, I feel that I carry a part of her ideals with me. She has been a constant source of motivation and inspiration to our scientific work. Under her close observation and supervision I must say that I have evolved as a person. I would also like to thank my co-supervisor Prof. Surajit Sengupta, for helping me out with his supervision and brilliant ideas. I have hugely benefited from the scientific discussions that we have had from time to time over the past couple of years. I would also like to thank Prof. Sumit Chakraborty and Prof. Nibir Mondal for guiding us into the field of geology. I am specially grateful to Prof. Sumit Chakraborty for creating opportunities for me to discuss my PhD work at different universities/ institutes in Germany. It has been a great learning experience, which has enhanced my scientific knowledge and the discussions and feedbacks that I obtained from there have hugely motivated me to do further research in this field.

I am thankful to the office staffs of S. N. Bose, specially Mr. Sunish Deb, for their help at official/paper work, often at very short notices. I would also like to thank our system administrator Mr. Sudeep Narayan Bannerjee, for promptly taking care of all hardware and software related problems, so that our simulations ran smoothly.

When I joined the group under Tanusri Ma'am, I got Soumendu'da and Hena as my group senior, and Bodiur'da had just submitted his thesis. I am really blessed to have such seniors who have often gone out of their way to help me whenever I needed them. I am also deeply indebted to Mukul'da, who inspite of being physically far away, spent hours over the internet, often explaining some concept and at times trying to solve a problem. I would like to specially thank Soumyajit, who was my batch-mate here, for all the help he has extended to me from time to time. In addition to helping me out academically, he was always there to boost up my morale whenever I felt low. I would also like to thank my group-mates, Sudipta, Santu and Swarnakamal for all the scientific discussions which have greatly enriched my knowledge. I will cherish every moment spent with them all my life.

When I think of S. N. Bose, I feel life here would have been incomplete without a friend like Raka. She has been my critic and confidante, a person from whom I never hesitated to ask for help. I also made some great friends here in the form of Indrakshi, Rudranil and Sirshendu. They will always be a special part of my S. N. Bose memories. People generally say that PhD life is dull and colorless, but I am blessed to have friends like Kapil, Prashant, Abhinav, Jena'ji, Rajiv, Sujoy..... who have never, ever made me feel bored. I should specially thank Ambika P. Jena, whom we fondly called as 'our in-house system administrator', for taking care of all kinds of software related problem in our personal computers.

Lastly, I would like to thank my family. It is a very difficult task to pen down ones sense of gratitude towards ones parents and siblings, but one thing that I would like to say here is that, in this age where most parent wants his/her child to be either a doctor or an engineer, it has been my father who from

a very tender age motivated me to pursue higher studies in pure science. My mother too has been a constant source of inspiration. I am also thankful to my husband and in-laws for extending their support during the last part my tenure as a PhD student. Without their constant encouragement, it would have been difficult to complete my PhD smoothly. I would also like to thank my childhood (best) friend, Ishita Basu, who has helped me several times during my PhD.

Swastika Chatterjee
Kolkata, India
August, 2012

List of Publications

1. **S. Chatterjee**, T. Saha-Dasgupta, S. Sengupta, K. Chatterjee, N. Mondal
Site preference of Fe atoms in $FeMgSiO_4$ and $FeMgSi_2O_6$ studied by density functional calculation
Phys. Rev. B 79, 115103 (2009) *
2. **S. Chatterjee** and T. Saha-Dasgupta
First principles simulation of structural, electronic, and magnetic properties of vacancy bearing Fe silicates
Phys. Rev. B 81, 155105(2010).*
3. **S. Chatterjee**, S. Bhattacharyya, S. Sengupta, T. Saha-Dasgupta
Electronic structure of $FeCr_2S_4$: Evidence of Coulomb enhanced spin-orbit splitting
Physics and Chemistry of Minerals, v. 38, #4, 259-265 (2010) *
4. **S. Chatterjee** and T. Saha-Dasgupta
Electronic and Magnetic structure of the mixed-valence cobaltite $CaBaCo_4O_7$
Phys. Rev. B 82, 035108 (2011)
5. **S. Chatterjee**, T. Saha-Dasgupta and S. Sengupta
Visualizing frozen point defect tracks in Fe containing silicate minerals
Euro. Phys. Lett. 98, 29001 (2012) *

Contents

Table of Contents	ix
List of Figures	xi
List of Tables	xiv
1 Introduction	1
1.1 Structure of the Earth	2
1.2 Mineralogy of the Mantle	3
1.3 Overview of Thesis	8
2 Methodology	13
2.1 Electronic structure calculation	13
2.1.1 Many Body Hamiltonian	13
2.1.2 The Born Oppenheimer Approximation	14
2.1.3 The electronic problem and the one electron picture	15
2.1.4 Exchange correlation	23
2.1.4.1 Local density approximation	24
2.1.4.2 Generalized Gradient Approximation(GGA)	25
2.1.5 Basis set	26
2.1.5.1 Pseudopotential Method	27
2.1.5.2 Linear Muffin-Tin Orbital (LMTO) method	32
2.1.6 LDA+U method, missing correlation effect	38
2.1.7 Calculation of properties using DFT	42
2.1.7.1 Density of states and band structure	42
2.1.7.2 Total Energy	43
2.1.7.3 Vacancy Formation Energy	45
2.1.7.4 Calculation of barrier height using NEB method	46
2.2 The Monte-Carlo simulation technique	49
3 Site preference of Fe atoms in Olivine(FeMgSiO_4) and Pyroxene($\text{FeMg}(\text{SiO}_3)_2$) studied by density functional calculations	57
3.1 Introduction	58
3.2 Crystal structure	59
3.3 Results	61

3.3.1	Structural Optimization	61
3.3.2	Basic Electronic Structure	63
3.3.3	Total Energy Calculations - Site preference	65
3.3.4	Discussion	70
3.4	Conclusion	71
4	Crossover of cation partitioning in olivines : a combination of ab-initio and Monte carlo study	77
4.1	Introduction	77
4.2	Lattice Gas Model	80
4.3	Results	83
4.3.1	Variation in crystal structure of olivine with increasing temperature	83
4.3.2	Determination of the parameters of the model Hamiltonian from quantum mechanical total energy calculations	83
4.3.3	Determination of K_D value from MC simulation	86
4.4	Summary and Conclusions	88
5	First-principles Simulations of Structural, Electronic and Magnetic properties of vacancy bearing Fe silicates	93
5.1	Introduction	94
5.2	Results	95
5.2.1	Site preference of vacancy	95
5.2.2	Crystal structure of laihunite	96
5.2.3	Electronic and Magnetic Structure of fayalite with double vacancies at the metallic sites.	99
5.3	Conclusion	104
6	Vizualizing frozen point defect tracks in Fe containing olivines.	111
6.1	Introduction	112
6.2	Ab-initio Results	113
6.2.1	Vacancy formation energy at all cationic and anionic sites and its dependence on Fe-content	113
6.2.2	Relative site preference of Fe^{2+} , Fe^{3+} and Mg	115
6.2.3	Calculation of barrier potential	117
6.3	The 2D lattice gas model and the Monte-Carlo simulation.	119
6.4	Vizualization of vacancy track.	120
6.5	Summary and possible experimental verification	122
7	Conclusion and scope for future study.	127
7.1	Scope for future work	130

List of Figures

1.1	Interior of the Earth	1
1.2	Different ways in which the Si-O tetrahedral units are interconnected in minerals	4
1.3	An olivine crystal	6
1.4	A Pyroxene crystal	7
1.5	A Garnet crystal.	8
2.1	An illustration of Pauli's exclusion principle	23
2.2	A pictorial representation of the exchange-correlation hole	24
2.3	An illustration of the full all-electron wave-function and the corresponding potential along with the corresponding psedo-wavefunction and pseudo-potential plotted againts distance 'r' from the atomic nucleus.	30
2.4	Construction of Muffin Tin(MT) potential	33
2.5	The envelope of a MTO centered at R with its head in its own sphere at the centre and tails in the neighbouring two sphere.	35
2.6	The shifting of the occupied and unoccupied LDA orbitals with respect to each other due to presence of the U parameter.	40
2.7	A pictorial illustration of how NEB method is better than plain elastic band method in determination of the minimum energy path.	48
3.1	Buiding units of olivine and pyroxene	62

3.2	Complete lattice structure of olivine and pyroxene	62
3.3	Partial DOS of olivine and pyroxene	66
3.4	Comparison of total DOS for olivine and pyroxene	68
3.5	Charge density plot for olivine	69
4.1	Crystal structure of olivine projected onto bc plane	81
4.2	Schematic diagram of olivine involving the M-only lattice projected onto bc plane . . .	81
4.3	Temperature dependence of M1 and M2 octahedral volume as obtained by Redfern <i>et al.</i> and Heinemann <i>et al.</i>	84
4.4	A plot of difference in volume between M1 and M2 octahedra as a function of temperature	84
4.5	Four different configurations of the olivine crystal	85
4.6	Variation of h_s, J, J' as a function of temperature	86
4.7	Variation of $\ln K_D$ with inverse of Temperature (in K^{-1})	87
5.1	Schematic diagram showing the approximate hexagonal closed packing of oxygen atoms in case of fayalite and the total crystal structure of fayalite	97
5.2	Schematic diagram showing different configurations with all possible ways in which two vacancies can be created at the metallic sites in fayalite	98
5.3	Optimized structure of our theoretically developed laihunite crystal(configuration 1) . .	100
5.4	Partial DOS for configuration1	102
5.5	Charge density plot for configuration 1	104
5.6	[The two possible anti-ferromagnetic order in fayalite] The two possible anti-ferromagnetic order in fayalite. Solid lines show the intra-chain and dashed lines show the inter-chain interactions. Red (dark) and green (light) filled circles represent M1 and M2 sites. . . .	105

- 6.1 (Color online) Left panel: The vacancy formation energy at various cationic and anionic sites for iron-free as well iron-bearing olivines, measured with respect to that at M1 site. Black bar, dashed bar and cyan (light grey) bars represent iron-free olivine, iron bearing olivine with 25% Fe and with 50% Fe respectively. The inset shows the crystal structure of olivine, projected onto bc plane, with M1, M2, O1, O2, O3, Si sites marked. Right Panel: The vacancy formation energy at M1 site for various Fe concentrations of olivines. Inset shows the M-site only sublattice, with M1 (M2) sites marked as small (large) balls. 114
- 6.2 (Color online) Plot of magnetization density of olivine containing 37.5% of Fe (3 sites out of 8 M sites being occupied by Fe) and having a vacancy situated at the central M1 site of the lattice. Two of the M2 sites adjacent to vacancy as well as corner M1 sites are occupied by Fe, rest of the M sites being occupied by Mg. 114
- 6.3 The spin-polarized density of states projected onto d -states of the Fe atom sitting at the M2 site(solid line) and that projected onto d -states of the Fe atom sitting at M1 site(dashed line). The partial densities of states are calculated by projecting onto a sphere of radius 1.302 Å for both the Fe sites. 116
- 6.4 (Color online) Site preferences of Fe^{2+} -like and Fe^{3+} -like ions in olivine in presence of a single vacancy in the 4 f.u. unit cell. The vacant site is indicated by an empty circle, the Mg atoms by green (light grey), Fe^{3+} -like atoms by white and Fe^{2+} -like atoms by red (dark grey) balls. Left panel: Configurations with 2 Fe^{3+} -like ions at M2 (top) and M1 (bottom) sites. Middle panel: Configurations with 2 Fe^{3+} -like ions at M2 sites near (top) and far (bottom) to vacant site. Bottom panel: Configurations with 2 Fe^{3+} -like ions at M2 sites and a Fe^{2+} -like ion at M1 (top) and M2 site (bottom) site. The energy difference between bottom and top configurations are listed at the bottom of each panel. 118

- 6.5 Barrier height of vacancy propagation along [001] direction in a 50:50 Fe-Mg olivine, as obtained in a NEB calculation. The initial and final configurations are shown in left and hand insets, respectively. Various paths of vacancy propagation (except A and B which are perpendicular to the plane of the figure) are shown in the top inset. 119
- 6.6 (Color online) Snapshots of M-only lattice at two different MC step. Shown are only positions of wrong Fe sites. The region around the vacancy, marked with a box, is shown in the zoomed view with all M sites shown explicitly. The green and black balls denote positions of Mg and Fe²⁺ like ions at wrong (M2) sites, respectively. The red (dark grey) annular rings indicate Fe²⁺ like ions at M1 while the triangle and square indicate the positions of Fe³⁺ like ions and vacancy, respectively. Left panels: For perfectly ordered starting configuration. Right panels: Partially ordered starting configuration. 121

List of Tables

3.1	The Wykoff positions for each species in case of olivine.	61
3.2	Optimized structural parameters for olivine and pyroxene where all M1(M2) sites are occupied by Fe(Mg) and vice-versa in comparison to experimentally determined structure (data taken from ref 21 and 22). Lattice constants have been kept fixed at the experimental values.	64
3.3	LDA+U total energies for olivine and pyroxene with Fe atoms placed at the M1 sites and M2 sites respectively. Energy differences between the the two configurations are listed in the last row.	67
3.4	size and structural distortion of octahedral units	72
5.1	Energy required for creation of vacancy at different atomic sites of fayalite.	95
5.2	Total energies corresponding to the six different configurations with double vacancies created at M1 and M2 sites in fayalite as shown in Fig. 5.2.	99
5.3	The lattice constants and Wykoff positions for each species for Fayalite in orthorhombic space group and configuration 1 in triclinic space group.	100
5.4	Crystal structure data for configuration1.	101
5.5	Structural comparison between fayalite, laihunite and vacancy bearing fayalite in configuration 1(double vacancies at M1 sites).	101
5.6	Total energy of the three structures with double vacancies at M1 sites in the two types of possible anti-ferromagnetic configuration as shown in Fig. 5.2.	105

Chapter 1

Introduction

The evolution of the Earth in particular and the universe in general has fascinated human beings since ages. The study of material properties of the Earth dates back to around 300 B.C in ancient Greece. Since then attempt has been made to understand the physical processes happening inside and around the Earth. In the present thesis, we attempt on extending this knowledge using theoretical tools widely used in the physical sciences community.

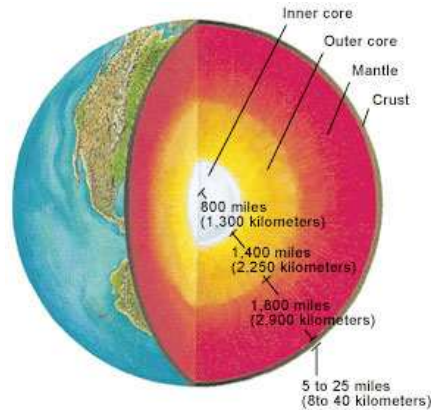


Figure 1.1 Interior of the Earth. Adapted from [1]

1.1 Structure of the Earth

The internal structure of the Earth is revealed primarily by compressional waves (primary waves or P waves) and shear waves (secondary or S waves) that pass through the planet in response to earthquakes. Seismic wave velocities vary with pressure(depth), temperature, mineralogy, chemical composition and degree of partial melting. Three first order seismic discontinuities divide the Earth into crust, mantle and core(see Fig. 1.1).

The major regions of the Earth can be summarized as follows:

1.**Crust**- Crust is the outermost solid shell of the Earth, which is chemically distinct from the underlying mantle. There are two different types of crust: thin oceanic crust that underlies the ocean basins and thicker continental crust that underlies the continents. These two different types of crust are made up of different types of rock. The thin oceanic crust is composed primarily of basalt and the thicker continental crust is composed primarily of granite. The low density of the thick continental crust allows it to "float" in high relief on the much higher density mantle below.

2. **Mantle** - Earth's mantle is believed to be composed mainly of olivine-rich rock. It has different temperatures at different depths. The temperature is lowest immediately beneath the crust and increases with increasing depth. The highest temperatures occur where the mantle material is in contact with the heat-producing core. This steady increase of temperature with depth is known as the geothermal gradient. The geothermal gradient is responsible for different rock behaviors and the different rock behaviors are used to divide the mantle into two different zones. Rocks in the upper mantle are cool and brittle, while rocks in the lower mantle are hot and soft (but not molten). Rocks in the upper mantle are brittle enough to break under stress and produce earthquakes. Rocks in the lower mantle, on the other hand, are soft and flow when subjected to forces instead of breaking. The lower limit of brittle behavior is the boundary between the upper and lower mantle.

3.**Core** - Earth's Core is composed mainly of iron and nickel alloy. This composition is assumed based upon calculations of its density and upon the fact that many meteorites (which are thought to be portions of the interior of a planetary body) are iron-nickel alloys. There are three main sources of heat

in the deep Earth: (1) heat from when the planet formed and accreted, which has not yet been lost; (2) frictional heating, caused by denser core material sinking to the center of the planet; and (3) heat from the decay of radioactive elements. Hence the core is the Earth's source of internal heat.

The core is divided into two different zones. The outer core is a liquid because the temperatures there are adequate to melt the iron-nickel alloy. However, the inner core is a solid even though its temperature is higher than the outer core. Here, tremendous pressure, produced by the weight of the overlying rocks is strong enough to crowd the atoms tightly together and prevents the liquid state.

In this thesis, we focus primarily on minerals found in the Earth's upper mantle.

1.2 Mineralogy of the Mantle

The silicate minerals make up the largest and most important class of rock-forming minerals in the mantle. Silicate rocks may belong to any of the three major classes: igneous (formed by cooling and solidification of magma or lava), sedimentary (formed by sedimentation of materials on the Earth's surface and beneath water) and metamorphic (formed due to transformation of an existing rock of any type).

All silicates have the following general features:

1. The SiO_4 tetrahedron invariably and inadvertently forms the basic structural unit among all silicates as shown in the centre of Fig. 1.2.

2. The different silicate types arise from the different ways in which the silicon-oxygen tetrahedra in a given structure are related to each other. The rule that the tetrahedra can share corners only, and not sides or edges has been found to be universally true, consequently two tetrahedra can have one oxygen in common between them. However every oxygen of a given tetrahedra may be shared with another tetrahedra.

3. Since the oxygen atoms are usually the largest in the structure as given by the ionic radii, these atoms are chiefly responsible for the size of the unit cell. From this it follows that the number of oxygen atoms in the silicate is highly important.

4. There are characteristic ways in which the tetrahedra have been found to combine in silicates, and these ways of linkages are comparatively few in number. If the tetrahedra are not combined to each other, the composition of the silicate is SiO_4 type, if all the corners are shared with other tetrahedra, the composition is SiO_2 type. Other relations yield intermediate type (see Fig. 1.2). The list is given below:

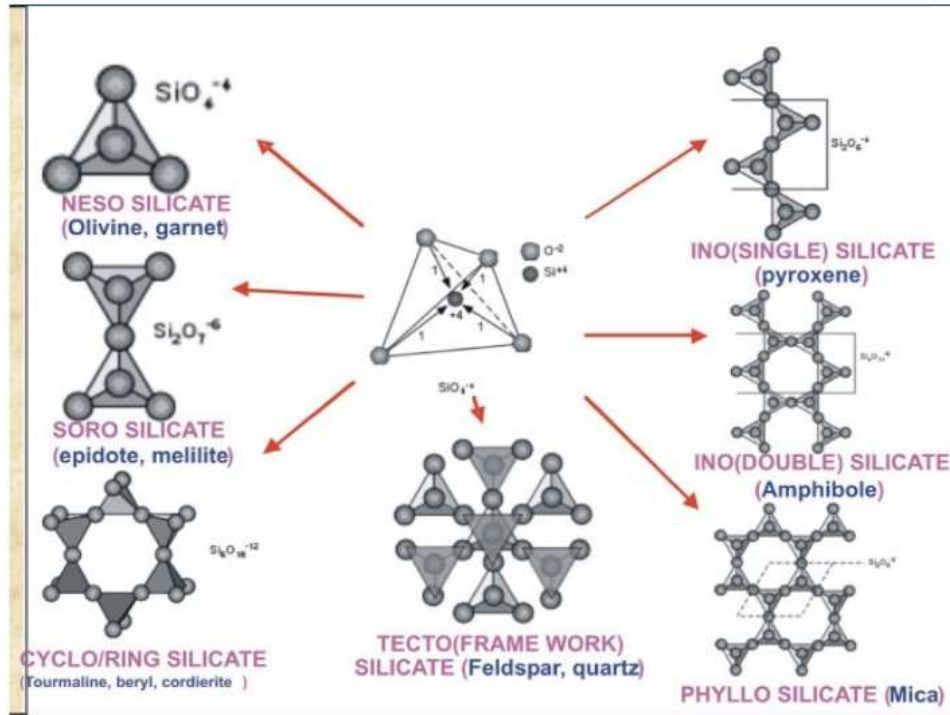


Figure 1.2 Different ways in which the Si-O tetrahedral units may be interconnected in minerals. [2]

(a) Three dimensional network (silica type) : All the tetrahedra share corners with other tetrahedra giving a three-dimensional network. Silica, in any of its modifications, belongs to the category of this linkage, which results in a composition of SiO_2 .

(b) The sheet structure(phylo-silicate) : This structure is obtained when tetrahedra are placed all in one plane with each tetrahedron being joined to other tetrahedra with three atoms lying in the common plane. An indefinite extension of this linkage produces a hexagonal network in the plane. The example

of silicate minerals with this structure is mica, with composition of Si_2O_5 .

(c1) The chain structure(Iono-silicate) : In this structure, SiO_4 tetrahedra join together to form chains of infinite extent. There are several modifications of this structure,yielding somewhat different compositions.(i) a single chain, one long linkage of tetrahedra of indefinite extent producing a composition of SiO_3 as in pyroxenes (ii) Di-silicate giving a composition of Si_4O_{11} as in the amphiboles. (iii) A sort of triple chain, with some modifications, yielding Si_3O_8 compositions.

(c2) Ring structure(Cyclo-silicate) : Two of the tetrahedral units are corner shared, as in the chains, but instead of extending indefinitely in one direction the chains make closed units of a ring like structure. Benitoite with Si_3O_9 ring and Beryl with Si_6O_{18} ring are typical examples.

(d) Double Tetrahedra structure(Soro-silicate) : These structures arise from two tetrahedra sharing a common oxygen between them. The resulting composition is Si_2O_7 and examples are thortvietite, melilite etc.

(e) Independent tetrahedral groups(Orthosilicate)- In this silicate type none of the tetrahedra shares corner with each other. The resultant composition is SiO_4 and the example is olivine.

The main minerals in the upper mantle are olivine, pyroxene and garnet. These minerals are only stable over a limited range of pressure and temperature. As pressure is increased the atoms re-arrange themselves and ultimately a new arrangement of atoms is energetically more favorable, usually with denser packing. The mineralogy of the mantle therefore changes with depth due to solid-solid phase changes. The elastic property and density of the mantle are primarily controlled by the proportions of the above minerals or their high pressure equivalents. To a lesser extent the properties depend on the composition of the individual minerals.

The following gives a brief description of the three most common minerals in the Earth's upper mantle:

Olivine - Olivine and its high pressure structural variants constitute over 50% of the Earth's upper mantle. It is one of Earth's most common mineral by volume. Olivine gets its name from its typical olive green color(see Fig. 1.3). In addition to being one of the most common mineral on the Earth's crust, it is also found in Mars, moon and meteorites. The spectral signature of olivines have been



Figure 1.3 Olivine crystal showing its characteristic olive green color.

found in the dust discs around young stars. Tails of comets also show spectral signature of olivine. Olivines have a general chemical formula M_2SiO_4 , where M refers to a metal cation such as Mg, Fe, Mn, Ni etc. As mentioned, they are neso-silicates, i.e, the SiO_4 tetrahedral units in the olivine crystal are isolated from each other. The most abundant olivines are magnesium-iron olivines where M cation is either Mg or Fe. The ratio of Mg and Fe varies between the two end members of the solid solution series: forsterite(Mg_2SiO_4) and fayalite(Fe_2SiO_4). Compositions of olivine are generally expressed in terms of molar fraction of forsterite and fayalite(eg, Fo70Fa30). Forsterite has a very high melting temperature ($1900^\circ C$), whereas fayalite has a comparatively lower melting temperature of $1200^\circ C$ at atmospheric pressure. Olivine incorporates very minor amount of other elements such as Ni, Ca etc. in addition to magnesium, iron, silicon and oxygen. They are found to occur in mafic and ultramafic igneous rocks and as a primary mineral in certain metamorphic rocks. Mg rich olivine crystallizes from magma that is rich in Mg and low in silica. Olivine and its high pressure structural variants constitute over 50% of the Earth's upper mantle, and olivine is one of Earth's most common mineral by volume. The metamorphosis of some sedimentary rocks(such as dolomite) high in Mg content also produce Mg-rich olivine or forsterite. Fe-rich olivine is comparatively less common, and occurs in igneous rocks in small amounts in rare granites and rhyolites(volcanic rock rich in silica(SiO_2) content) and extremely Fe-rich olivine can exist stably with quartz. In contrast Mg-rich olivines do not occur stably

with silica minerals. Mg-rich olivines are stable to a pressure upto 410 Km inside the Earth. Because it is thought to be the most abundant mineral in the Earth's mantle at the shallower depths, the properties of olivine have a dominant effect on the rheology of that part of the Earth, and hence on the solid flows that controls plate tectonics.

Pyroxene- The name pyroxene comes from the Greek words for fire (pyro) and stranger (xenos). Pyroxenes were named this way because of their presence in volcanic lavas. They are early-forming minerals that crystallized before the lava erupted (see Fig. 1.4). As mentioned before, pyroxenes are ionsilicates, i.e, chained silicates and may crystallize in both orthorhombic and monoclinic form. They are mostly found in igneous and metamorphic rocks. They have a general formula: $M_2(\text{SiO}_3)_2$, where M : Mg, Fe^{2+} , Ca, Na and rarely Zn, Mn, Li.



Figure 1.4 A Pyroxene crystal. The dark color shows higher Fe concentration.

Garnet - The name "garnet" comes from the 14th century Middle English word Garnet meaning 'dark red'(see Fig. 1.5). Garnet species are found in many colors including red, orange, yellow, green, blue, purple, brown, black, pink and colorless. They have been popularly used over ages as gem-stone and abrasive. Structurally they are neso-silicates, i.e, the SiO_4 tetrahedral units are completely isolated from each other, with a chemical formula $\text{X}_3\text{Y}_2(\text{SiO}_4)_3$ where X is usually occupied by divalent cations and Y is usually occupied by tri-valent cations.



Figure 1.5 A Garnet crystal.

1.3 Overview of Thesis

The aim of the present thesis is to study the structural, electronic, magnetic and mechanical properties of the olivine and pyroxene silicate minerals using ab-initio and classical simulation approach.

The following is an overview of the present thesis work:

- In the next chapter, the methodologies used for the present study have been elaborated on. It involved first-principles density functional calculations as well as Monte-Carlo simulation of the lattice gas model.
- Chapter 3 deals with the site preference of Fe in olivine and pyroxene. Olivines [7] and pyroxenes [4] have two in-equivalent octahedral sites M1 and M2, which are the contenders for hosting Fe ion. Our $T = 0K$ study in the total-energy-minimized structures indicate a strong preference for Fe to occupy M2 site in case of pyroxene and a preference for Fe to occupy M1 site in case of olivine. We provide the microscopic understanding of our finding in terms of density of states and charge densities.
- In Chapter 4, the effect of temperature on the site preference of Fe in olivine is discussed. It has long been debated among various experimental groups [5, 6, 7, 8, 9, 10, 11, 12, 13, 14, 15, 16, 17, 18] whether there is a cross-over of the cation partitioning beyond a certain temperature.

Here we present studies based on a combination of ab-initio electronic structure and classical Monte-Carlo(MC) techniques on this very problem of cross-over of cation partitioning in mixed Fe-Mg olivines. Our MC scheme uses interactions derived out of ab-initio density functional calculations carried out on experimentally reported crystal structure data. Our results show that there is no reversal of the preference of Fe for M1 over M2 as a function of temperature.

- In Chapter 5, our study on the structural, electronic and magnetic properties of vacancy bearing silicate mineral, Fe_2SiO_4 using first principle density functional theory(DFT) is presented. Our DFT simulated structure, which is compositionally close to naturally occurring Laihunite compound [20] shows good agreement in the general trend in the change of Fe_2SiO_4 crystal structure upon vacancy introduction. Our study shows that the introduction of vacancy creates charge disproportionation of Fe ions into Fe^{2+} -like and Fe^{3+} like ions with a charge difference larger than 0.5, keeping the valences of other ions unaltered. Fe^{2+} - like ions are found to occupy octahedral sites of specific symmetry while Fe^{3+} -like occupy the other leading to charge ordering at zero temperature. We have also studied the magnetic ordering of Fe ions.
- In Chapter 6, using a combination of First principles calculations and Monte Carlo simulations, we show that Fe containing silicates such as olivines naturally offer a way for visualizing tracks left by diffusing vacancies. Fe in its 2+ and 3+ valence states prefers two distinct cationic sites in the olivine structure. Vacancies formed at cationic M sites, cause neighboring Fe ions in their normally occurring Fe^{2+} state to change valency to Fe^{3+} , compensating for the charge imbalance and reducing energy costs, consequently altering the local site preference of Fe. Once the vacancy diffuses away, Fe atoms remain stuck in their meta-stable location producing a microscopic record of the vacancy's trajectory. Our results may be verified using high resolution transmission electron microscopy, combined with electron energy-loss spectroscopy.
- Chapter 7 includes summary and outlook of the present work.

Bibliography

- [1] T. H. Jordan, Proc. Natl. Acad. Sci. USA **76** No. 9, 4192-4200 (1979).
- [2] A. Putnis (1992) *An introduction to mineral sciences* Cambridge Univ Press, Cambridge.
- [3] S. A. T. Redfern *et al.* Phys. Chem. Miner, **27**, 630 (2000).
- [4] H. T. Evans, Jr., J. S. Huebner, and J. A. Konnert, Earth Planet. Sci. Lett. **37**, 476 (1978).
- [5] Y. A. Abdu, H. Annersten, T. Ericsson, F. C. Hawthorne Hyperfine Interact. **186**, 99-103 (2008).
- [6] G. Artioli, R. Rinaldi, C. C. Wilson, P. F. Zanazzi Am. Mineral. **80**, 197-200 (1995).
- [7] R. G. Burns Am. mineral. **55**, 1609 (1970).
- [8] W. Bush, S. S. Hafner, D. Virgo Nature(London) **227**, 339 (1970).
- [9] L. W. Finger Carnegie Inst. Wash. Year Book **69**, 302 (1971).
- [10] S. Ghose, C. Wan, I. S. McCallum Indian J. Earth. Sci. **3**, 1 (1976).
- [11] R. Heinemann, V. Staack, A. Fischer, H. Kroll, V. Thomas, A. Kirfel **84**, 1400-1405 (1999).
- [12] R. Heinemann, H. Kroll, F. Langenhorst, T. Lueder Eur. J. Mineral. **12**, 163-176 (2001).
- [13] R. Heinemann, H. Kroll, A. Kirfel, B. Barbier Eur. J. Mineral., **15**, Bh.1, 78 (2003) (in German).
- [14] R. Heinemann, H. Kroll, A. Kirfel, B. Barbier Eur. J. Mineral. **18**, 673-689 (2006).

- [15] M. Morozov, C. Brinkmann, W. Lottermoser, G. Tippet, G. Amthauer, H. Kroll H Eur. J. Mineral. **17**, 495-500 (2005).
- [16] S. A. T. Redfern, G. Artioli, R. Rinaldi, C. M. B. Henderson, K. S. Knight, B. J. Wood Phys. Chem. Minerals **27**, 630-637 (2000).
- [17] R. Rinaldi, C. C. Wilson Solid State Communications **97**, 395-400(1996).
- [18] R. Rinaldi, G. Artioli, C. C. Wilson, G. McIntyre Phys Chem Minerals **27**, 623-6(2000).
- [19] O. Tamada, B. Shen, N. Morimoto, Mineralogical Journal **11**, 382 (1983).

Chapter 2

Methodology

This chapter deals with the methodologies which form the basis of the computational techniques used in calculating various properties of the minerals presented in the thesis. The first section deals with the theoretical framework of our quantum mechanical calculations. This is followed by the details and theory behind our classical simulation approach used in this thesis.

2.1 Electronic structure calculation

2.1.1 Many Body Hamiltonian

Matter is made out of atoms, and the atoms in turn are made out of a positively charged nucleus and one or many negatively charged electrons, such that the net charge in the atom is zero. Matter hence, irrespective of its state(phase) or dimensionality, may be considered as a collection of interacting electrons and ions. The exact theory for such a system is based on solving the many-body Schrodinger equation of the form:

$$H\Psi(R_I, r_i) = E\Psi(R_I, r_i) \quad (2.1)$$

where:

E is the energy of the system, $\Psi(R_I, r_i)$ is the many body wave-function that describes the state of the

system, R_I are the positions of ions, r_i are the variables that describe the position of the electrons and the Hamiltonian H is defined as follows:

$$H = T_n + T_e + V_{mn} + V_{ne} + U_{ee} \quad (2.2)$$

Here T_n and T_e represent the kinetic energy operators for the nuclei and electrons respectively.

$$T_n = -\sum_I \frac{\hbar^2}{2M_I} \nabla_{R_I}^2 ; \quad T_e = -\sum_i \frac{\hbar^2}{2m_e} \nabla_{r_i}^2 \quad (2.3)$$

m_I - mass of ions and m_e - mass of electrons.

V_{mn} represents the repulsive interaction between two ions positioned at R_I and R_J .

$$V_{mn} = \frac{Z_I Z_J e^2}{|R_I - R_J|} \quad (2.4)$$

V_{ne} represents the attractive interaction between an ion at R_I and an electron at r

$$V_{ne} = -\frac{Z_I e^2}{|R_I - r|} \quad (2.5)$$

V_{ee} is the repulsive interaction between two electrons at r_i and r_j respectively.

$$V_{ee} = \frac{e^2}{r_i - r_j} \quad (2.6)$$

The above described Hamiltonian though exact in nature, is impossible to solve as many degrees of freedom are involved. This calls for the need for approximation.

2.1.2 The Born Oppenheimer Approximation

Since the nuclei are massive in size as compared to the electrons, we can consider the ions to move slowly in space and the electrons responding instantaneously to its motion. Hence the motion of the ions and electrons can be separated and this is what is implied by Born-Oppenheimer approximation [1]. This can be mathematically formulated as :

$$\Psi(R_I, r_i, t) = \sum_n \Theta_n(R, t) \Phi_n(R, r) \quad (2.7)$$

here $\Theta(R, t)$ describes the evolution of the nuclear sub-system and $\Phi(R, r)$ are the electronic eigenstates which satisfy the time-independent Schrodinger equation, given by :

$$h_e \Phi(R, r) = E_n(R) \Phi_n(R, r) \quad (2.8)$$

where the electronic Hamiltonian

$$h_e = T_e + V_{ne} + U_{ee} = H - T_n - V_{nn} \quad (2.9)$$

Hence, to summarize, within this approximation, the Ψ would have an explicit dependence on the electronic degrees of freedom and the nuclei may be considered frozen in space.

2.1.3 The electronic problem and the one electron picture

If one can solve the Schrodinger equation to obtain the wave function $\Phi(R, r)$, then this wave function can in turn be used to calculate various properties of the system. But the main problem that one faces is the difficulty in solving the Schrodinger equation. Exact analytical solution of the Schrodinger equation has been obtained for very few simple systems. On the other hand, the main difficulty with numerical solutions comes from the number of variables that one needs to handle. There are $3N$ variable for a wavefunction $\Psi(r_1, r_2, \dots, r_N)$. Hence, a full specification of a single wave-function of neutral Fe is a function of seventy-eight variables. If we want to tabulate (in a rather crude way) this function at 10 different values, the full tabulation would require 10^{78} entries. Undertaking such a huge calculation is rather impossible. One therefore needs to resort to further approximations. Two different classes of approximations/methods are carried out in this direction.

One class of methods is the wave-function based formalism, as proposed by Hartree and Hartree-Fock [2]. In the Hartree method, the basic assumption is that the many-electron wave-function can be written as a product of one electron orbitals. On the other hand in the Hartree-Fock formalism a comparatively more complicated wave-function obeying the Pauli's exclusion principle is employed. In both these methods, the energy E , given by:

$$\tilde{E} = \langle \tilde{\Psi} | H | \tilde{\Psi} \rangle \quad (2.10)$$

is variationally minimized using the corresponding wave-functions.

In the second approach the properties of many-electron system are assumed to be determined using the spatially dependent electronic densities. One of the earliest tractable density functional schemes for solving the many-electron problem was proposed by Thomas and Fermi(1927) [3] prior to Hartree(1928) and Hartree-Fock(1930) theories. In this model, the electron density of non-interacting homogeneous gas is the central variable. But it suffered from various drawbacks. The largest source of error was in the representation of kinetic energy, followed by the errors in exchange energy, and the error incorporated due to the complete neglect of electron correlation. It did not predict bonding between atoms, so molecules and solids cannot form in this theory.

Much later, in 1964 Hohenberg and Kohn [4] proved that it was indeed possible to develop an exact theory for many particle systems in terms of ground state single particle density alone. They proposed two remarkably strong theorems:

Theorem1 : There is a one-to-one correspondence between the ground state density of a N electron system and the external potential acting on it.

Theorem2 : The density that minimizes the total energy is the exact ground state density.

But, the Hohenberg-Kohn theorems did not offer a way of computing ground state density of a system in practice. This was done a year later by Kohn and Sham (1965) [5]. Their formulation centres on mapping the interacting system with real potentials onto a fictitious system whereby the electrons move with in an effective single particle potential.

The mathematical details are presented in the following.

The one-body electron-ion interaction term " V_{ne} " can be written as follows:

$$= \int \Psi^*(r_1, r_2, \dots, r_N) \sum_i V(r_i) \Psi(r_1, r_2, \dots, r_N) dr_1 dr_2 \dots dr_N \quad (2.11)$$

$$= N \int dr_1 V(r_1) \int \Psi^*(r_1, r_2, \dots, r_N) \Psi(r_1, r_2, \dots, r_N) dr_2 dr_3 \dots dr_N \quad (2.12)$$

$$\text{Hence } V_{ne} = \langle \Psi | \sum_i V(r_i) | \Psi \rangle = \int d^3r V(r) \rho(r)$$

where $\rho(r)$ is the probability density for finding an electron in a small volume d^3r around the point r and is mathematically represented as:

$$\rho(r_1) = N \int \Psi^*(r_1, r_2, \dots, r_N) \Psi(r_1, r_2, \dots, r_N) dr_2 \dots dr_N \quad (2.13)$$

Similarly, the two body potential term, i.e, the electron-electron repulsion term can be written as follows:

$$V_{ee} = \left\langle \Psi \left| \frac{1}{2} \sum_{ij} \frac{1}{r_{ij}} \right| \Psi \right\rangle = \frac{1}{2} \int d^3r_1 d^3r_2 \Gamma(r_1, r_2) / r_{12} \quad (2.14)$$

where $\Gamma(r_1, r_2)$ is the joint probability of finding one electron in a volume d^3r_1 around r_1 and another in d^3r_2 at r_2 , and is mathematically represented as:

$$\Gamma(r_1, r_2) = N(N-1) \int \Psi^*(r_1, r_2, \dots, r_N) \Psi(r_1, r_2, \dots, r_N) d^3r_3 \dots d^3r_N \quad (2.15)$$

The kinetic energy term that involves differential operator can be written as :

$$T = - \left\langle \Psi \left| \frac{1}{2} \sum_i \nabla_i^2 \right| \Psi \right\rangle \quad (2.16)$$

$$= - \frac{N}{2} \int \Psi^*(r_1, r_2, \dots, r_N) \nabla_1^2 \Psi(r_1, r_2, \dots, r_N) d^3r_1 d^3r_2 \dots d^3r_N \quad (2.17)$$

$$= - \frac{N}{2} \int [\nabla_1^2 \Psi^*(r'_1, \dots, r_N) \Psi(r_1, \dots, r_N)]_{r_1=r'_1} d^3r_1 \dots d^3r_N \quad (2.18)$$

$$= - \frac{1}{2} \int d^3r_1 [\nabla_1^2 \gamma(r_1, r'_1)]_{r_1=r'_1} \quad (2.19)$$

Here $\gamma(r_1, r'_1)$ is the first order reduced density matrix, defines as :

$$\gamma(r_1, r'_1) = N \int \Psi_*(r'_1, r_2, \dots, r_N) \Psi(r_1, r_2, \dots, r_N) d^3 r_2 \dots d^3 r_N \quad (2.20)$$

The total energy can be expressed in terms of the reduced density matrices :

$$E[\rho, \gamma, \Gamma] = T[\gamma(r_1, r'_1)] + V_{ne}[\rho(r)] + V_{ee}[\Gamma(r_1, r_2)] + V_{nn} \quad (2.21)$$

Which leads to the possibility of developing a quantum mechanics of a many electron system in terms of the reduced density matrices bypassing the wave-function. This problem has to be solved by imposing necessary and sufficient conditions on $\gamma(r_1, r'_1)$ and $\Gamma(r_1, r_2)$, which are unfortunately not known. The conditions on $\rho(r)$ are however known. The theory as reformulated by Levy(1982) [6] demands that the ground state density ($\rho(r)$) is non-negative and is obtained from antisymmetric wave-function and it satisfies the condition :

$$\int \rho(r) dr = N \quad (2.22)$$

This is known as the N-representability problem. This makes the single particle density a promising candidate for the formulation of quantum mechanics.

Mathematical proof of Hohenberg Kohn Theorem : Consider the ground states of two N-electron systems characterized by two external potentials $v_1(r)$ and $v_2(r)$ with the corresponding Hamiltonians and the Schrodinger equations given by :

$$H_1 = T + U + \sum_i v_1(r_i) \quad (2.23)$$

$$H_2 = T + U + \sum_i v_2(r_i) \quad (2.24)$$

Here:

$$T = -\frac{1}{2} \sum_{i=1}^N \nabla_i^2 \quad (2.25)$$

and

$$U = \frac{1}{2} \sum_{i \neq j} \frac{1}{r_{ij}} \quad (2.26)$$

Hence, H_1 and H_2 operating respectively on Ψ_1 and Ψ_2 yield the energy eigen-values E_1 and E_2 respectively as given by :

$$H_1 \Psi_1 = E_1 \Psi_1 \quad (2.27)$$

and

$$H_2 \Psi_2 = E_2 \Psi_2 \quad (2.28)$$

We assume that the two wave-functions yield the same density via the equation:

$$\rho(r_1) = N \int \Psi_{1/2}^*(r_1, r_2, \dots, r_N) \Psi_{1/2}(r_1, r_2, \dots, r_N) dr_2 dr_3 \dots dr_N \quad (2.29)$$

One can use the variational principle and write the energy :

$$E_1 = \langle \Psi_1 | H_1 | \Psi_1 \rangle \quad (2.30)$$

$$\langle \Psi_2 | H_1 | \Psi_2 \rangle = \langle \Psi_2 | H_2 | \Psi_2 \rangle + \langle \Psi_2 | H_1 - H_2 | \Psi_2 \rangle \quad (2.31)$$

Hence,

$$E_1 < E_2 + \int dr \rho(r) [v_1(r) - v_2(r)] \quad (2.32)$$

On interchanging suffixes :

$$E_2 < E_1 + \int dr \rho(r) [v_2(r) - v_1(r)] \quad (2.33)$$

Summation of the inequalities leads to the contradiction:

$$E_1 + E_2 < E_2 + E_1 \quad (2.34)$$

Hence, the assumption of identical density arising from two different external potentials is wrong and a given $\rho(r)$ can correspond to only one $v(r)$. Now, since $v(r)$ is fixed, the Hamiltonian and hence the wavefunction are fixed by the density. The wave-function being a functional of density, the energy functional for a given external potential $v(r)$ is a unique functional of density. This functional assumes a minimum value for the true density.

Kohn Sham Equation : The minimization of $E_v[\rho]$ subject to the constraint of normalized density :

$$\rho(r)dr = N \quad (2.35)$$

leads to the Euler equation for the direct calculation of density :

$$\delta[E_v[\rho] - \mu[\int \rho(r)dr - N]] = 0 \quad (2.36)$$

$$\frac{\delta E}{\delta \rho} - \mu = 0 \Rightarrow \mu = \frac{\delta E}{\delta \rho} = v(r) + \frac{\delta F}{\delta \rho} \quad (2.37)$$

The crux of the problem is to obtain an expression for the energy functional in terms of density which has the general form :

$$E_v[\rho] = \int v(r)\rho(r)dr + F[\rho] \quad (2.38)$$

Comparing with the energy functional in terms of the reduced density matrices :

$$E_v[\rho, \gamma, \Gamma] = T[\gamma] + \int v(r)\rho(r)dr + \frac{1}{2} \int \int \frac{\Gamma(r_1, r_2)}{r_{12}} dr_1 dr_2 \quad (2.39)$$

and using the decomposition :

$$\Gamma(r_1, r_2) = \rho(r_1)\rho(r_2)[1 - f(r_1, r_2)] \quad (2.40)$$

where $f(r_1, r_2)$ is the correlation functional, one can separate out from the electron-electron repulsion term $V_{ee}[\rho]$, the Hartree contribution:

$$E_H[\rho] = \frac{1}{2} \int \int \frac{\rho(r_1)\rho(r_2)}{r_{12}} dr_1 dr_2 \quad (2.41)$$

The exact kinetic energy functional $T[\rho]$ is usually replaced by the kinetic energy of a system of non-interacting particles, $T_0[\rho]$ and the contribution $V_{ee}[\rho] - E_H[\rho]$ together with $T[\rho] - T_0[\rho]$ constitute what is known as the exchange-correlation (XC) energy functional $E_{XC}[\rho]$. This is unknown. Thus one can write:

$$E_V[\rho] = T_0[\rho] + \int v(r)\rho(r)dr + E_H[\rho] + \{T - T_0(\rho) + V_{ee} - E_H[\rho]\} \quad (2.42)$$

$$= T_0[\rho] + \int v(r)\rho(r)dr + E_H[\rho] + E_{XC}[\rho] \quad (2.43)$$

The scheme for obtaining the non-interacting kinetic energy functional $T_0[\rho]$ for a certain $\rho(r)$ is through the solution of the one particle Schrodinger equation:

$$\left[-\frac{1}{2}\nabla^2 + \lambda(r) \right] \Psi_i = \varepsilon_i \Psi_i \quad (2.44)$$

For a suitably chosen $\lambda(r)$ such that the resulting orbitals yield the density as:

$$\rho(r) = \sum_i |\Psi_i|^2 \quad (2.45)$$

And then evaluating the functional as:

$$T_0[\rho] = \sum_i \varepsilon_i - \int dr \lambda(r) \rho(r) \quad (2.46)$$

The energy functional that is to be minimized for determining the correct equilibrium density is then given by:

$$E_V[\rho] = \sum_i \varepsilon_i - \int dr \lambda(r) \rho(r) + \int v(r)\rho(r)dr + E_H[\rho] + E_{XC}[\rho] \quad (2.47)$$

which leads to the variational condition:

$$\delta E_V[\rho] = 0 \quad (2.48)$$

$$= \sum_i \delta \varepsilon_i - \int dr \delta \lambda(r) \rho(r) + \int dr \delta \rho(r) \left[-\lambda(r) + v(r) + \frac{\delta E_H}{\delta \rho(r)} + \frac{\delta E_{XC}}{\delta \rho(r)} \right] \quad (2.49)$$

Now since :

$$\varepsilon_i = - \left\langle \Psi_i \left| \frac{1}{2} \nabla_i^2 \right| \Psi_i \right\rangle + \langle \Psi_i | \lambda(r) | \Psi_i \rangle \quad (2.50)$$

One has:

$$\delta \varepsilon_i = - \left\langle \delta \Psi_i \left| \frac{1}{2} \nabla_i^2 \right| \Psi_i \right\rangle + \langle \delta \Psi_i | \lambda(r) | \Psi_i \rangle + c.c. + \langle \Psi_i | \delta \lambda(r) | \Psi_i \rangle \quad (2.51)$$

$$= \varepsilon_i \delta \langle \Psi_i | \Psi_i \rangle (= 0) + \langle \Psi_i | \delta \lambda(r) | \Psi_i \rangle \quad (2.52)$$

And hence the result:

$$\sum_i \delta \varepsilon_i = \int dr \rho(r) \delta \lambda(r) \quad (2.53)$$

which in combination with variational condition leads to the result:

$$\delta E_V[\rho] = 0 = \int dr \rho(r) \left[-\lambda(r) + v(r) + \frac{\delta E_H}{\delta \rho(r)} + \frac{E_{XC}}{\delta \rho(r)} \right] \quad (2.54)$$

Since the variation in $\delta \rho(r)$ is arbitrary:

$$\lambda(r) = v(r) + \frac{\delta E_H}{\delta \rho(r)} + \frac{\delta E_{XC}}{\delta \rho(r)} \quad (2.55)$$

This clearly shows that if one chooses $\lambda(r)$ given by this expression, the single particle Schrodinger equation leads to the correct density for the system. This provide the basis for Kohn-Sham density functional scheme which involves the solution of the following N such differential equation:

$$\left[-\frac{1}{2} \nabla^2 + V_{eff}(r; \rho) \right] \Psi_i = \varepsilon_i \Psi_i \quad (2.56)$$

With the effective potential given by:

$$V_{eff}(r) = V(R) + \int \frac{\rho(r')}{|r-r'|} dr + \frac{\delta E_{XC}}{\delta \rho(r)} \quad (2.57)$$

And the density is calculated as:

$$\rho(r) = \sum_i |\Psi|^2 \quad (2.58)$$

The energy functional in this theory is calculated as:

$$E_V[\rho] = \sum_i \varepsilon_i - \frac{1}{2} \int \int \frac{\rho(r)\rho(r')}{|r-r'|} dr dr' + E_{XC}[\rho] - \int dr \rho(r) \frac{\delta E_{XC}}{\delta \rho(r)} \quad (2.59)$$

2.1.4 Exchange correlation

Apart from the exchange-correlation term E_{XC} , all other terms in the many body Hamiltonian can be exactly determined in terms of the single particle density. But before we delve further into the various ways of obtaining a good approximate value of this functional, it would be worthwhile to discuss as to what exchange and correlation physically mean.

To understand exchange, let us imagine that there is a up-spin electron at r_0 . Pauli's exclusion principle forbids the presence of electrons with spin up at the same position co-ordinate r_0 (see Fig. 2.1), whereas a down spin electron is free to sit there. This function can be calculated exactly, although it involves calculation of expensive integrals. In the Hartree-Fock scheme, which employs a many-body wave-function of the Slater determinant form, the exchange energy is calculated exactly. But here the correlation energy is completely neglected.



Figure 2.1 According to Pauli's exclusion principle, the situation as showed in figure (a), where two electrons of the same spin occupies the same quantum state is not allowed. Whereas, as shown in (b), two electrons of opposite spin are allowed to occupy the same quantum state.

Correlation, on the other hand is representative of the exclusion zone that an electron creates around itself, where it discourages the presence any other electron(see Fig. 2.2). The origin of this correlation energy is completely coulombic. In general this exclusion zone, which is also known as a correlation hole is not generally spherically symmetric, unless for homogeneous jellium model.

Now, since correlation can not be calculated exactly, one has to resort to approximate forms. The exchange part which can otherwise be calculated accurately is also approximated with an expectation that it would be able compensate for any error that might have crept in because of approximating the correlation term. Hence, one looks for an approximation for the sum of the two terms $E_X + E_C = E_{XC}$, where both exchange and correlation are treated on the same level of accuracy and approximation.

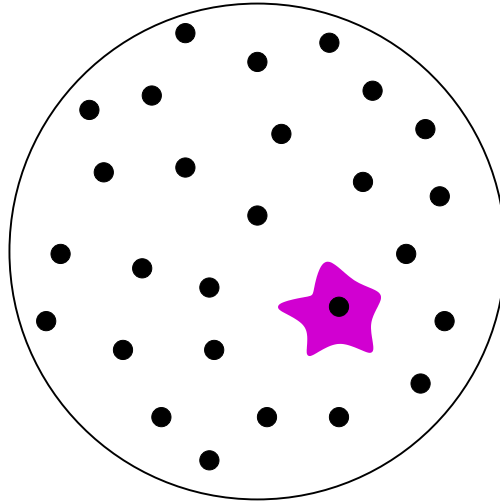


Figure 2.2 The black dots in the figure represent the sea of electrons in a piece of material, the shaded (pink) area described around one such black dot is a pictorial representation of the exclusion zone that is created around an electron due to electron-electron correlation.

There are many approximate models available for this purpose. Two of the most common are the local density approximation and the generalized gradient approximation.

2.1.4.1 Local density approximation

This is one of the most widely used approximation for estimating the exchange-correlation energy. It was proposed by Kohn and Sham in their 1965 paper [5], although the very idea existed primarily in the theory by Thomas-Fermi-Dirac [7]. The main idea employed here is to consider a generally inhomogeneous electron gas to be locally homogeneous and use the exchange-correlation hole for the homogeneous electron gas, which can be calculated to a very high degree of accuracy. One can now write the exchange-correlation energy as the average of an energy density $\epsilon_{XC}^{LDA}[\rho]$

$$\tilde{E}_{XC}^{LDA} = \int \rho(r) \tilde{\epsilon}_{XC}^{LDA}[\rho(r)] dr \quad (2.60)$$

where $\tilde{\epsilon}_{XC}^{LDA}[\rho] = \epsilon_X^{LDA}[\rho] + \epsilon_C^{LDA}[\rho]$

The exchange energy is exactly given by Dirac's expression:

$$\varepsilon_X[\rho] = -\frac{3}{4}\left(\frac{3}{\pi}\right)^{1/3} \rho^{1/3} = -\frac{3}{4}\left(\frac{9}{4\pi^2}\right)^{1/3} \frac{1}{r_s} = -\frac{0.458}{r_s} a.u. \quad (2.61)$$

Here $r_s = (3/4\pi\rho)^{1/3}$ and is the mean inter-nuclear distance.

There are many good approximations for correlation that have been proposed. The most accurate results are given by quantum Monte-Carlo simulations by Ceperly and Alder(1980)[8]. This correlation functional as obtained by Ceperly and Alder is exact within numerical accuracy and has been parametrized by Perdew and Zunger(1981)[9].

For dealing with magnetic systems, the LDA is extended to a spin-polarized system, and is named as the local spin density approximation(LSDA). Here the exchange correlation energy density is written in terms of the up $\rho_\uparrow(r)$ and down $\rho_\downarrow(r)$ spin densities.

$$E_{XC}^{LSDA}[\rho_\uparrow(r), \rho_\downarrow(r)] = \int [\rho_\uparrow(r) + \rho_\downarrow(r)] \varepsilon_{XC}[\rho_\uparrow(r), \rho_\downarrow(r)] dr \quad (2.62)$$

Although, LDA apparently seems to be a huge and drastic approximation as compared to the real systems of interest, but it is known to be very successful and has been shown to produce robust and consistent results in a variety of systems. The main reason behind it lies in the fact that the exchange-correlation energy does not depend on the shape, but the size of the exchange correlation hole, i.e, the spherical average of the hole. Furthermore, LDA satisfies the sum rule, wherein the exchange-correlation hole contains exactly one displaced electron.

LDA gives best estimates of various properties when the electronic densities are close to homogeneity. It tends to overestimate the binding energy of molecules and the cohesive energy of solids, but the trends shown are very good. LDA is able to reproduce well the bond length, bond angle and vibrational frequencies with small deviations. In general LDA overbinds and hence bond lengths are underestimated. Elastic constants and phonon frequencies are also well reproduced with some underestimation. Dielectric constants and piezoelectric co-efficients are generally over-estimated.

2.1.4.2 Generalized Gradient Approximation(GGA)

In the generalized gradient approximation, the functional depends on the density and its gradient.

$$E_{XC}^{GGA}[\rho] = \int \rho(r) \varepsilon_{XC}(\rho(r), |\nabla\rho(r)|) dr \quad (2.63)$$

Several GGA functionals like Perdew-Wang 1991 [10] and Perdew, Burke and Ernzerhof [PBE] [11] are the most popular. In comparison to LDA, GGA's tend to improve total energies, atomization energies, energy barriers and structural energy differences [11]. GGA expands and softens bands, an effect that sometimes corrects and sometimes over-corrects the LDA prediction.

2.1.5 Basis set

Basis sets are the foundation of modern electronic structure theory. In order to solve the eigenvalue problem as already stated, the eigenstates Φ_i , which are the single particle wave-functions, must be expanded in terms of any converged basis set. Depending on the choice of basis functions, different schemes can be broadly grouped into two categories:

(i) Fixed basis set method : The wave-function is determined as an expansion in some set of fixed basis functions, like linear combination of atomic orbitals(LCAO)[12], plane waves, Gaussian orbitals etc. Here one has to solve the eigenvalue problem:

$$(H - \varepsilon O).b = 0 \quad (2.64)$$

involving the Hamiltonian H and overlap matrix O, to determine the eigenvalues ε and the expansion coefficients b.

This method is computationally simple but the disadvantage is that the basis set may be large to be reasonably complete.

Most of the fixed basis set uses pseudopotential for the electron-ion interaction, where localized core states are removed by replacing the strong crystalline potential by a weak pseudopotential, while giving faithful determination of the valence and conduction bands. Pseudopotential in conjunction with plane wave basis has become one of the most versatile and efficient approaches for calculating electronic properties.

(ii) Partial Wave method : The wave-function is expanded in a set of energy and potential dependent partial waves like the cellular method [13], the augmented plane wave method [14] and the Korringa-Kohn-Rostoker method [15]. One has to solve set of equations of the form :

$$M(\epsilon).b = 0 \quad (2.65)$$

In contrast to Eqn.2.64 which is a polynomial in ϵ , the Eqn.2.65 has a complicated non-linear energy dependence. We have no a priori idea how many roots we expect, nor whether all roots are physically permissible. The partial wave methods though complicated to solve, do have advantages. Firstly, they provide solutions of arbitrary accuracy for a muffin-tin potential and for closed packed systems, this makes them far more accurate than the traditional fixed basis methods. Secondly, the information about the potential enters only via a few functions of energy. However as already stated, it has the disadvantage of being computationally heavy, the eigen energy ϵ_j must be found individually by tracing the roots of the determinant of M as a function of ϵ . To overcome this, Andersen (1975) first proposed a unified approach for linear methods [25] such as linear augmented plane wave (LAPW) and linear muffin-tin orbital (LMTO) methods which are the linearized versions of APW and KKR methods, respectively. These methods therefore lead to secular equations like Eqn.2.64 rather than Eqn.2.65 and combine the desirable features of the fixed basis and partial wave methods.

In this thesis, we use pseudopotential method along with plane wave basis, as implemented in the Vienna ab initio simulation package (VASP) [26], to obtain very accurate total energies for various systems. We have also extensively used the LMTO method to investigate electronic structure properties of the systems studied. Therefore, in the following two subsections, we discuss the pseudopotential method and LMTO method in greater details.

2.1.5.1 Pseudopotential Method

In solving the Schrodinger equation for condensed aggregates of atoms, space can be divided into two regions, with quite different properties. The regions near the nuclei, called the core region, are composed primarily of tightly bound core electrons, whose wave-functions are well localized, while the

remaining volume contains the valence electrons which are involved in the binding together of atoms. These valence electrons may be found with appreciable probability in the interstitial regions, where their wave-functions can be described with a few number of plane waves. But the main problem with describing the valence electronic wave-function with a small number plane waves is that this would fail badly in reproducing the highly oscillating behavior of these valence wave-functions near the core region. These heavy oscillations occur because the valence wavefunctions are orthogonal to those of the core, which produces a large kinetic energy for the valence electrons in the core regions. In order to solve this problem, Herring in 1940 [18] proposed the Orthogonalized plane wave [OPW] method, where he constructed valence wave functions from a linear combination of plane waves and core states such that they were orthogonalized to the core. The pseudopotential method, which will be discussed in details here originated from of this OPW method. Here, going a step ahead, the core states were altogether eliminated, by replacing their action by an effective potential called the pseudopotential. It needs to be constructed carefully, so that it is able to reproduce the bonding properties of the actual potential accurately.

In the following, we will develop the basic concept of OPW method followed by the pseudopotential method for an atom where core and valence states are denoted by the subscript c and v respectively. The orthogonalized plane wave can be represented as follows:

$$\phi_k = e^{ik \cdot r} + \sum_c b_c \Psi_k^c(r) \quad (2.66)$$

constant b_c is determined by requiring ϕ_k be orthogonal to the core:

$$\int dr \Psi_k^{c*}(r) \phi_k(r) = 0 \quad (2.67)$$

Hence, the wave function for the system may written as a linear combination of the OPWs:

$$\Psi_k = \sum_k c_k \phi_{k+K} \quad (2.68)$$

By explicit construction, the wave-functions are made orthonormal to the core and hence it also

has the expected rapid oscillations at the core. Moreover, this wave-function is plane wave like in the interstitial region where the contribution from second term of Eqn 2.66, involving the core wave function Ψ_k^c , has very little contribution.

This gives, a very basic idea of OPWs. With this background, will go further and develop the pseudopotential method. Let ϕ_k^v be the plane wave part of the wave-function :

$$\phi_k^v(r) = \sum_k C_k e^{i(k+K).r} \quad (2.69)$$

Hence, using Eqn.2.66, we can write :

$$\Psi_k^v(r) = \phi_k^v(r) - \sum_c \left(\int dr' \Psi_k^{c*}(r') \phi_k^v(r') \right) \Psi_k^c(r) \quad (2.70)$$

Since Ψ_k^v is an exact valence wavefunction, it should satisfy the Schrodinger equation:

$$H\Psi_k^v = \varepsilon_k^v \Psi_k^v \quad (2.71)$$

Substituting Eqn.2.70 in Eqn.2.71 and using

$$H\Psi_k^c = \varepsilon_k^c \Psi_k^c \quad (2.72)$$

and

$$V^R \Psi = \sum_c (\varepsilon_k^v - \varepsilon_k^c) \left(\int dr' \Psi_k^{c*}(r') \Psi(r') \right) \Psi_k^c \quad (2.73)$$

we obtain :

$$(H + V^R) \phi_k^v = \varepsilon_k^v \phi_k^v \quad (2.74)$$

which leads to a Schrodinger equation satisfied by ϕ_k^v

The pseudopotential is defined as :

$$H + V^R = -\frac{\hbar^2}{2m} \nabla^2 + V^{pseudo} \quad (2.75)$$

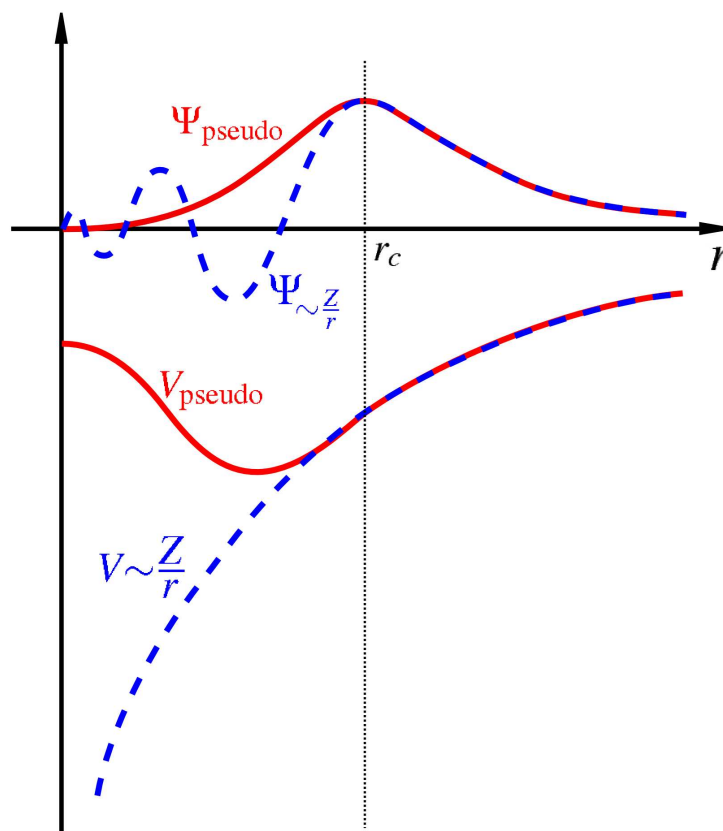


Figure 2.3 An illustration of the full all-electron wave-function and the electronic potential (solid lines) plotted against distance r , from the atomic nucleus. The corresponding pseudo-wavefunction and the potential is plotted in dotted lines. Outside a given radius r_c , the all-electron and the pseudo-electron values match. This figure is adapted from [21].

The pseudo-potential represents a weak attractive potential, as is obtained by a balance between the attractive potential and the repulsive potential V^R , as shown in Fig.2.3. The new states ϕ^v obey a single-particle equation with a modified potential, but have the same eigenvalues as the original valence state Ψ^v and are called pseudo-wavefunctions. These new valence states project out of the valence wave-functions any overlap they have with the core wavefunctions, thereby having zero overlap with the core states. In other words, through the pseudopotential formulation, we have created a new set of valence states, which experience a weaker potential near the atomic nucleus, but the proper ionic potential away from the core region, beyond a certain cut-off radius r_c . Since it is this region in which the va-

lence electrons interact to form bonds that hold the solid together, the pseudo-wavefunctions preserve all the important physics relevant to the behaviour of the solid. Since then several methods have been used to generate more accurate as well as more efficient pseudo-potentials, keeping the basic principles same. In norm-conserving pseudopotential [24], the all electron (AE) wave function is replaced by a soft nodeless pseudo (PS) wave function, with the restriction to the PS wave function that within the chosen core radius the norm of the PS wave function has to be the same with the AE wave function and outside the core radius both the wave functions are just identical. Good transferability of constructed pseudopotential requires a core radius around the outermost maximum of the AE wavefunction, because only then the charge distribution and moments of the AE wavefunctions are well produced by the PS wavefunctions. Therefore, for elements with strongly localized orbitals like first-row, 3d and rare-earth elements, the resulting pseudopotentials require a large plane-wave basis set. To work around this, compromises are often made by increasing the core radius significantly beyond the outermost maximum in the AE wave-function. But this is usually not a satisfactory solution because the transferability is always adversely affected when the core radius is increased, and for any new chemical environment, additional tests are required to establish the reliability of such soft PS potentials. This was improved by Vanderbilt [25], where the norm-conservation constraint was relaxed and localized atom centered augmentation charges were introduced to make up the charge deficit. These augmentation charges are defined as the charge density difference between the AE and the PS wavefunction, but for convenience, they are pseudized to allow an efficient treatment of the augmentation charges on a regular grid. Only for the augmentation charges, a small cutoff radius must be used to restore the moments and the charge distribution of the AE wavefunction accurately. The success of this approach is partly hampered by rather difficult construction of the pseudopotential. Later Blöchl [22] developed the projector-augmented- wave (PAW) method, which combines idea from the LAPW method with the plane wave pseudopotential approach, which turns out to be computationally elegant, transferable and accurate method for electronic structure calculation of transition metals and oxides. This approach retains the all-electron character, but it uses a decomposition of the all-electron wavefunction in terms smooth pseudo-wave function and a rapidly varying contribution localized within the core region.

$$|\Psi_{AE}^n\rangle = |\Psi_{PS}^n\rangle + \sum_{I=1}^P \sum_{l,m} \sum_i (|\Phi_{AE}^{ilm}\rangle - |\Phi_{PS}^{ilm}\rangle) \langle \tilde{p}_i^{ilm} | \Psi_{PS}^n \rangle \quad (2.76)$$

where, $\Phi_{AE}^{ilm}(r)$ are the all-electron partial waves centered at atom I obtained for a reference atom, and $\Phi_{PS}^{ilm}(r)$ are the pseudo-atomic partial waves that coincide with the all-electron one outside a cut-off radius and match continuously inside. The projector functions verify the relation $\langle \tilde{p}_i^{ilm} | \Phi_{PS}^{ilm} \rangle = \delta_{ij}$. The sums run over all the atomic sites I, angular momentum(l,m) and projector functions i. For a single projector this is basically a OPW method. Using the above expression for the wave function, the orthogonality relation of the projectors and pseudoatomic partial waves, splits the electronic density naturally into three disjoint contributions : a soft pseudo-charge density arising from $\Psi_{PS}^n(r)$, and two localized charge densities involving $\Phi_{AE}^{ilm}(r)$ and $\Phi_{PS}^{ilm}(r)$ respectively. Similar partitions can be obtained for potential and energy[23] . All the expressions involving the pseudized quantities are evaluated on a Cartesian grid using plane waves, while the expressions involving localized quantities are evaluated using radial grids. No cross terms appear which might require both the grids. Furthermore, although it is strictly not necessary, the PAW method freezes the core orbitals to those of a reference configuration and works only with valence wave functions, exactly as the pseudized method. Therefore, all the pseudopotential machinery is available for the PAW method, which just has to be supplemented with contributions from spherical regions.

2.1.5.2 Linear Muffin-Tin Orbital (LMTO) method

The LMTO method is based on the muffin-tin approximation. Here the potential is assumed to be spherically symmetric (close to the ion core), within a sphere of a certain radius S_R , centered around the ion cores, called the muffin-tin sphere. In the interstitial regions, i.e, in the rest of the space, the potential varies very slowly and hence is replaced by a constant average potential(Fig. 2.4). Mathematically, this MT potential can be represented as :

$$v(r-R) = \begin{cases} v(r_R) & \text{for } r_R \leq S_R; r_R = |r-R| \\ -v_0 & \text{for } r_R > S_R \end{cases} \quad (2.77)$$

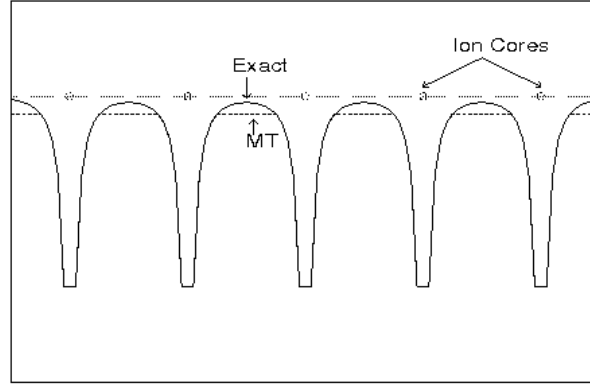


Figure 2.4 Construction of Muffin Tin(MT) potential. Exact implies the actual potential as it occurs close to the ion cores (marked in the figure). The MT potential, which arises from the muffin-tin approximation, has also been marked in the figure.

Within the MT sphere, the potential is spherically symmetric, hence they are solutions of the radial equation:

$$\left[\frac{d^2}{dr_R^2} - v(r) + \frac{l(l+1)}{r_R^2} - \varepsilon \right] r_R \phi_{RL}(r_R, \varepsilon) = 0 \quad (2.78)$$

Outside the MT sphere, since the potential is constant, $v(r_R) = -v_0$, the wave-function is a solution of the following Schrodinger equation:

$$\left[\frac{d^2}{dr_R^2} + \frac{l(l+1)}{r_R^2} - \kappa^2 \right] r_R \phi_{RL}(r_R, \varepsilon) = 0 \quad (2.79)$$

where $\kappa^2 = \varepsilon - v_0$

The wave-functions in the interstitial region, where the potential is constant, are plane waves, which can be expanded in spherical Bessel and Neumann functions.

$$A_{Rl}(\varepsilon, \kappa) j_l(\kappa r_R) + B_{Rl}(\varepsilon, \kappa) \eta_l(\kappa r_R) \quad (2.80)$$

The partial wave solution in all space is given by:

$$\phi_{RL}(R_r, \varepsilon) = \begin{cases} N_{RL}^0(\varepsilon, \kappa) \phi_{RL}(r_R, \varepsilon) & \text{if } r_R \leq S_R \\ \eta_l(\kappa r_R) + P_{RL}^0(\varepsilon, \kappa) j_l(\kappa r_R) & \text{if } r_R > S_R \end{cases} \quad (2.81)$$

But, we would like the basis to be such that its head contains all information about the potential, while its tail contains information only about the constant potential outside the MT sphere. In addition the basis should be well behaved in all space. A way of doing this is the following:

$$\phi_{RL}(R_r, \varepsilon) = \begin{cases} N_{RL}^0(\varepsilon, \kappa) \phi_{RL}(r_R, \varepsilon) + P_{RL}^0(\varepsilon, \kappa) j_l(\kappa r_R) & \text{if } r_R \leq S_R \\ \eta_l(\kappa r_R) & \text{if } r_R > S_R \end{cases} \quad (2.82)$$

They qualify as suitable basis for representation of the wave function in all space.

If we consider an array of ion-cores, with intervening interstitials, the wave-function for the system would simply be a linear combination of the MT orbitals associated with the individual MT potentials centered at different R.

$$\Psi(r, \varepsilon) = \sum_R \sum_L C_{RL}(\varepsilon) \chi_{RL}(r - R, \varepsilon) \quad (2.83)$$

The expression for the tails of the Neumann function $\eta_l(\kappa r_R)$ outside its personal sphere is taken to be as:

$$\eta_l(\kappa r_R) = -\sum_{L'} S_{RL, R'L'}^0(\kappa) j_{l'}(\kappa r'_R) \quad (2.84)$$

$S_{RL, R'L'}^0(k)$ are canonical structure constants depending on the relative position of R and R' and independent of ion-core potentials.

Referring to Fig.2.5, the wave function can be written as :

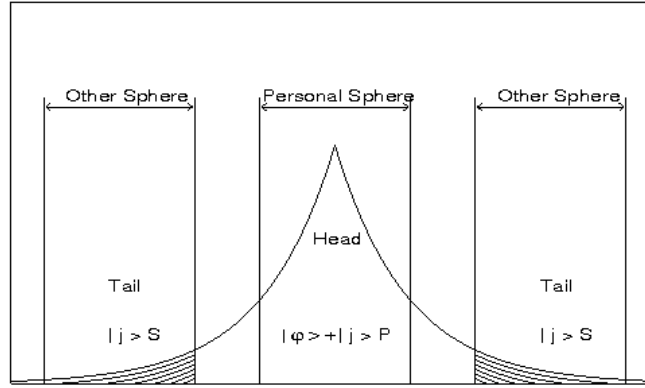


Figure 2.5 The envelope of a MTO centered at R with its head in its own sphere at the centre and tails in the neighbouring two sphere.

$$\chi_{RL}(r-R, \varepsilon) = \begin{cases} [N_{RL}^0(\varepsilon, \kappa)\phi_{RL}(r_R, \varepsilon) + P_{RL}^0(\varepsilon, \kappa)j_l(\kappa r_R)]Y_L(r_R) & \text{if } r_R \leq S_R \\ -\sum_{L'} j_{l'}(\kappa r_{R'})S_{R'L',RL}^0(\kappa)Y_L(r_R) & \text{if } r_{R'} \leq S_{R'} \\ -\sum_{L''} j_{l''}(\kappa r_{R''})S_{R''L',RL}^0(\kappa)Y_L(r_R) & \text{if } r_{R''} \leq S_{R''} \\ \dots\dots\dots & \\ \eta_l(\kappa r_R)Y_L(r_R) & \text{if } r_R \in \text{interstitial} \end{cases} \quad (2.85)$$

Considering,

$|\Psi_R\rangle$ to represent functions defined in all space,

$|\Psi_R\rangle$ to represent functions are all zero outside personal sphere, and

$\#\Psi_R\rangle$ to represent functions that are non-zero only in the interstitial space, one can write :

$$|\chi_R(\varepsilon)\rangle = N_R^0(\varepsilon)|\phi_R(\varepsilon)\rangle + P_R^0(\varepsilon, \kappa)|j_R(\kappa)\rangle - \sum_{R'} S_{RR'}^0(\kappa)|j_{R'}(\kappa)\rangle + \#\eta_R(\kappa)\rangle \quad (2.86)$$

This was for a single MT sphere, considering a linear combination of all MTs, the total wavefunction can be written as :

$$|\Psi(\varepsilon)\rangle = \sum_R C_R^+(\varepsilon)|\chi_R(\varepsilon)\rangle \quad (2.87)$$

Confining ourselves to a single MT sphere centered at R_0 , the potential seen by an electron in the solid is identical to that in the single MT potential at R_0 . Hence, the solution to the Schrodinger equation of the electrons in solid within the MT sphere, i.e, $r_{R_0} < S_{R_0}$ is:

$$|\Psi(\epsilon)\rangle = C_{R_0}^+(\epsilon) N_{R_0}^0(\epsilon) |\phi_{R_0}(\epsilon)\rangle \quad (2.88)$$

Substituting Eqn 2.86 into Eqn 2.87 and doing some further simplification:

$$|\Psi(\epsilon)\rangle = \sum_R C_R^+(\epsilon) [N_{R_0R}^0(\epsilon) |\phi_R(\epsilon)\rangle + \{P_{R_0R}^0(\epsilon, \kappa) - S_{R_0R}^0(\kappa)\} |j_R(\kappa)\rangle] \quad (2.89)$$

Comparing equations 2.87 and 2.89, we see that the extra term $P_{R_0}^0(\epsilon) |j_{R_0}(\kappa)\rangle$ which was added to the partial wave corresponding to the head is exactly cancelled by the contributions of the tail $S_{R_0R}^0(\kappa) |j_R(\kappa)\rangle$ coming from all the other MT spheres. Hence,

$$C^+ N^0(\epsilon)^{-1} [P^0(\epsilon, \kappa) - S^0(\kappa)] = 0 \quad (2.90)$$

where, $N^0(\epsilon) = N_{R_0R}^0(\epsilon)$, $P^0(\epsilon, \kappa) = P_{R_0R}^0(\epsilon, \kappa)$ and $S_{R_0R}^0(\kappa) = S^0(\kappa)$. The above equation forms a set of linear equations in unknowns $C_{R_L}(\epsilon)$.

This leads to the set of KKR equations :

$$\det ||P^0(\epsilon, \kappa) - S^0(\kappa)|| = 0 \quad (2.91)$$

Using which one can determine the eigenvalues ϵ .

It was desirable that one bypasses this energy dependence of the KKR equation. Hence, Andersen [25] devised a way for linearizing these equations. The energy dependent solution of the Schrodinger equation inside a MT sphere can be expanded as a Taylor series about some energy $\epsilon_{R_L}^V$ in our range of interest.

$$|\phi_{RL}(\epsilon)\rangle = |\phi_{RL}(\epsilon^V)\rangle + (\epsilon - \epsilon_{R_L}^V) |\dot{\phi}_{RL}(\epsilon_{R_L}^V)\rangle + O((\epsilon - \epsilon_{R_L}^V)^2) \quad (2.92)$$

We define two functions :

$$|\Phi(\varepsilon)\rangle = N^0(\varepsilon)(N^0)^{-1}|\phi(\varepsilon)\rangle \quad (2.93)$$

$$|\dot{\Phi}(\varepsilon)\rangle = N^0(\varepsilon)(N^0)^{-1}|\dot{\phi}(\varepsilon)\rangle + \dot{N}^0(\varepsilon)(N^0)^{-1}|\phi(\varepsilon)\rangle \quad (2.94)$$

Andersen's method was to build a linearized MT orbitals by taking Neumann function at a fixed value of κ and replacing the head by a linear combination of functions $|\phi_R\rangle$ and $\dot{\phi}_R$. In addition, the tails of the LMTO in the other spheres are replaced by $|\dot{\phi}_{R'}\rangle$ associated with these spheres centered at R.

Hence, the basis function can be written as :

$$||\chi_R\rangle = ||\eta_R\rangle + |\phi_R\rangle + \sum_{R'} h_{RR'} |\dot{\phi}_{R'}\rangle - |\eta_R\rangle \quad (2.95)$$

$$= |\phi_R\rangle + \sum_{R'} h_{RR'} |\dot{\phi}_{R'}\rangle + \# \eta_R \quad (2.96)$$

The notations $|\rangle$, $||\rangle$ and $\#\rangle$ have already been discussed before.

The secular equation follows directly from variational treatment of the Hamiltonian representation as in any fixed basis set method.

$$||\varepsilon I - H|| = 0 \quad (2.97)$$

Expanding the potential term about the reference energy :

$$P^0(\varepsilon) = P^0 + (\varepsilon I - \varepsilon^v) \dot{P}^0 \quad (2.98)$$

Since \dot{P} is totally diagonal, the matrix $(\dot{P}^0)^{1/2}$ is also totally diagonal. Substituting the expansion in Eqn. ,

$$\det[(P^0)^{1/2}] || P^0 (\dot{P}^0)^{-1} + \varepsilon I - \varepsilon^v - (\dot{P}^0)^{-1/2} S^0 (\dot{P}^0)^{-1/2} || \det[(P^0)^{1/2}] = 0 \quad (2.99)$$

if $\det[(P^0)^{1/2}] \neq 0$ then

$$\det\|P^0(\dot{P}^0)^{-1} + \epsilon I - \epsilon^v - (\dot{P}^0)^{1/2}S^0(\dot{P}^0)^{1/2}\| = 0 \quad (2.100)$$

Comparing Eqn. 2.100 and Eqn. 2.97 :

$$H = C + \Delta^{1/2}S\Delta^{1/2} \quad (2.101)$$

where $C = -P^0(\dot{P}^0)^{-1}$ and $\Delta = (\dot{P}^0)^{-1}$

This linearized method of the MTO is quite popular because it is fast.

2.1.6 LDA+U method, missing correlation effect

Electron-electron correlation effects have been treated in an average way in the local-spin density approximation (LSDA)[4, 5] of the one-electron band theory. Although this assumption works well for most of the materials, it fails in case of materials that contain narrow bands. Hence, in spite of its many successes, LSDA has been unable to correctly deal with strongly correlated materials. According to band theory, a system containing an odd number of electrons will give rise to a partially filled band at the Fermi-level and hence should be classified as a metal. Accordingly, band theory classifies materials like CoO and FeO which are otherwise known to be hard-core insulators as metals because of odd number of electron in these systems. For such materials, a more accurate treatment of the strong correlation effect is required. In other words, one needs to repair LSDA.

As summarized by Anisimov *et al* in their 1997 review [24], there have been several attempts improve LDA, in order to account for strong electron-electron correlations. One of the most popular methods in the self-interaction correction(SIC) [25]. It reproduces quite well the localized nature of the d (or f) transition(or rare earth) electrons. But SIC one-electron energies are in strong disagreement with spectroscopic data.

The other method is the Hartree-Fock(HF) method [26], which contains a term that explicitly cancels self-interaction. However, a serious problem with HF method is that here the Coulomb interaction considered is not screened.

A much more successful method in describing highly correlated system is the Hubbard LSDA+U method [27, 28, 29]. Here, the electrons are divided into two sub-systems, localized d(or f) electrons, for which coulomb d-d interaction should be taken into account by a term:

$$\frac{1}{2}U\sum_{i\neq j}n_in_j \quad (2.102)$$

where n_i are the d-orbital occupancy, and the delocalized s or p electrons which are well described by the orbital independent one-electron potential as given by LDA.

Let us consider a system with fluctuating number of d-electrons. The total number of d-electrons in the system is given by :

$$N = \sum_i n_i \quad (2.103)$$

Then, the Coulomb interaction energy between the d-electrons in given by:

$$E = \frac{UN(N-1)}{2} \quad (2.104)$$

This should be subtracted from the LDA total energy and a Hubbard-like term should instead be added:

$$E = E_{LDA} - \frac{UN(N-1)}{2} + \frac{1}{2}U\sum_{i\neq j}n_in_j \quad (2.105)$$

Then the orbital energies are given by:

$$\epsilon_i = \frac{\partial E}{\partial n_i} = \epsilon_{LDA} + U\left(\frac{1}{2} - n_i\right) \quad (2.106)$$

This formula shifts the LDA orbital energy by $(-U/2)$ for occupied orbital for which $n_i = 1$ and by $(+U/2)$ for unoccupied orbital with $n_i = 0$ (Refer to Fig. 2.6).

The LDA+U orbital dependent potential gives upper and lower Hubbard bands with the energy separation between them equal to the Coulomb parameter U. Hence this methods helps qualitatively

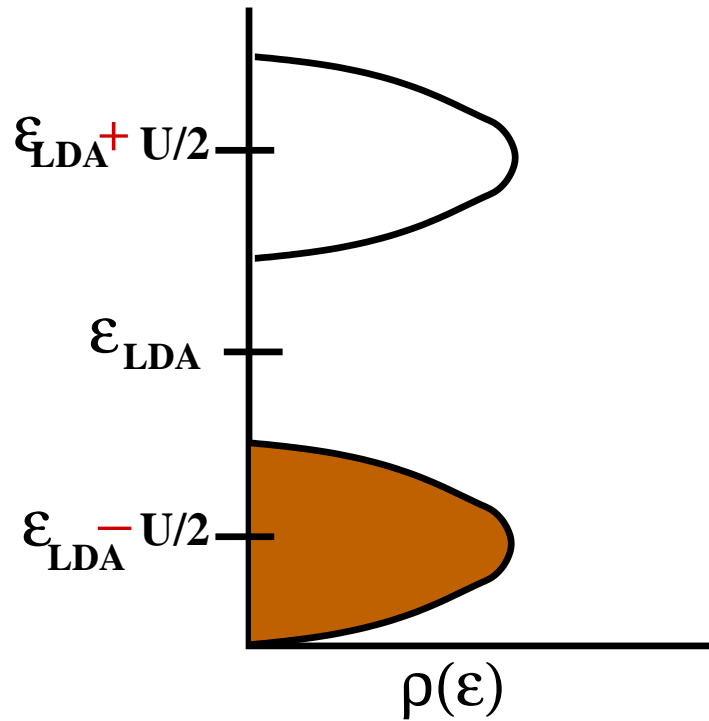


Figure 2.6 The shifting of the occupied and unoccupied LDA orbitals with respect to each other due to presence of the U parameter.

reproduce the correct physics and hence the insulating nature of systems with transition metal and even number of electrons. Such systems are popularly known as Mott-Hubbard insulators.

We have used rotationally invariant multi-band Hubbard model in our calculations. There are two popular approaches in this regard. They are :

(i) The Lichtenstein method

This method was proposed by Lichtenstein *et al* in their 1995 paper [29]. It basically requires identification of regions in space where the atomic characteristics of the electronic states are largely satisfied. Within the atomic spheres one can expand wave-functions in a localized orthonormal basis $|inlm\sigma\rangle$, where i denotes the site, n denotes the principal quantum number, l the orbital quantum number, m the magnetic number and σ the spin index. Let us assume that a particular shell is partly filled. A density matrix for correlated electrons in this shell is defined as follows :

$$n_{mm'}^\sigma = -\frac{1}{\pi} \int I_m G_{ilm,ilm'}^\sigma(E) dE \quad (2.107)$$

where : $G_{ilm}^{ilm'}(E) = \langle ilm\sigma | (E - H')^{-1} |ilm'\sigma \rangle$ are the elements of the Green's function matrix in this localized representation and H is the effective single electron Hamiltonian. The integration is carried over from 0 to E_F , the Fermi energy. In terms of the elements of the density matrix $\{n\}$, we define the generalized LDA+U functional as follows :

$$E^{LDA+U}[\rho^\sigma(r), n^\sigma] = E^{LSDA}[\rho^\sigma(r)] + E^U[\{n^\sigma\}] - E_{dc}[\{n^\sigma\}] \quad (2.108)$$

where $\rho^\sigma(r)$ is the charge density for spin- σ electrons and $E^{LSDA}[\rho^\sigma(r)]$ is the standard LSDA functional. Eqn. 2.108 asserts that LSDA suffices in the absence of orbital polarizations, while the later are described by the mean-field (Hartree-Fock) type of theory:

$$\begin{aligned} E^U[\{n\}] &= \frac{1}{2} \sum_{\{m\}, \sigma} \{ \langle m, m'' | V_{ee} | m', m''' \rangle n_{mm'}^\sigma, n_{m''m'''}^{-\sigma} \\ &+ (\langle m, m'' | V_{ee} | m', m''' \rangle - \langle m, m'' | V_{ee} | m''', m' \rangle) n_{mm'}^\sigma, n_{m''m'''}^\sigma \} \end{aligned} \quad (2.109)$$

where V_{ee} are the screened Coulomb interactions among the nl electrons. The last term in Eqn. 2.108 corrects for double counting and is given by:

$$E_{dc}[\{n_\sigma\}] = \frac{1}{2} U n(n-1) - \frac{1}{2} J [n_\uparrow(n_\uparrow - 1) + n_\downarrow(n_\downarrow - 1)] \quad (2.110)$$

where $n^\sigma = Tr(n_{mm'}^\sigma)$ and $n = n^\uparrow + n^\downarrow$. U and J are screened coulomb and exchange parameters.

The effective single-particle potential to be used in the effective single-particle Hamiltonian H ,

$$\begin{aligned} V_{mm'}^\sigma &= \sum_{m'', m'''} \{ \langle m, m'' | V_{ee} | m', m''' \rangle n_{m''m'''}^{-\sigma} + (\langle m, m'' | V_{ee} | m', m''' \rangle \\ &- \langle m, m'' | V_{ee} | m''', m' \rangle) n_{m''m'''}^\sigma \} - U(n - \frac{1}{2}) + J(n^\sigma - \frac{1}{2}) \end{aligned} \quad (2.111)$$

Here also, we claim that within the atomic spheres these interactions retain their atomic nature. The matrix elements can be expressed in terms of complex spherical harmonics and effective Slater integral [30].

(ii) The Dudarev method

The simplified (rotationally invariant) approach to LSDA+U as proposed by Dudarev *et al* [31] is as follows : Taking into account the orbital degeneracy of the 3d electrons, the model Hamiltonian is written by :

$$H = \frac{U}{2} \sum_{m,m',\sigma} n_{m,\sigma} n_{m',-\sigma} + \frac{U-J}{2} \sum_{m \neq m',\sigma} n_{m,\sigma} n_{m',\sigma} \quad (2.112)$$

where the summation is performed over projections of the orbital momentum ($m, m' = -2, -1 \dots 2$ in case of d electrons). U and J are the spherically averaged matrix elements of the screened Coulomb and Exchange interactions.

Here the parameters U and J do not enter separately, only the difference ($U - J$) is meaningful.

2.1.7 Calculation of properties using DFT

2.1.7.1 Density of states and band structure

Density of states (DOS) of a system describes the number of states per interval of energy level that are available to be occupied by electrons. Unlike isolated systems, like atoms or molecules in a gas phase, the density distribution is not discrete but continuous for bulk materials. A high DOS at a specific energy level means that there are many states available for occupation. A DOS of zero means that no states can be occupied at that energy level. Partial density of states (PDOS) on the other hand decomposes the total density of states into contributions due to different angular components (i.e, s-like and p-like) for different atoms in the system. We have extensively used the total DOS and the partial-DOS for analysis of our results.

The density of states $g(\varepsilon)d\varepsilon$ for energies in the range $[\varepsilon, \varepsilon + d\varepsilon]$ is given by a sum over all states

with energy in the range. In a crystal the expression for DOS is:

$$g(\varepsilon) = \frac{1}{\Omega} \sum_{n,k} 2\delta(\varepsilon - \varepsilon_k^{(n)}) \quad (2.113)$$

$$= \frac{2}{(2\pi)^2} \sum_n \int (\varepsilon - \varepsilon_k^{(n)}) dk \quad (2.114)$$

$$= \frac{1}{(2\pi)^3} \int_{\varepsilon_k^{(n)} = \varepsilon} \frac{1}{|\nabla_k \varepsilon_k^{(n)}|} dS_k \quad (2.115)$$

Band structure of a solid describes those ranges of energy, called energy bands, that an electron within the solid may have ("allowed bands") and ranges of energy called band gaps ("forbidden gaps") where the electrons are not allowed. The concept of band comes from the celebrated band theory for solids. A material's band structure may be used to explain many physical properties of solids. In addition, we have also plotted the 'fat bands' which show the percentage contribution from a certain orbital of a given atom to the different bands.

2.1.7.2 Total Energy

Very accurate total energies have been estimated using pseudopotential method and the plane wave basis sets. These total energies are basically Kohn-Sham ground state energies and have been used extensively in this thesis to determine lowest energy, most preferred stable configuration from a set of possible configurations.

In plane wave calculations under periodic boundary condition, the actual system is infinitely periodically repeated. The energy of such a system being infinite, the energy per cell is a quantity that is well-defined and can be calculated through Kohn-Sham expression:

$$E_{KS}[\rho] = \frac{1}{N_{cell}} (T_e[\rho] + E_H[\rho] + E_{PS}^{loc} + E_{ii} + E_{XC}[\rho] + E_{PS}^{nl}) \quad (2.116)$$

Here $T_e[\rho]$ represents the kinetic energy component, $E_H[\rho]$ represents the Hartree energy, E_{ii} represents ion-ion interaction, $E_{PS}^{loc} + E_{PS}^{nl}$ represents electron-ion interaction, where the superscript *loc* and *nl* respectively refer to local and non-local parts of the pseudo-potential, $E_{XC}[\rho]$ represents the exchange-correlation energy.

Out of these, E_H , E_{PS}^{loc} and E_{ii} are the three local electrostatic energy terms, the sum of which is represented as E_{es} . Hence, E_{es} can be mathematically expressed as follows:

$$\begin{aligned}
E_H[\rho] + E_{PS}^{loc}[\rho] + E_{ii} &= \frac{1}{2} \int \int \frac{\rho(r)\rho(r')}{|r-r'|} drdr' & (2.117) \\
&+ \sum_{S=1}^{N_S} \sum_{I=1}^{P_S} \int \rho(r) v_{PS}^{loc,S}(|r-R_I|) dr \\
&+ \frac{1}{2} \sum_{I=1}^P \sum_{J=1, J \neq I}^P \frac{Z_I Z_J}{|R_I - R_J|}
\end{aligned}$$

where, $\rho(r)$ is the electrostatic charge distribution, S labels different atomic species, N_S number of atoms with atomic species ' S ', $v_{PS}^{loc,S}(r)$ represents the local component of the pseudopotential corresponding to that species, while long-distance behaviour is purely coulombic, Z_I represents the valence charge on ion core ' I ' and R_I gives its location.

All three terms in Eqn. 2.117 diverge for an infinite system. However, since the total charge distribution of valence electrons plus ionic cores is neutral, the electrostatic energy of a single cell should be finite. In order to sort this problem, we consider a neutralizing, continuous auxiliary charge distribution $\rho_i(r)$ associated with the nuclear subsystem (and thus negative), and add and subtract the electrostatic self-interaction energy (as given below) of the system:

$$\frac{1}{2} \int \int \frac{\rho_i(r)\rho_i(r')}{|r-r'|} drdr' \quad (2.118)$$

After performing some algebra the electrostatic energy can be written as :

$$\begin{aligned}
E_{es}[\rho] &= \frac{1}{2} \int \int \frac{\rho_T(r)}{\rho_T(r')} drdr' + \rho(r) (\sum_{I=1}^{P_S} v_{PS}^{loc,S}(|r-R_I|) - \int \frac{\rho_i(r')}{|r-r'|} dr') & (2.119) \\
&+ \frac{1}{2} (\sum_{I=1}^P \sum_{J=1, J \neq I}^P \frac{Z_I Z_J}{|R_I - R_J|} - \int \int \frac{\rho_i(r)\rho_i(r')}{|r-r'|} drdr')
\end{aligned}$$

where, $\rho_T(r) = \rho(r) + \rho_i(r)$ is a neutral charge distribution. With this rearrangement, all the terms give an energy contribution that is finite in the simulation cell.

The other terms of the total energy include :

Exchange-Correlation energy It can be mathematically represented as follows :

$$E_{XC}[\rho] = \int \rho(r) \varepsilon_{XC}[\rho] dr \quad (2.120)$$

which is calculated by integrating the *XC* energy density numerically in the real-space grid.

Kinetic Energy whose expression in real space is :

$$T_e[\rho(r)] = -\frac{\hbar^2}{2m} \sum_k w_k \sum_{i=1}^{N_k} f_i^{(k)} \int \phi_i^* \nabla^2 \phi_i dr \quad (2.121)$$

where $f_i^{(k)}$ is the occupation number of state "i" at wave vector "k", w_k is the weight of point "k" in the Brillouin Zone.

Non-local Pseudopotential This is the only contribution that is somewhat more complicated to compute. For a particular *l*-component, the matrix element for an atom "s" located at the origin are :

$$\nabla \tilde{V}_{k+G, k+G'}^{l,s} = \langle k+G | \nabla V_{PS}^{l,s} \hat{P}_l | k+G' \rangle \quad (2.122)$$

$$= \sum_{m=-l}^l \langle k+G | Y_{lm} \rangle \nabla V_{PS}^{l,s}(r) \langle Y_{lm} | k+G' \rangle \quad (2.123)$$

2.1.7.3 Vacancy Formation Energy

Let us consider a system (*AB*) [32]. Say, a vacancy is created in this system by the removal of a *B* atom. The vacancy formation energy ΔE_f can be defined in terms of the external chemical potentials of *A* and *B* and the Fermi energy (in case the defect is charged) as:

$$\Delta E_f = E(N_A, N_B) - N_A \mu_A - N_B \mu_B + q \varepsilon_f \quad (2.124)$$

where, $E(N_A, N_B)$ is the energy of the system containing N_A number for *A* atoms, N_B number of *B* atoms, μ_A and μ_B are the external chemical potentials and q is the charge of the defect including sign and ε_f is the Fermi energy. Now, the energy required to add one "A" and one "B" should be equal to the molar energy of one molecule of *AB*. Hence , we can re-write the formation energy as:

$$\Delta E_f = E(N_A N_B) - (N_A - N_B)\mu_A - N_B E_{AB} + q\varepsilon_f \quad (2.125)$$

where : $E(N_A N_B)$ is the energy of the defect system, the second term gives energy for adding the extra number of A atoms over and above the number of B atoms that remain in the system after the defect is created. The third terms gives the energy of the number of complete chemical formulae of the system that are there after the creation of the vacancy and the fourth term is due to any charge present.

In our case, since the structure and chemical composition of the minerals are very complicated, we have tried to work with a simpler method for calculation of the defect formation energy, by-passing the chemical potential concept. Here, we have considered the formation of the minerals in vacuum. Hence for us, the vacancy formation energy is obtained by subtracting the total energy of the vacancy-free structure from the sum of the energies of the vacancy bearing structure and the energy of the atom in isolation at which vacancy is created. This can be mathematically represented as follows:

$$\Delta E_f = E(A_m B_{m-1}) + E(B) - E(A_m B_m) \quad (2.126)$$

Due to the presence of defect charges(q) in certain cases, defect-defect correction of the form :

$$E(\text{correction}) = \alpha q^2 / \varepsilon L \quad (2.127)$$

is included, where α is the Madelung constant, L is the cell length, and ε is the dielectric constant[6]

2.1.7.4 Calculation of barrier height using NEB method

This method is used to determine minimum energy paths involved in a transition, wherein a group of atoms re-arrange themselves while going from one stable configuration to another. The potential energy maximum along this minimum energy path represents the barrier height that is encountered in such a process. Here, both the initial and final configurations for the transition are given. A chain of images (or replicas, or 'states') of the system is generated between the end point configurations and all the intermediate images are optimized simultaneously. In an elastic band method [34] several images

of the system are connected together to trace out a path. The images are connected using springs and the object function is defined as:

$$S^{PEB}(\bar{R}_1, \dots, \bar{R}_{P-1}) = \sum_{i=0}^P V(\bar{R}_i) + \sum_{i=1}^P \frac{PK}{2} (\bar{R}_i - \bar{R}_{i-1})^2 \quad (2.128)$$

Here $(P+1)$ represents the number of images, K is the spring constant and R_i represents the position of image i . $V(r_i)$ is the potential acting on the i th image. This object function S^{PEB} is then minimized with respect to intermediate images, while keeping the end point images, R_0 and R_P , fixed. This is referred to as plain elastic band method. But this method involves several disadvantages. In this method, the force acting on image i :

$$\bar{F}_i = -\bar{\nabla}V(\bar{R}_i) + \bar{F}_i^S \quad (2.129)$$

where : $\bar{F}_i^S = K_{i+1}(\bar{R}_{i+1} - \bar{R}_i) - k_i(\bar{R}_i - \bar{R}_{i-1})$

If the elastic band is too stiff, the path connecting the several images cuts the corner and therefore misses the saddle point region. But if a smaller spring constant is used, the elastic band or the path comes closer to the saddle point, but the images manage to slide down and avoid the barrier region, thus reducing the resolution of the path in the most critical region. This is shown in Fig. 2.7.

The cure is very simple. The problem with corner cutting actually results from the component of the spring force which is perpendicular to the path and tends to pull images off the Minimum Energy Path (MEP). The problem with sliding down results from the component of the true force $\bar{\nabla}V(R_i)$ in the direction of path. The distance between images becomes uneven so the net spring force can balance out the parallel component of the true force. This is what that is exactly followed in the nudged elastic band(NEB) method [7]. Here a minimization of an elastic band is carried out where the perpendicular component of the spring force and the parallel component of the true force are projected out. The force on the image i then becomes:

$$\bar{F}_i^0 = -\bar{\nabla}V(\bar{R}_i)_\perp + \bar{F}_i^S \cdot \hat{\tau}_\parallel \hat{\tau}_\parallel \quad (2.130)$$

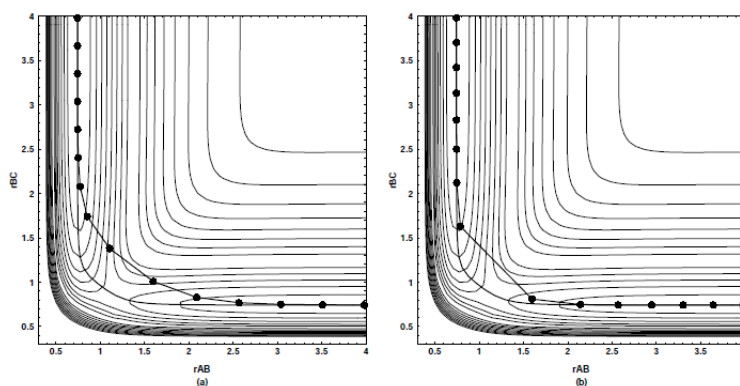


Figure 2.7 A contour plot of the potential energy surface for a simple test problem, where an atom, B, can form a chemical bond with either one of two movable atoms, A or C, as described by a LEPS(London-Eyring-Polanyi-Sato) [35] potential. The horizontal axis gives the A-B distance and the vertical axis the B-C distance. (a) A plain elastic band with spring constant $k = 1:0$ is shown with filled circles connected by a solid line. It cuts the corner and leads to an over estimate of the saddle point energy. The Minimum energy path (MEP) as obtained by the NEB method is shown with a solid line going through the saddle point. (b) Same as (a) but with a spring constant of $k = 0:1$. The corner cutting is diminished, but now the images slide down from the barrier region towards the minima at the endpoints thus reducing the resolution of the path in the region of greatest importance [36].

where $\hat{\tau}_{parallel}$ is the unit tangent to the path and $\bar{\nabla}V(\bar{R}_i)_\perp = \bar{\nabla}V(\bar{R}_i) \cdot \hat{\tau}_\parallel \cdot \hat{\tau}_\parallel$

We refer to this projection of perpendicular component of $\bar{\nabla}V$ and the parallel component of spring force as 'nudging'. These force projections decouple the dynamics of the path itself from the particular distribution of the images chosen in the discrete representation of the path. The spring force then does not interfere with the relaxation of the images perpendicular to the path and the relaxed configuration of the images satisfies $\bar{\nabla}V(\bar{R}_i)_\perp = 0$, i.e, they lie on the minimum energy path. Furthermore, since the spring force only affects the distribution of the images within the path, the choice of the spring constant is quite arbitrary. This decoupling of the relaxation of the path and the discrete representation of the path is essential to ensure convergence of the minimum energy path.

2.2 The Monte-Carlo simulation technique

Monte-Carlo methods are a class of computational algorithms that rely on repeated random sampling to compute results. This is a stochastic technique, and is based on the use of random numbers and probability statistics to investigate problems. This method hence is used in a wide variety of fields starting from economics to physics.

We have used the Monte-Carlo simulation technique in our physical system to determine equilibrium distribution properties as well as to investigate out-of-equilibrium situations.

When a system is in contact with its environment, the probability that the system is in a microstate 'S' with energy E_S is given by:

$$P_S = \frac{1}{Z} e^{-\beta E_S} \quad (2.131)$$

where $\beta = \frac{1}{kT}$ and Z is a normalization constant also known as the partition function of the system

$$Z = \sum_{S=1}^M e^{-\frac{E_S}{kT}} \quad (2.132)$$

This summation is over all microstates that are accessible to the system.

Using Eqn 2.131, one can calculate the ensemble average of the physical quantities of interest. For example, the mean energy is given by:

$$\langle E \rangle = \sum_{S=1}^M E_S P_S = \frac{1}{Z} \sum_{S=1}^M E_S e^{-\beta E_S} \quad (2.133)$$

Our aim is to simulate a system a system of N particles confined in a volume V at a fixed temperature T . Now, since we can generate only a finite number 'm' of the total number of M microstates, we might estimate the average value of a certain physical quantity 'A' as :

$$\langle A \rangle \approx A_m = \frac{\sum_{S=1}^m A_S e^{-\beta E_S}}{\sum_{S=1}^m e^{-\beta E_S}} \quad (2.134)$$

A_S is the value of A in the microstate 'S'

A very crude way would be to generate a microstate 'S' at random, calculate E_S , A_S and $e^{-\beta E_S}$, and evaluate the corresponding contribution of this microstate to B. However, if we follow this procedure, it is very much possible that we generate a microstate 'S', which is rather highly improbable, and hence would contribute very less to the sum B. So, instead of this, one uses methods where the more probable states are captured. One such method is the Metropolis algorithm. Here microstates are generated using a probability distribution function π_S defined as follows:

$$\pi_S = \frac{e^{-\beta E_S}}{\sum_{S=1}^m e^{-\beta E_S}} \quad (2.135)$$

i.e, we generate microsates with probability π_S

The following summarizes the Metropolis algorithm in context of the simulation of a system involving spins.

- (1)Start with an initial microstate having an energy E_{ini} .
- (2)Perform a random trial step, e.g, select a spin at random and invert it or say select a spin and randomly displace it. Call this step the trial step, the energy of which is designated by E_{trial}
- (3)Calculate $\Delta E = E_{trial} - E_{ini}$.
- (4)If ΔE is less than or equal to zero, accept the new microstate, goto step 8.
- (5)If ΔE is positive, compute the weight $w = e^{-\beta \Delta E}$.
- (6)Generate a random number 'r' in the interval [0,1]
- (7)If $r \leq w$, accept the new microstate, otherwise retain the initial state. This implies that if the temperature is high, we do not mind taking the 'not-so-probable' direction or step, but as the temperature is lowered, we are forced to settle into the most probable configuration that can be found in the neighborhood.
- (8)Determine the value of the desired physical quantity.
- (9)Repeat 2 to 8 to obtain sufficient number of microstates.
- (10)Compute averages over microsates.

Here, we basically compute the conditional probability that the system can be found in microstate 'S_j', given that it was in microstate 'S_i'. It is only necessary to evaluate the ratio $P_j/P_i = e^{-\beta \Delta E}$, and

hence it is not necessary to normalize the probability.

It is to be noted that for performing our Monte-Carlo simulation on mineral systems, we have developed a model Hamiltonian involving pseudo-spins (instead of real spins), where pseudospins are used to designate various chemical species, such as Fe, Mg. We will elaborate on this in great details in the following chapters.

Bibliography

- [1] M. Born and J. R. Oppenheimer, Ann. d. Physik **84**, 457 (1927).
- [2] E. Kaxiras, *Atomic and Electronic Structure of Solids*, Cambridge University Press (2003).
- [3] L. H. Thomas, *The calculation of atomic fields*, Proc. Cambridge Phil. Soc. **23**(5), 542 (1927).; Enrico Fermi, Rend. Accad. Naz. Lincei. **6**, 1049 (1927).
- [4] P. Hohenberg and W Kohn, Phys. Rev. **136**, B864 (1964).
- [5] W. Kohn and L. Sham, Phys Rev **14**, A1133 (1965).
- [6] M. Levy, Phys. Rev. A **26**, 1200-1208 (1982).
- [7] P. Hohenberg and W Kohn, Phys. Rev. **136**, B864 (1964), W. Kohn and L. Sham, Phys Rev **14**, A1133 (1965), P. A. M. Dirac *The Quantum Theory of the Electron*, Proceedings of the Royal Society A : Mathematical, Physical and Engineering Sciences **117**(778), 610(1928).
- [8] D. M. Ceperly, B. J. Alder, Phys. Rev. Lett. **45**, 566 (1980).
- [9] J. P. Perdew and Alex Zunger, Phys. Rev. B **23**, 5048 (1981).
- [10] J. P. Perdew, in *Electronic Structure of Solids '91* edited by P. Ziesche and H. Eschrig (Academie Verlag, Berlin, 1991).
- [11] J. P. Perdew, K. Burke and M. Ernzerhof, Phys. Rev. Lett. 3865 (1996).
- [12] J. C. Slater and G. F. Koster, Phys. Rev. **94**, 1498 (1954).

- [13] E. P. Wigner and F. Seitz, Phys. Rev. **46**, 509 (1934).
- [14] T. L. Loucks, *Augmented Plane wave Methods*, Benjamin, New York (1967).
- [15] J. Koring, Physica **13**, 392 (1947); J. Koringa, Phys. Rev. **238**, 341 (1994).
- [16] O. K. Andersen, Phys. Rev. **12**, 3060(1975).
- [17] G. Kresse and J. Hafner, Phys. Rev. B **47**, 558 (1993); G. Kresse and J. Furthmuller, Phys. Rev. B **54**, 11169(1996).
- [18] W. C. Herring, Phys. Rev. **57**, 1169 (1940); W. C. Herring and A. G. Hill, Phys. Rev. **58**, 132(1940).
- [19] D. R Hamman, M. Sluter and C. Chiang, Phys. Rev. Lett. **43**, 1494 (1979).
- [20] D. Vanderbilt, Phys. Rev. B **41**, 7892 (1985).
- [21] Alexander O. E. Animalu, *Intermediate Quantum Theory of Crystalline Solids*, Prentice-Hall of India Private Limited (1978).
- [22] P. E. Blöchl, Phys. Rev. B **50**, 17953 (1994).
- [23] P. E. Blöchl, Phys. Rev. B **50**, 17953 (1994); G Kresse and D Joubert, Phys. Ref. B **59**, 1758 (1999).
- [24] V. I. Anisimov, F. Aryasetiawan, A. I. Lichtenstein, J. Phys : Condens. Matter **9** 767 (1997).
- [25] A. Svane and O. Gunnarsson, Phys. Rev. Lett. **65** 1148 (1990).
- [26] S Massida, M. Posternak and A. Baldereschi, Phys. Rev. B **48**, 5058 (1993).
- [27] V. I. Anisimov, J. Zaanen and O. K. Andersen, Phys. Rev. B **44**, 943 (1991).
- [28] V. I. Anisimov *et. al.* Phys. Rev. B **48**, 16929 (1993).
- [29] A. I. Lichtenstein *et. al.*, Phys. Rev. B **52**, R5467 (1995).

- [30] B. R. Judd *Operator techniques in Atomic Spectroscopy* McGraw Hill, New York (1966).
- [31] S. L. Dudarev *et. al.*, Phys. Rev. B **57**, 1505 (1998).
- [32] A. F. Kohan, G. Ceder, D. Morgan, Chris G Van De Walle, Phys. Rev. B **61**, 15019 (2000).
- [33] J. Brodholt, Am. Miner. **82**, 1049 (1997).
- [34] A. Kuki and P. G. Wolynes, Science **236**, 1647 (1986); L. R. Pratt, J. Chem. Phys. **85**, 5045 (1986); R. Elber and M. Karplus, Chem. Phys. Lett. **139**, 375 (1987).
- [35] L. Martin-Gondre *et. al.* Chemical Physica Letters, Vol 471, Issue1-2 Pages 136-142 (2009).
- [36] H. Jönsson, G. Mills, K. W. Jacobsen, *Nudged elastic band method for finding minimum energy paths for transition.*
- [37] M. R. Sörensen *et. al.*, Surf. Sci. **72**, 1124(1994); G. Mills *et. al.* Phys. Rev. Lett. **72** 1124(1994); G. Mills *et. al.* Surf. Sci. **324**, 305 (1995); M. Villarba *et. al.*, Surf. Sci. **317**, 15 (1994).

Chapter 3

Site preference of Fe atoms in Olivine(FeMgSiO_4) and Pyroxene($\text{FeMg}(\text{SiO}_3)_2$) studied by density functional calculations

Olivine(FeMgSiO_4) and pyroxene($\text{FeMg}(\text{SiO}_3)_2$) are the two major minerals in the earth's upper mantle. In this chapter, we investigate the site preference of Fe in both these minerals. A combination of the state-of-the-art-techniques has been used for this purpose. The strong correlation effect at Fe site has been taken care of by means of local-density approximation+U calculations. Although the basic structural units that make up these two minerals are the same, namely, two kinds of metal-oxygen octahedron, M1 and M2 and Si-O tetrahedron, our $T = 0\text{K}$ study in the total energy minimized structures finds varied site preferences, indicating a strong preference for Fe to occupy M2 site in case of pyroxene and a preference for Fe to occupy M1 site in case of olivine [1]. We provide the microscopic understanding of our finding in terms of density of states and charge densities.

This chapter is based on *Phys. Rev. B* **79**, 115103 (2009)

3.1 Introduction

As introduced in the first chapter, olivine and pyroxene are the predominant mineral phases present in the Earth's upper mantle. They have recorded in them the physico-chemical environment prevailing at the interior of the Earth. Moreover, olivines are known to appear in extra-terrestrial bodies such as Mars, moon and meteorites. Hence, these mineral phases have drawn great attention of workers from different branches of science for over a long time. One of the main objective of these studies aims at developing thermodynamical models, and use them to understand the thermal evolution and the differentiation processes in the mantle.

The basic structural units in both olivines and pyroxenes are the same. They consist of Si-O tetrahedral unit and the Metal-O octahedral unit. These octahedral units are further of two types, namely, M1 and M2. The M1 octahedral geometry is comparatively more regular and smaller in size whereas the M2 octahedral unit is more distorted and larger.

A problem of great geological importance is the nature of the site preference of Fe-Mg in orthorhombic olivines and pyroxenes. At a given temperature, Fe and Mg cations are partitioned among the two in-equivalent octahedral sites M1 and M2 with varying proportions. It is an experimentally established fact that at room temperatures Fe strongly prefers M2 site in pyroxenes, resulting in Mg occupying M1 site[2, 3]. In contrary, there is a wide variation in the results reported on site preference in olivine. One of the earliest studies on the distribution of Fe-Mg over the two non-equivalent sites in olivines dates back to 60's[4]. Several investigations using X-ray diffraction[5], Mossbauer spectroscopy[6], crystal field spectra[7] yielded information about the crystal structure of olivine and suggested that the Fe^{2+} - Mg^{2+} distribution is either totally random or very weakly ordered, with Fe^{2+} preferring M2 site, which is in general true for Fe^{2+} in other silicate group of minerals. However, some experimental studies conducted on terrestrial and lunar samples of natural olivine revealed the tendency of Fe^{2+} to occupy M1 sites [8]. A distribution coefficient ' K_D ', described as follows, is popularly used to quantify partitioning of Fe into M1 and M2 site:

$$K_D = [(Fe)_{M1} \cdot (Mg)_{M2}] [(Fe)_{M2} \cdot (Mg)_{M1}] \quad (3.1)$$

where $Fe_{M1}(Mg_{M1})$ denotes the atomic fraction of Fe(Mg) at M1(M2) site. These groups reported increase of K_D values with increasing temperature indicating ordering of Fe^{2+} in the smaller and more regular M1 site. Since then a variety of experimental as well as theoretical studies[9] employing parameters like temperature[10], kinematics of Mg-Fe cation exchange between M1 and M2 sites[11], pressure[12], fugacity of oxygen[13], presence of elements other than Fe-Mg at octahedral sites[14] were carried out, but failed to reach a common conclusion. In-situ neutron diffraction studies conducted on olivine[15] reveals a switch over in the trend of K_D value with increasing temperature, suggesting a reversal of preference of Fe^{2+} from M1 to M2 at a critical temperature. But later studies challenged these findings, saying that Fe^{2+} orders into the smaller M1 site with rising temperature[16].

The study of intra-crystalline partitioning of Fe and Mg into the two octahedral sites can greatly help in the thermodynamic modeling of earth's mantle and also in understanding planetary processes. Before one attempts in understanding the complex temperature dependence and the thermodynamic evolution of the site-preference, it is worthwhile to consider the $T = 0K$ case and investigate the site preference issue from a quantum-mechanical point of view, which to the best of our knowledge has not been attempted before. Hence in this present work we have conducted extensive studies based on first principles electronic structure calculations to resolve the nature of Fe-Mg distribution in olivines. We have used pyroxene as a benchmark to justify and establish our methodology, for which the site preference of Fe has been definitely established.

3.2 Crystal structure

Olivines have a general formula M_2SiO_4 . They crystallize in the orthorhombic space group $Pbnm$ (International Table no. 62). The unit cell contains four formula units, i.e, 28 atoms out of which 8 may be either Fe or Mg, 4 Si and 16 O. The corresponding Wyckoff positions are given in Table I. Orthopyroxenes also crystallize in the orthorhombic symmetry but with a different space group, $Pbca$

(International Table no. 61). The unit cell contains 8 formula units, i.e. 80 atoms with 16 being Fe or Mg, 16 Si and 48 O, with all species occupying Wyckoff position 8c.

In order to understand the complex crystal structure of these silicate minerals we have broken up the complete lattice structure into three sub-lattices: (i) Si-O tetrahedral unit (ii) M1-O octahedral unit (iii) M2-O octahedral unit and compare them for olivine and pyroxene (Fig. 3.1).

The individual structural units of olivines and pyroxenes are described and compared in great details in the following:

Si-O tetrahedral unit- Olivine and pyroxene being silicate minerals are essentially built out of $(\text{SiO}_4)^{4-}$ tetrahedral units [see left panels in Fig. 3.1]. In any $(\text{SiO}_4)^{4-}$ unit there are three distinct oxygen positions corresponding to three distinct Si-O bonds. Out of the four oxygens two oxygen ions which are equidistant from Si are labeled as O3. The oxygen farthest from Si^{4+} , which also forms the apical oxygen is named as O1. The one situated nearest to Si^{4+} is O2. In the case of olivines, the tetrahedral units are completely isolated from each other and are called neso-silicates (as already introduced in the first Chapter). Viewed on the bc plane [top left panel in Fig. 3.1], the tetrahedral units form rows parallel to c -axis with alternately pointing up and down along the b axis in any particular row. On the other hand in case of orthopyroxenes, the SiO_4 tetrahedral units share corners forming chains [bottom left panel in Fig. 3.1]. The $(\text{SiO}_4)^{4-}$ units share their two O3 oxygen atoms with their neighbors forming the chained structure along c -axis. These chains are not straight as seen from the view along c [bottom left panel in Fig. 3.1] but form layer of tetrahedral units parallel to bc plane. These alternate planes can be further distinguished as T1 and T2 layer. The three distinct oxygen belonging to T1 are regarded as O1A O2A O3A and those belonging to T2 are designated as O1B O2B O3B.

M1-O octahedral unit- The M1 octahedral units in both olivines and pyroxenes are connected to each other forming chains. In olivine, two O1, two O2 and two O3 oxygen atoms participate in forming the M1O_6 octahedral unit along with centrally placed M1 cation. The neighboring M1O_6 octahedral units share edges (O1-O2) to form chains parallel to c -axis [top middle panel in Fig. 3.1]. Whereas, in pyroxene, two O1A, two O1B, one O2A and one O2B make up the M1 octahedra. It is to be noted that O3A and O3B are not connected to M1 in pyroxenes. The M1O_6 octahedra share (O1A-O2B) edges

Table 3.1 The Wykoff positions for each species in case of olivine.

atom	class	coordinates
M1	4a	(0,0,0), (1/2,1/2,0), (0,0,1/2), (1/2,1/2,1/2)
M2, Si, O1, O2	4c	(x,y,1/4), (x+1/2,-y+1/2,3/4), (-x,-y,3/4), (-x+1/2,y+1/2,1/4)
O3	8d	(x,y,z), (x+1/2,-y+1/2,-z), (-x,-y,z+1/2),(-x+1/2,y+1/2,-z+1/2), (-x,-y,-z), (-x+1/2,y+1/2,z), (x,y,-z+1/2), (x+1/2,-y+1/2,z+1/2)

with adjacent M1 octahedral units to form zig-zag chain like structures running almost parallel to *c* axis.

M2-O octahedral unit- The M2-octahedra in olivines is made out of one O1, one O2 and four O3 oxygen atoms. Each $M2O_6$ octahedral unit shares corners(O3 atom) with four other M2 octahedra to form a somewhat corrugated plane parallel to *ac* face of the unit cell. In case of pyroxene, all six inequivalent oxygen atoms participate in forming the $M2O_6$ octahedral unit. Unlike that of the olivine, in case of pyroxene the M2 octahedral units are not connected to each other and hence remain completely isolated.

On superimposing the three sub-lattices, one obtains the full structure of olivines and pyroxenes as shown in Fig. 3.2.

3.3 Results

3.3.1 Structural Optimization

The experimentally determined olivine and pyroxene crystal structures have been optimized using our theoretical tools. This is done in order to obtain the most stable configuration, as crystal structure data

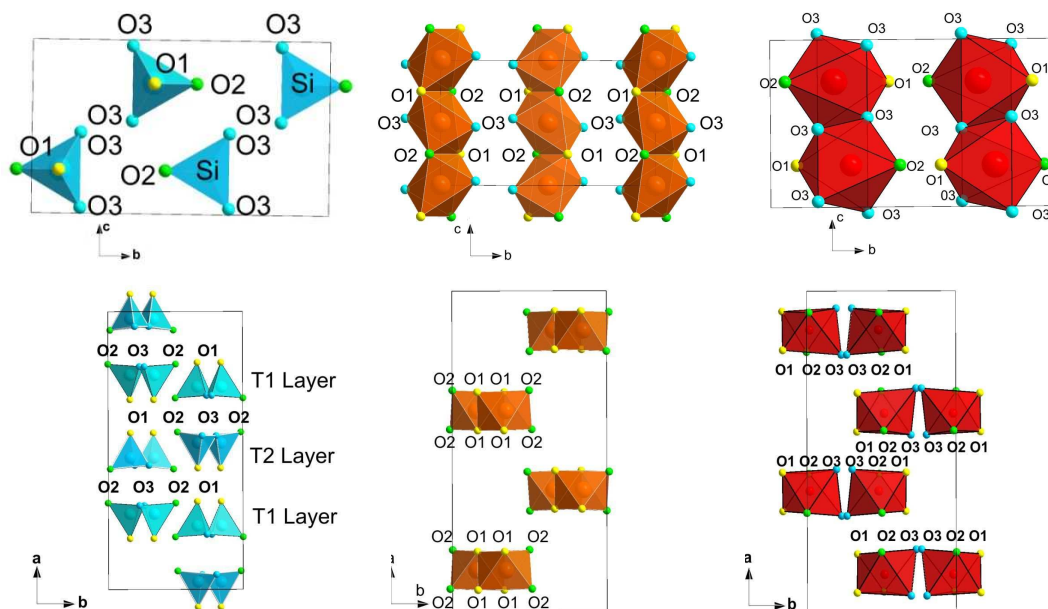


Figure 3.1 Building units of olivine projected on to *bc* plane (top panel) and pyroxene-projected onto *ab* plane (bottom panel). (a) SiO_4 tetrahedral unit. (b) M1-O octahedral unit. (c) M2-O octahedral unit.

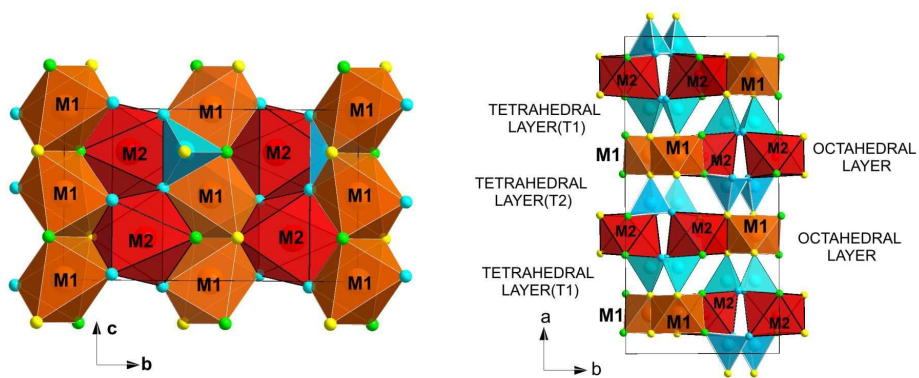


Figure 3.2 Complete lattice structure of olivine (left panel) and pyroxene (right panel)

used in our calculation are determined from actual minerals, which might have been formed under various diverse conditions, and hence might not be the equilibrium structure. Moreover oxygen being a light element, its positions co-ordinates can not be estimated very accurately using X-ray diffraction. Hence a structural optimization was done by employing the plane-wave pseudo-potential method as employed in VASP [20]. The atomic positions have been optimized keeping the lattice constants fixed at the experimentally estimates values.

The structural parameters, as obtained in our calculations are summarized in Table II. Although, the experimental measurements do not report separate data for Fe occupying M1 and M2 sites, the energy optimized data would very naturally depend on whether Fe occupies M1 or M2 site. We have therefore carried out structural relaxations for the two individual cases, Fe occupying M1 and M2 sites respectively. Table II shows the structural data for representative cases where all the M1(M2) sites are occupied by Fe(Mg) and vice-versa. The energetically optimized atomic positions show reasonable agreement with the experimental data listed in the first three columns. While the position of Fe/Mg cations and Si atom are found to remain more or less unchanged, the O atomic positions are found to differ at most by 5% for olivine and 10% for pyroxene. In the following, we have considered for our calculations the energetically optimized structure in each case.

3.3.2 Basic Electronic Structure

Our non-spin-polarized DFT-LDA calculation finds both Fe-containing olivine and pyroxene to be insulators. The insulating solution as obtained in non-spin-polarized LDA calculations, can be rationalized in the follow manner: the octahedral surrounding of Fe, which is created by the oxygen atoms splits the five degenerate Fe-d states into 3 t_{2g} and 2 e_g levels. The non-spin-polarized calculation forces $Fe^{2+}(3d^6)$ to go into low spin configuration, *i.e.*, the t_{2g} levels are completely filled whereas the e_g levels are completely empty. The energy gap between the t_{2g} - e_g levels appears as the gap at the Fermi level, thereby resulting in an insulator. The occupied energy levels for the Mg and Si atoms, which occur in their +2 and +4 oxidized states in olivines, lie deeper down, much below the Fermi level. However, once the spin degrees of freedom are relaxed through performance of spin-polarized calcu-

Table 3.2 Optimized structural parameters for olivine and pyroxene where all M1(M2) sites are occupied by Fe(Mg) and vice-versa in comparison to experimentally determined structure (data taken from ref 21 and 22). Lattice constants have been kept fixed at the experimental values.

OLIVINE

	experimental data			optimized data					
	[ref 21]			Fe at M1			Fe at M2		
atom	x	y	z	x	y	z	x	y	z
M1	0	0	0	0	0	0	0	0	0
M2	0.992	0.279	0.25	0.992	0.278	0.25	0.987	0.278	0.25
Si	0.425	0.098	0.25	0.428	0.096	0.25	0.429	0.094	0.25
O1	0.768	0.092	0.25	0.75	0.095	0.25	0.767	0.088	0.25
O2	0.217	0.451	0.25	0.208	0.448	0.25	0.226	0.451	0.25
O3	0.283	0.164	0.035	0.284	0.165	0.035	0.284	0.163	0.033

PYROXENE

	experimental data			optimized data					
	[ref 22]			Fe at M1			Fe at M2		
atom	x	y	z	x	y	z	x	y	z
M1	0.375	0.654	0.874	0.376	0.656	0.863	0.376	0.655	0.874
M2	0.378	0.483	0.367	0.376	0.492	0.358	0.378	0.487	0.366
Si1	0.474	0.337	0.796	0.473	0.336	0.708	0.473	0.336	0.796
Si2	0.272	0.341	0.052	0.274	0.341	0.049	0.272	0.341	0.058
O1	0.562	0.337	0.799	0.562	0.34	0.790	0.562	0.335	0.798
O2	0.312	0.501	0.053	0.314	0.5	0.041	0.313	0.501	0.056
O3	0.447	0.204	0.595	0.448	0.195	0.597	0.447	0.199	0.597
O4	0.184	0.338	0.041	0.185	0.344	0.027	0.183	0.337	0.046
O5	0.435	0.484	0.696	0.431	0.48	0.683	0.433	0.485	0.695
O6	0.303	0.231	0.824	0.304	0.21	0.832	0.303	0.228	0.833

lations, Fe appears in its high spin state, with a finite magnetic moment of about $3.7 \mu_B$ at the Fe site. The spin polarized calculation within the framework of LDA yields a metallic solution with fully filled Fe d states in the majority spin channel, and partially filled Fe t_{2g} states in the minority spin channel. It is therefore expected that the inclusion of missing correlation effect in LDA, within the partially filled Fe t_{2g} manifold would lead to opening up of a gap through formation of Mott-Hubbard insulator. The LDA+U calculations confirm this expectation. For all the LDA+U calculations, we have fixed the value of U at 4.5 eV while the Hund's exchange J is chosen to be 0.8 eV (introduced to consider the multi-orbital situation).

Fig. 3.3 presents the LDA+U density of state (DOS) for olivine (FeMgSiO_4) and pyroxene ($\text{FeMg}(\text{SiO}_3)_2$) projected on to Fe-d, O-p, Mg-sp and Si-sp states. Here, the zero of the energy is set at the top of the valence band. In these calculations, one of the octahedral sites out of 8 available have been assumed to be occupied by Fe and the rest by Mg. We show the density of states for the representative cases where the Fe(Mg) atoms have been put at M1(M2) sites, since the gross features of the density of states remain same in different site occupancies. We can see from the DOS plot that the Mg and Si states remain empty with negligible contribution in the occupied part of the DOS. The density of states close to Fermi energy is mostly dominated by O-p and Fe-d derived states, indicating a strong hybridization between Fe-d and O-p. The d-p hybridized bands extend from -9eV to 4eV in case of olivine and -11eV to 5eV in case of pyroxene. The split out states at the bottom of dp derived manifold in case of pyroxene in the energy range of about -11 eV to -9 eV arises out of O3A and O3B oxygens which are not connected to M1 site.

3.3.3 Total Energy Calculations - Site preference

The results of our total energy calculations within the framework of LDA+U, performed using our optimized geometries for olivine and pyroxene is shown in Table III. We find that in case of pyroxene when Fe is in the M2 site the total energy is much lower, compared to when it occupies the M1 site, the energy difference being 153.89 meV (1786.11 K) per Fe site[27]. Hence Fe occupying M2 site is the stable, preferred configuration in case of pyroxene. This result is in accordance with published

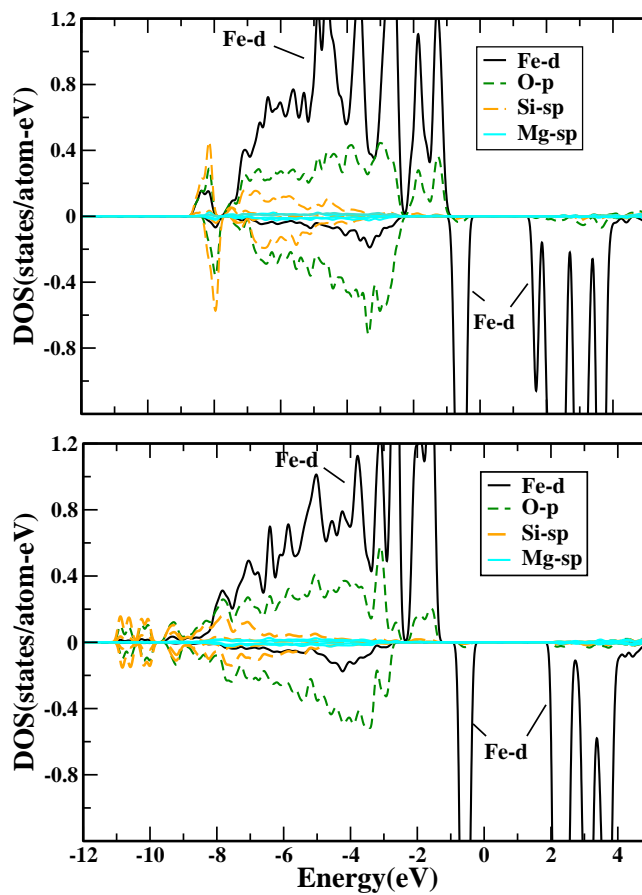


Figure 3.3 Partial DOS of olivine(top panel) and pyroxene(bottom panel) projected onto Fe-d, O-p, Si and Mg. Within each panel the upper(lower) sub-panel corresponds to majority(minority) spin. The negative of DOS has been plotted for the minority channel for clarity.

Table 3.3 LDA+U total energies for olivine and pyroxene with Fe atoms placed at the M1 sites and M2 sites respectively. Energy differences between the the two configurations are listed in the last row.

olivine		pyroxene	
site	Energy(eV)	site	Energy(eV)
Fe at M1	-218.04133	Fe at M1	-644.2392
Fe at M2	-217.89932	Fe at M2	-645.4710
Energy difference		Energy difference	
per Fe= 35.48 meV (411.83 K)		per Fe = 153.89 meV (1786.11 K)	

experimental results, where a strong preference of Fe for M2 site has been reported [3, 4]. Having succeeded in arriving at the correct description of site preference in case of pyroxene, we can conclude that our methodology successfully describes complicated mineral structure. Hence, we next extend it to the case of olivine, where the situation is rather unsettled. In case of olivine our total energy calculations show a preference for M1 site, the energy difference being 35.48 meV (411.83 K) per Fe site.

Total energy calculations performed at lower concentrations of Fe in olivine i.e, 25% (2 Fe atoms per unit cell) and 12.5%(1 Fe atom per unit cell) also show a preference of Fe for M1 site. For 25% concentration of Fe we obtain a energy difference of 43.97 meV (510.342 K) per Fe atom, whereas for 12.5% concentration, the energy difference is found to be 60.01 meV (696.522 K) per Fe atom. The quoted values are obtained by taking the average of energy differences where the two Fe sites are placed at six different configurations in case of 25% concentration and four different configurations in case of 12.5% concentration.

Further, attempts made to simulate the hydrostatic pressure by varying the experimentally measured lattice constant at ambient pressure, do not seem to alter the conclusion of Fe preferentially occupying M1 site. The energy difference were found to change by about 3% for a change of lattice parameters by 2%.

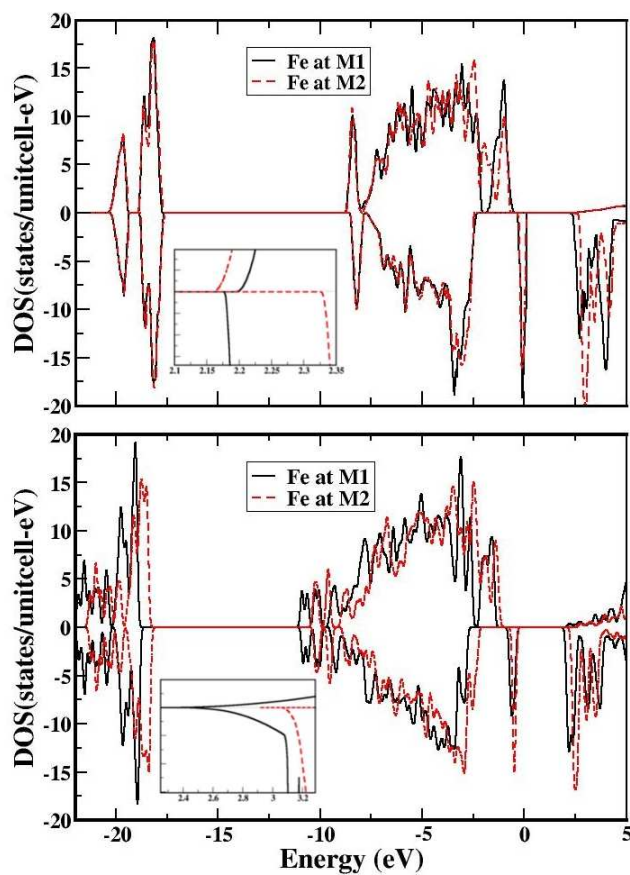


Figure 3.4 Comparison between total DOS for olivine and pyroxene with Fe at M1 and M2 sites in olivine (top panel) and pyroxene (bottom panel). The solid and the dashed lines correspond to DOS for Fe at M1 and M2 respectively. Inset shows an enlarged plot of DOS focused at the bottom of the conduction band.

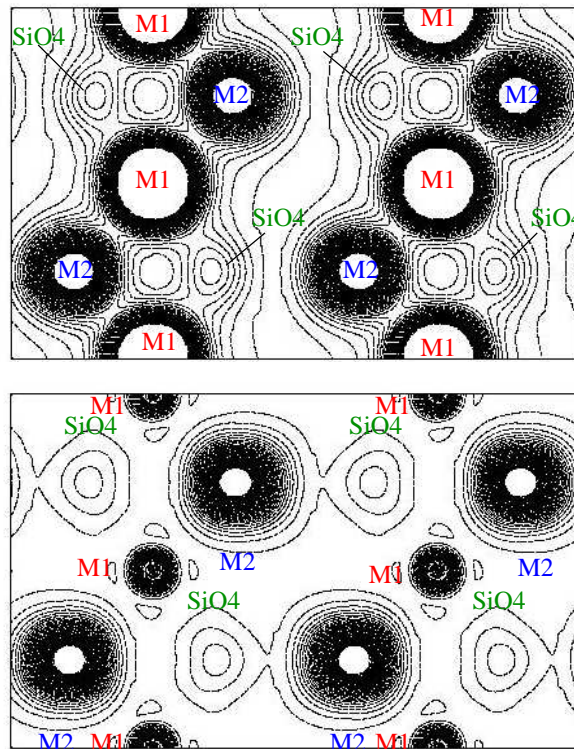


Figure 3.5 Charge density plot of olivine projected onto the *ac* plane. Top panel shows Fe at M1 site and Mg at M2 site. Bottom panel shows Fe at M2 site and Mg at M1. Contour values are $\rho_n = \delta \times n \times e^- / (\text{a.u.})^3$ where $\delta = 0.002$ and *n* labels the contours. Note enhanced covalency for Fe at M1 (top panel) compared to Fe at M2 (bottom panel).

3.3.4 Discussion

In order to explain our results, we perform a structural comparison and analysis of the olivine and pyroxene crystal structures. These are summarized in Table IV. We find that the distortion of M_2O_6 octahedral unit in case of olivine is about 2 times larger than that of M_1O_6 . Whereas, in the case of pyroxene, it is 3 times larger. The octahedral size analysis shows that the M_2O_6 octahedra is larger by 17% as compared to M_1O_6 in case of pyroxene while it is only 5% larger in case of olivine. The M_1O_6 and M_2O_6 structural difference is therefore much larger in case of pyroxene as compared to that of olivine. We know that the ionic radius of Fe^{2+} (0.76) is larger than that of Mg^{2+} (0.72) by 0.04. The mere size consideration would hence imply that Fe^{2+} should preferentially occupy the larger of the two octahedral units, M2 in both pyroxene and olivine. Although, our total energy calculations find such a preference in case pyroxene, it shows that Fe^{2+} prefers the smaller M1 site in case of olivine, which is against what is predicted using geometry. Hence, the simple size consideration works for pyroxene which has a large structural difference between M1 and M2 sites, but it fails in the case of olivine, where the structural difference between the M1 and M2 site is small. We note that the size argument is based on the concept of isolated M_1O_6 and M_2O_6 octahedra and does not take into account the connectivity of M1 and M2 sites to other sites which is different between olivine and pyroxene. The connectivity of these octahedral units to their respective crystal environment should also be an important parameter in the determination of site preference, which we will bring in next in our analysis.

In order to determine the microscopic origin of site preferences, we perform a comparison of the density of states(DOS) in two cases : (1) where the Fe atoms have been put into M1 and (2) where Fe atoms have been made to occupy M2 sites, the concentration of Fe-Mg being 50-50, for both olivine and pyroxene. While the gross features of the density of states are found to be similar between M2 occupied Fe^{2+} and M1 occupied Fe^{2+} situations, with occupied part of the spectrum being dominated by O-p and Fe-d, the two density of states differ in finer, minute details. The difference between DOS for Fe occupying M1 and M2 sites respectively, appears to be more pronounced in case of pyroxene than in case of olivine. This is but expected, because of the larger structural difference between M1 and M2 in case of pyroxene compared to olivine. The DOS shows a band gap of 2.18 eV for olivine

with Fe occupying M1 site as compared to a band gap of 2.16 eV with Fe occupying M2 site. In contrast, for pyroxene the band gap is found to be 3.06 eV for Fe in M2 site and 2.30 eV for Fe in M1 site. Larger band gap points towards greater stability in terms of lowering of band energy. Hence, the band-gaps computed also support the results obtained from total energy calculations. The lowering of energy levels can happen through increased co-valency effect between metal d and neighboring oxygen p states.. In case of pyroxene, the M1 site is connected to only four oxygen sites out of the six in-equivalent O sites, whereas M2 is connected to all the in-equivalent oxygens. Hence, because of this greater connectivity, there is an enhanced co-valency effect for Fe sitting at M2 site which works hand-in-hand with the larger volume effect at M2 site, resulting into a strong preference of Fe²⁺ for M2 site. In case of olivine, the M1 site forms chains by sharing the oxygen edges of neighboring octahedra while M2 sites form a network with corner shared oxygens from neighboring M2-octahedra resulting in reduced connectivity for Fe at M2 as compared to M1. This causes an enhanced covalency for Fe occupying M1 site, which is sufficient enough to overcome the larger size effect of M2 occupied situation. Fig. 3.5 shows the charge density plots in *ac* plane for olivine with M1 sites occupied by Fe(top panel) and M2 sites occupied by Fe(bottom panel). The Fe-O covalency is found to be much stronger for the M1 occupied case compared to M2 occupied case, placing further the arguments presented above on a strong footing.

3.4 Conclusion

In conclusion, we have carried out a thorough study of the site preference problem in case of silicate minerals like olivine and pyroxene using first-principles electronic structure calculations within the framework of density functional theory. While the experimental situation clearly indicates a preference for M2 site over M1 site for Fe in case of pyroxene, the situation in case of olivine was debatable. Our calculations at $T = 0K$ from a purely quantum chemical point of view found a strong preference towards M2 site for pyroxene in agreement with experimental finding, while at $T = 0K$ preference towards M1 site has been found for olivines. Our study finds the important role of covalency in deciding the site

Table 3.4 size and structural distortion of octahedral units

OLIVINE			
site	average M-O bond length	volume of MO_6 octahedron	RMS deviation of M-O bond length
M1	2.1287\AA	$12.8612 (\text{\AA})^3$	0.0407\AA
M2	2.1611\AA	$13.4575 (\text{\AA})^3$	0.078\AA
PYROXENE			
site	average M-O bond length	volume of MO_6 octahedron	RMS deviation of M-O bond length
M1	2.0917\AA	$12.2022 (\text{\AA})^3$	0.0592\AA
M2	2.2029\AA	$14.2536 (\text{\AA})^3$	0.1842\AA

preference in addition to size effect. Carrying over from this point, in the next chapter we present the effect of finite temperature on the site preference of Fe in olivine, which is a much debated topic in the geo-sciences community. Our zero temperature results and analysis, as presented in this Chapter, forms the basis of the finite temperature calculations that follow up in the next Chapter.

Bibliography

- [1] S. Chatterjee, S. Sengupta, T. Saha-Dasgupta, K. Chatterjee, N. Mandal, Phys. Rev. B **79** 115103 (2009).
- [2] J.A Sykes-Nord and G.M. Molin , Am. Mineral. **78**, 921 (1993).
- [3] G.M. Molin, S.K. Saxena, E. Brizi, Earth Planet. Sci. lett. **105**, 260 (1991).
- [4] S.Ghosh, Am. Mineral. **47**, 388 (1962).
- [5] J.D.Birle, G.V.Gibbs, P.B. Moore and J.V Smith, Amer. Mineral. **53**, 807 (1968).
- [6] W.R. Bush, S. S. Hafner, D. Virgo, Nature **227**, 1339 (1970).
- [7] R. G. Burns, Am. Mineral. **55**, 1609 (1970).
- [8] L.W.Finger, Carn. Inst. Year Book **69**, 302(1971); H.R. Wenk and K.N. Raymond, Z. Krist **137**, 86 (1973); J.R Smyth and R.M Hazen, Am. Mineral. **58**, 588(1973); S. Ghosh, C. Wan, I.S. McCallum, Indian J Earth Science **3**, 1 (1976).
- [9] H. Annersten, J.Adetunji, A.Filippidis, Am. Mineral. **69**, 1110 (1984); T. Akamatsu, M.Kumazawa, N.Aikawa, H.Takei, Phys. Chem. Minerals. **19**, 431 (1993).
- [10] F. Princivalle, Mineralogy and Petrology **43**, 121 (1990).
- [11] N. Aikawa, M Kumazawa, N Tokonami, Phys. Chem. Minerals **12**, 1 (1985).
- [12] R.M.Hazen, Am. Mineral **61** 1280 (1976), Am. Mineral. **62** 286 (1977).

- [13] G.Nover and G.Will, *Phys. Chem. Minerals*. **3** 95 (1978); *Phys. Chem. Minerals*. **4** 199 (1979); *Z. Krist* **155** 27 (1981); G. Ottonello, F.Princivalle, A. Della Giusta, *Phys. Chem. Minerals* **17**, 301 (1990).
- [14] V. Rajamani, G.E.Brown, C.T.Prewitt, *Am. Mineral.* **60**, 292 (1975); A.G.Nord, H.Annersten, A.Filippidis, *Am. Mineral.* **67**, 1206 (1982); H.R. Wenk and K.N. Raymond, *Z. Krist* **137**, 86 (1973).
- [15] G.Artioli, R.Rinaldi, C.C.Wilson, P.F.Zanazzi *Am. Mineral.* **80**, 197 (1995); C.M.B.Henderson, K.S.Knight, S.A.T. Redfern, B.J.Wood *Science* **271**,1713 (1996); Rinaldi et.all 2000; S.A.T.Redfern, G. Artioli, R.Rinaldi, C.M.B. Henderson, K.S.Knight, B.J.Wood, *Phys. Chem. Minerals* **27**, 630 (2000).
- [16] M.Morozov, C.Brinkmann, W.Lottermoser, W.Tippelt, G.Amthuer, H.Kroll, *Eur.J.Mineral* **17**, 495 (2005); M.N.Taran, M.Koch-MÃijller, *Phys. Chem. Mineral* **33**, 511 (2006).
- [17] P. Hohenberg and W. Kohn, *Phys. Rev.* **136**, B864 (1964); W. Kohn and L. J. Sham, *Phys. Rev.* **140**, A1133 (1965).
- [18] G.Kresse and J.Hafner, *Phys. Rev. B* **47**, 558 (1993); G.Kresse and D.Furthmüller, *Comput. Mater. Sci.* **6**, 15 (1996); *Phys. Rev. B* **54**, 11169 (1996).
- [19] O.K. Andersen and O. Jepsen, *Phys. Rev. Lett.* **53**, 2571 (1984).
- [20] P.E Blöchl, *Phys. Rev. B* **50**, 17953 (1994); G.Kresse and D.Joubert, *ibid*, **59**, 1758 (1999).
- [21] J.Hubbard, *Proc. R. Soc. London A* **276**, 238 (1963).
- [22] V.I. Anisimov *et al.* *Phys. Rev. B* **48**, 16929 (1993).
- [23] Leonardo Pisani and Roser Valenti', *Phys. Rev. B* **71**, 180409(R) (2005).

- [24] The obtained total energy differences, computed for the whole cell, has been divided by the number of Fe atoms present in the unit cell, so as to make the comparison between cases with different concentration of Fe atoms, easier.
- [25] S.A.T Redfern, G.Artioli, R.Rinaldi, C.M.B. Henderson, K.S.Knight, B.J.Wood, *Phys. Chem. Miner.* **27**, 630-637 (2000).
- [26] H. T. Jr. Evans, J. S. Huebner, J. A. Konnert, *Earth and Planetary Science Letters* **37**, 476-484 (1978).

Chapter 4

Crossover of cation partitioning in olivines : a combination of ab-initio and Monte carlo study

In this Chapter, we report our studies based on a combination of ab-initio electronic structure and Monte Carlo simulation technique on the problem of cation partitioning among in-equivalent octahedral sites, M1 and M2 in mixed olivines containing Mg^{2+} and Fe^{2+} ions, with increasing temperature. We find that there is no reversal of the preference of Fe for M1 over M2 as a function of temperature. Our findings do not agree with the experimental findings of Redfern *et al.* [1] but are supported by those of Heinemann *et al.* [2] and Morozov *et al.* [3].

4.1 Introduction

It has long been recognized that non-equilibrium cation ordering in minerals might provide a means to measure cooling rates of rocks. Such kind of studies have been reported on pyroxene [4], Al/Si ordering in alkali feldspar [5] and Mg/Fe ordering in amphiboles [6]. These minerals being comparatively

This chapter is based on *Phys. Rev. B* **81**, 155105 (2010)

complex, such kind of phenomena may easily get obscured by displacive phase transitions and exsolution phenomena. Hence, in this chapter, we deal with a structurally simpler mineral phase, olivine [7]. We have already shown in the previous chapter that due to difference in crystallographic environment of the two M-sites as well as in the chemical behaviour of Fe^{2+} and Mg^{2+} cations, Fe prefers to occupy a certain octahedral site at $T = 0K$. As an extension to this, here we study the temperature dependence of the site preference and hence the ordering/disordering of Fe in $Fe - Mg$ olivine ($FeMgSiO_4$). Such a study becomes important because it is directly related to the physical properties of the crystal and thermodynamic properties of the crystal assemblages. A knowledge of the effects of temperature (in addition to that of pressure and composition) on the non-convergent [27], inter-site ordering/disordering of the octahedral cations is essential for a thorough understanding of the thermodynamic, petrological and geophysical properties of the phase. Most importantly, the ability to determine the cooling rates of olivine from partitioning of the cations over the structurally distinct M1 and M2 octahedral sites would be invaluable in explaining a large number of issues. For example, ancient strombolian type eruptions could be distinguished from eruptions involving less rapid quenches on the basis of expected differences in M-site partitioning of olivines contained within them. Moreover, it could resolve the serious disagreement over whether alkali olivine basaltic sills cooled rapidly by processes involving convection [9] or more slowly, by method of conduction [10]. Determination of cooling rates, also known as "Geo-speedometry", from intra-crystalline cation partitioning demands precise and accurate knowledge of site occupancies over a large temperature range.[11]

In the case of the olivine structure, since the two inequivalent octahedral sites M1 and M2 have similar geometries as opposed to other structures such as pyroxenes or amphiboles, it makes the prediction of site preference of Fe in mixed Fe-Mg olivine difficult and hence the problem interesting and much debated. An enormous amount of contradictory reports have been published over a long time in this regard. We have theoretically addressed this site-preference problem in olivine at $T = 0K$ using a first principles study[12], which has been extensively discussed in the previous Chapter. For complete understanding of the site-preference problem, further knowledge of the effects of temperature on the ordering/disordering of the cations occupying the octahedral sites is essential. In the case of Fe-Mg

olivine the temperature variation of ordering/disordering is also highly disputed and has been debated for over a long time, the problem being still very much alive and burning till date.

As already introduced in the last Chapter, the site occupancy is quantitatively represented by a distribution coefficient K_D , for intra-crystalline partitioning of cations among the two inequivalent octahedral sites M1 and M2. Since, we have extensively used this parameter in this chapter, we feel it is worthwhile to describe it once again here. For mixed Fe-Mg olivine K_D is defined as follows :

$$K_D = \frac{[(Fe)_{M1} \cdot (Mg)_{M2}]}{[(Fe)_{M2} \cdot (Mg)_{M1}]} \quad (4.1)$$

where $Fe_{M1}(Mg_{M1})$ denotes the atomic fraction of Fe(Mg) at M1(M2) site. Hence when $K_D = 1$, it represents complete disorder. $K_D > 1(K_D < 1)$ indicates the preference of Fe to occupy M1(M2) site.

There have been a large number of experimental studies reported which deal with site preference of Fe with increasing temperature in Fe-Mg olivine. As early as in 1973, Smyth and Hazen[13] found using X-ray diffraction studies that Fe orders more and more into the smaller M1 site with increasing temperature. Later reports include those by Artioli *et al.*[14] and Rinaldi *et al.*[?, 15], who performed in-situ single crystal neutron diffraction studies on natural olivines (Fa10 and Fa12, where Fa stands for fayalite and the number following it represents the percentage of Fe in the octahedral sites, the rest being Mg) at temperatures upto 1300°C. They found Fe^{2+} to be initially enriched into M1 site. However beyond a certain critical temperature $\sim 900^\circ C$, the site preference was found to be reversed. Given the existing knowledge of other minerals, such reversal of site preference is an unexpected phenomena and therefore interesting. A similar behavior was found by Redfern *et al.*[1] for synthetic polycrystalline olivine (Fa50). In this study the state of complete disorder was reached at $\sim 600^\circ C$, beyond which the site preference of Fe was found to reverse. This order/disorder behavior as reported by the experimental studies mentioned above are in direct conflict with a large number of reports such as that of Heinemann *et al.*[17] obtained using single crystal diffraction studies, Mössbauer spectroscopic studies done on powdered olivine sample by Morozov *et al.*[3], results obtained by performing X-ray diffraction on single crystal olivine by Heinemann *et al.*[2] and more recently the results of Abdu *et al.*[19] obtained by performing Mössbauer spectroscopic studies on powdered samples. None of these studies find the

site preference of Fe to get reversed at elevated temperatures. Some of these studies (Heinemann *et al.* 1999, 2000) [2] [18] point out that the discrepancy between the findings by the group of Redfern *et al.* [1] [14] [16] and others lies in the incorrect correlation between the site occupancies and the cation thermal displacement parameters which have been used in the study by Redfern *et al.*[1] to derive the K_D values. Therefore although the atomic co-ordinates reported in the study by Redfern *et al.* [1] are essentially correct, the reported site occupancies are not. Arguments have been further provided in favour of the "no-cross-over" partitioning scenario by considering the temperature dependence of $\ln K_D$ known for other transition metal-Mg olivines.

In order to resolve this controversy we have performed a purely theoretical study on a 50 : 50 FeMgSiO₄ olivine using a combination of classical and quantum mechanical tools. To the best of our knowledge, no such theoretical studies have been attempted so far. The rest of the Chapter is organized as follows. We have constructed a lattice gas like model based on the crystal structure of olivine, which we use to address the problem of site preference. This is followed up by the result section consisting of several different sub-sections: we start with a discussion of changes in crystal structure upon increasing temperature, as reported by Redfern *et al.*[1] and Heinemann *et al.*[2], followed by description and comparison of the parameters of the lattice gas model extracted out of first-principles DFT calculations carried out on crystal structure data of Redfern *et al.* [1] and Heinemann *et al.* [2]. The next Subsection under the Results section describes K_D values obtained from our theoretical study and its comparison with existing experimental results. Finally we present our summary and conclusion.

4.2 Lattice Gas Model

Fig. 4.1 shows the olivine crystal structure projected on the bc plane. The zig-zag lines as seen in the figure connect M1 and M2 octahedral sites lying in the same plane. These planes are in turn stacked along the crystallographic a axis with little connection between them. Based on this crystal structure information, we introduce a 2D lattice gas model, to address the issue of site preference. We consider the olivine structure to be projected on to the 2D lattice in crystallographic bc plane, where we consider

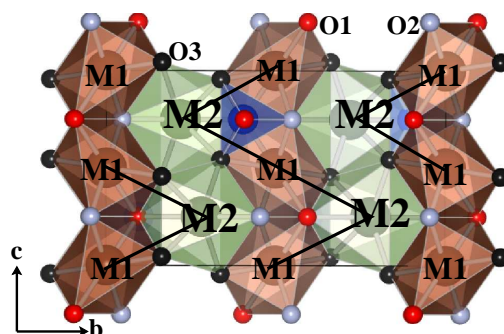


Figure 4.1 Crystal structure of olivine projected on the bc plane. Large, medium and small atoms respectively designate cations(Fe,Mg), Si and O atoms. The red(dark) octahedra are the $M1O_6$ octahedra and the green(light) octahedra are the $M2O_6$ octahedra. The three distinct oxygen atoms O1, O2, O3 have been marked. The solid lines depict zig-zag chains connecting nearest neighbour M1 and M2 octahedra.

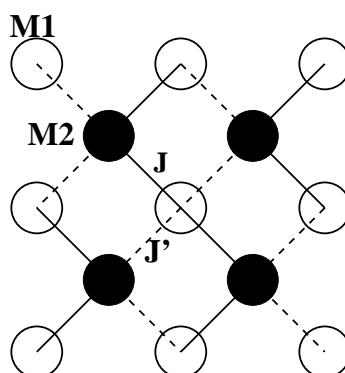


Figure 4.2 Schematic diagram of olivine projected on bc plane with silicon and oxygen degrees of freedom integrated out. The open circles represent M1 sites and filled circles correspond to M2 sites.

only the M cationic sublattice, as that is the relevant lattice for site preference. The Si and O degrees of freedom have not been considered explicitly. These degrees of freedom are assumed to be taken into account in quantum chemical calculation of the parameters of the model. As mentioned above, since the olivine structure is almost layered with little connection between out of plane metallic sites, such an approximate model is expected to capture the basic phenomena.

Fig.4.2 shows the 2D model under consideration. The bold line is indicative of the zig-zag chain formed by nearest neighbor M1 and M2 sites. The interchain M1-M2 neighbours as indicated by dotted lines, form second near neighbour pairs. We model the site preference of Fe on this lattice within an Ising like spin model. We consider a pseudo-spin variable $S_i = \pm 1$, with $S_i = +1(-1)$ denoting Fe(Mg). A model Hamiltonian involving the pseudo spins can, then be written as follows:

$$H = J \sum_{ij} S_i S_j + J' \sum_{ij'} S_i S_{j'} - h \sum_i S_i - h_s \left(\sum_{i \in M1} \frac{1 + S_i}{2} - \sum_{i \in M2} \frac{1 + S_i}{2} \right) + C. \quad (4.2)$$

Here ,

$J \Rightarrow$ is the chemical interaction energy between the first nearest neighbours, denoted by i and j , and

$J' \Rightarrow$ is the chemical interaction energy between second nearest neighbours denoted by i and j' .

The chemical interactions between Fe and Mg are expected to be short-ranged. The interactions beyond second nearest neighbors are therefore neglected. The sign of J and J' decide whether similar or opposite kinds of pseudo spins (representing Fe and Mg) are preferable as first and second nearest neighbours, respectively.

$h \Rightarrow$ The third term in the expression, involving h is a magnetic field like term, which gives the difference of chemical potential between Fe and Mg. For Fa50 where the Fe-Mg ratio is 50 : 50, the contribution from this term vanishes.

$h_s \Rightarrow$ The fourth term in the expression, represents the site preference, the magnitude of site preference being given by the parameter h_s . The positive value of h_s indicates Fe having preference for M1 site and the negative value indicates the opposite. All the factors that are believed to be responsible for the cation ordering such as the metal-O covalency [12] and the geometrical size effect are considered to be captured by h_s .

$C \Rightarrow$ is a constant which sets the zero of the energy.

4.3 Results

4.3.1 Variation in crystal structure of olivine with increasing temperature

We first examine how the crystal structure of 50-50 olivine varies with temperature as determined experimentally. There are only two crystal structure data available in the literature where the variation of the crystal structure with temperature has been reported over a wide range, namely, by Redfern *et al.* [1] and Heinemann *et al.* [2].

In Fig. 4.3 and Fig. 4.4 compare the structural parameters of our interest namely the volumes of $M1O_6$ and $M2O_6$ octahedra extracted out of the crystal structure data obtained by Heinemann *et al.* [2] and Redfern *et al.* [1]. Considering the crystal structure of Heinemann *et al.* [2] the M1-O and M2-O octahedral volumes are seen to increase monotonically as temperature is increased. A plot of the difference in M1-O and M2-O volumes with temperature (Fig. 4.4) is hence found to be more or less flat and featureless, apart from small fluctuations at higher temperatures. The crystal structure data measured by Redfern *et al.* [1] produces the $M1O_6$ volume that increases at a slower rate compared to $M2O_6$ octahedral volume below $\sim 600^\circ\text{C}$, beyond which it increases faster than that of $M2O_6$ octahedral volume, leading to the conclusion that the thermal expansion of $M1O_6$ and $M2O_6$ octahedra reverses at a critical temperature. As a result the difference in $M1O_6$ and $M2O_6$ octahedral volumes exhibits a minima around $\sim 600^\circ\text{C}$ as shown in Fig. 4.4.

4.3.2 Determination of the parameters of the model Hamiltonian from quantum mechanical total energy calculations

To determine the values of the parameters h_s, J, J' and C [26], we have carried out DFT calculations for four different configurations of M1 and M2 sites in a Fa50 olivine as shown in Fig. 4.5. The energies hence obtained for these four configurations are then substituted in the model Hamiltonian which are solved to determine the four unknown parameters h_s, J, J' and C . DFT total energies for configurations as shown in Fig. 4.5 (marked as U1-U4) on DFT optimized crystal structure at $T = 0\text{K}$ give rise to values:

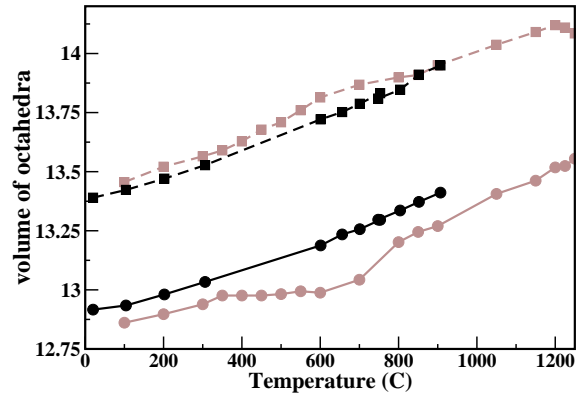


Figure 4.3 Temperature(in degree C) dependence of volume of M1 and M2 octahedra (in ³). The black(dark) curves are from Heinemann *et al.* [2] crystal structure data and the brown(light) curves are for Redfern *et al.* [1] crystal structure data. Solid(dashed) lines connecting data points represented as circles(squares) represent M1(M2) volumes respectively.

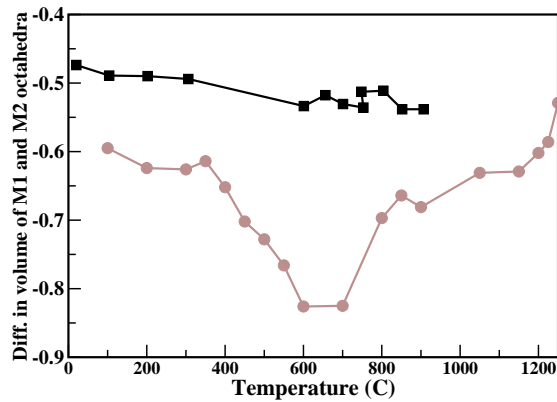


Figure 4.4 Difference in volume between M1 and M2 octahedra (in ³) vs temperature (in degree C). Black(dark) and brown(light) curves represent the data points corresponding to Heinemann *et al.* [2] and Redfern *et al.*'s [1] crystal structure data respectively.

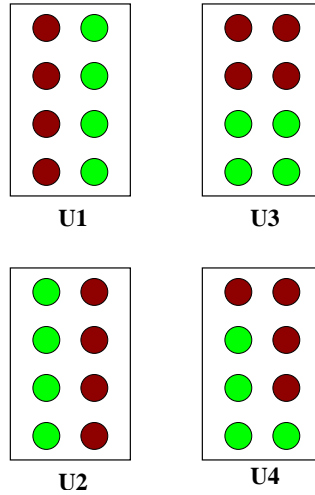


Figure 4.5 Four different configurations of the olivine unit cell. The first column in each cell represents M1 sites, whereas the second column represents M2 sites. Fe and Mg atoms have been marked with red and green respectively.

$$h_s=0.021\text{eV}, J=0.003\text{ eV}, J'=0.001\text{ eV and } C=-218.288\text{ eV}.$$

Hence keeping aside the parameter C which sets the zero of the energy, we find that the value of h_s which is an order of magnitude larger than that of J and J' , has the dominating effect. This trend has been also previously seen in another mineral which is also a major constituent of the upper mantle of the earth, namely, garnet[24].

Within DFT, we are unable to produce the temperature dependent crystal structure data which demands computer extensive ab-initio molecular dynamics by Car-Parinello [25]. In the next step, we therefore recalculate h_s , J , J' and C over a wide range of temperature using the crystal structure data of Redfern *et al* [1] and Heinemann *et al* [2].

Fig. 4.6 shows the variation of J , J' and h_s as a function of temperature for the two different sets of crystal structure data as provided by Redfern *et al* [1] and Heinemann *et al* [2]. The parameter h_s is found to follow roughly the same variation as the volume difference of M1-M2 octahedra, while the parameter J exhibits weak temperature dependence. The second nearest neighbour interaction J' , though, shows some variation, particularly for the crystal structure data by Redfern *et al* [1].

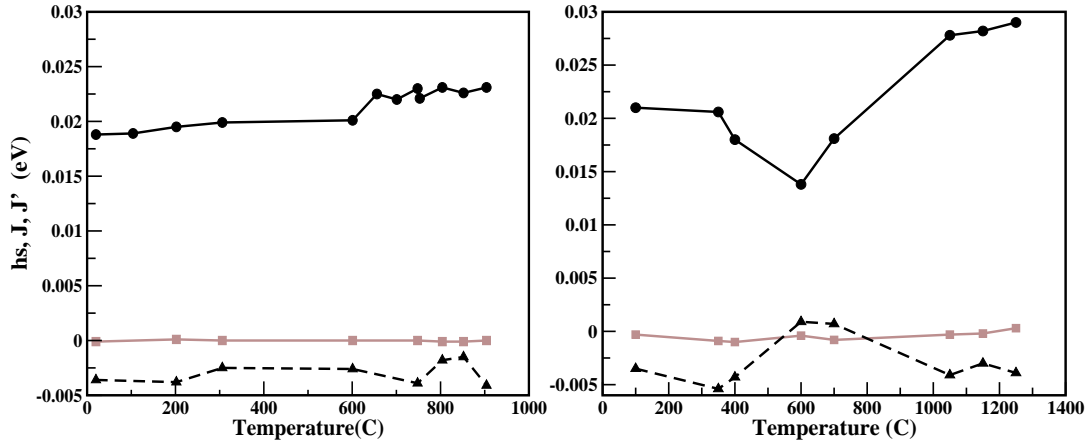


Figure 4.6 Variation of h_s , J , J' as a function of temperature (in °C), as given by Heinemann *et al* [2] crystal structure data(right) and Redfern *et al* [1] crystal structure data(left). Black-solid curve(dark-solid) represents h_s , brown(light) curve represents J and black-dashed(dark-dashed) curve represents J' in both the graphs.

4.3.3 Determination of K_D value from MC simulation

Considering the constructed lattice gas model with inputs from first-principles total energy calculations, we performed Monte Carlo (MC) simulations to find out K_D at various temperatures.

The calculated $\ln K_D$ values are shown in Fig. 4.7. For comparison, we also plot the $\ln K_D$ values as obtained by Redfern *et. al.* [1] and Heinemann *et. al.* [2]. Our results are found to be in clear conflict with Redfern's work [1] which indicates a crossover partitioning of Fe at 600°C (positive and negative values of $\ln K_D$ indicates preference towards M1 and M2 sites respectively). Our results on the other hand indicates that all throughout the temperature range Fe segregates into M1 site which follows the trend suggested by Morozov *et. al.* and Heinemann *et al* [2].

The site preference of Fe in olivine is decided upon by two competing factors, the Fe-O covalency and the geometric size effect. The co-valency effect prefers the occupancy of Fe at M1 site, while the geometric size effect prefers the occupancy of Fe^{2+} which is larger in size compared to Mg^{2+} , at M2 site [12]. Considering the crystal structure data of Redfern *et al* [1], at very low and very high temperatures the size difference between M1 and M2 is not significant. As a result co-valency is the dominant factor

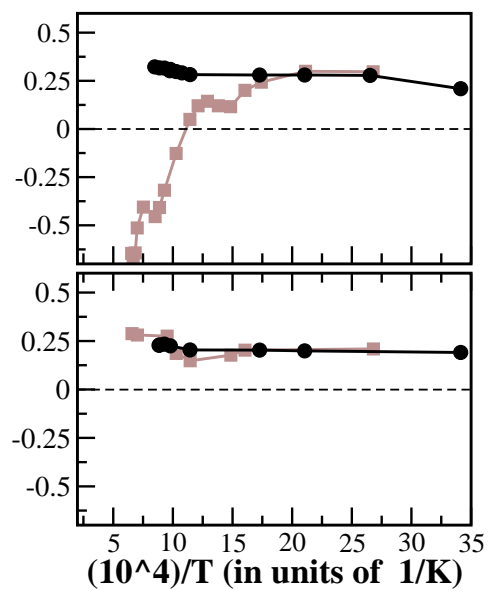


Figure 4.7 Variation of $\ln K_D$ with inverse of Temperature (in K^{-1}). The upper panel shows the experimentally determined values whereas the lower panel gives our theoretically obtained values for $\ln K_D$ obtained using experimental crystal structure data measured by Redfern *et al* [1] and Heinemann *et al* [2] at various temperatures. In both the graphs the black(dark) curve represents Heinemann *et al* and the brown(light) curve represents Redfern.

and makes Fe prefer M1 site, whereas at intermediate temperatures, 600°C , the volume difference becomes larger, which makes the geometry effect comparable to the co-valency effect of M1 site. This results in a dip in $\ln K_D$ value signaling increase of disorder. The disorder at 600°C is also reflected by J and J' values which are of opposite sign in this region, though their magnitude are significantly small. However, nowhere in the whole temperature range does the size difference between M1 and M2 become so large so as to cause a flip in the site preference of Fe. Consideration of the crystal structure data of Heinemann *et al* [2] results into much more flatter $\ln K_D$ vs T_{-1} , curve reflecting the relatively less temperature-sensitive crystal structure data.

4.4 Summary and Conclusions

In this study we have shown that accurate ab-initio calculations can be used to predict the nature of the partitioning of cations in mixed olivines. Going beyond our earlier work [12] on this subject we have now tried to examine whether the site-preference of the cations undergo a reversal with increase in temperature as has been suggested in literature [1]. For this we have used a Monte Carlo scheme with inputs from ab-initio calculations, which fix the basic interactions, determined on the measured crystal structure data. Using the data of Redfern *et al.* [1] we show that although, the value of K_D which quantifies the site preference, appears to decrease, initially with temperature, it goes through a minimum around $T = 600^{\circ}\text{C}$ and recovers to its zero temperature value on further increase of temperature producing a variation in $K_D(\ln K_D)$ value but always keeping it greater than 1(positive) signaling a small but finite preferential site occupancy of Fe at M1 site all throughout the temperature range. On the other hand, the crystal structure data of Heinemann *et al* [2] produces a more or less temperature insensitive K_D value of slightly larger than 1. Our results therefore agree with the experimental findings of Heinemann *et al* [2] and Morozov *et al.* [3] that there does not seem to exist any cross-over partitioning in mixed Fe-Mg olivine system. We however need to remember that the site occupancy in mixed Fe-Mg olivine system involves small energies given the fact that the size difference of M1O_6 and M2O_6 octahedra is small as opposed to the case of pyroxene. Accurate determination of crystal structure as a

function of temperature is therefore important. Ideally, one may carry out structural optimization of the free energy to obtain the theoretically derived crystal structures at various temperature. The use of classical pair-like potentials appear promising in that respect since fully quantum Car-Parrinello molecular dynamics is prohibitively expensive due to that large unit cell and complexity of the system. However, we are faced with the difficulty that none of the currently available classical potential are successful in capturing the required covalency effect that derives the site preference of Fe^{2+} ion towards M1 [12]. Work is in progress trying to improve upon the existing classical potentials. Finally, even if equilibrium state has $K_D > 1$ at all temperatures, metastable $K_D < 1$ states may become long-lived and easily accessible at higher temperatures particularly if the crystal data drives a significant variation in K_D value. It is therefore possible that the sample preparation procedures may tilt the balance one way or the other which may produce an out of equilibrium sample with $K_D < 0$.

Bibliography

- [1] S. A. T. Redfern, G. Artioli, R. Rinaldi, C. M. B. Henderson, K. S. Knight, B. J. Wood, *Phys. Chem. Minerals* **27**, 630-637 (2000).
- [2] R. Heinemann, H. Kroll, A. Kirfel, B. Barbier, *Eur. J. Mineral.* **18**, 673-689 (2006).
- [3] M. Morozov, C. Brinkmann, W. Lottermoser, G. Tippet, G. Amthauer, H. Kroll, *Eur. J. Mineral.* **17**, 495-500 (2005).
- [4] J. Ganguly and V. Tazzoli, *Am. Mineral.* **79**, 1053-1067 (1994); Kroll H., Schlenz H., Phillips M.W., *Phys. Chem. Minerals* **21**, 555-560 (1994).
- [5] H. Kroll and R. Knitter, *Am. Mineral.* **76**, 928-941 (1991).
- [6] F. A Seifert and D. Virgo, *Science* **188**, 1107-1109 (1975).
- [7] A. Putnis, *An introduction to mineral sciences*, Cambridge University Press, Cambridge (1992).
- [8] The order-disorder process in olivine is called non-convergent because M1 and M2 sites do not converge to symmetry equivalence even when Fe²⁺ and Mg²⁺ become randomly disordered.
- [9] H. E. Huppert, R. S. J. Sparks, *Earth planet. Sci. Lett.* **92**, 397-405 (1989).
- [10] F. G. F. Gibb, C. M. B. Henderson, *Contr. Miner. Petrol.* **109**, 538-545 (1992); B. D. J. Marsh, *Petrol.* **30**, 479-530 (1989).
- [11] S. A. T. Redfern, C. M. B. Henderson, B.J. Wood, R. J. R. Harrison, K. S. Knight, *Nature* **38**, 407 (1996).

- [12] S. Chatterjee, S. Sengupta, T. Saha-Dasgupta, K. Chatterjee, N. Mandal, *Phys. Rev. B* **79**, 115103 (2009).
- [13] J. R. Smyth, R. M. Hazen, *Am. Mineral.* **58**, 588-593 (1973).
- [14] G. Artioli, R. Rinaldi, C. C. Wilson, P. F. Zanazzi, *Am. Mineral.* **80**, 197-200 (1995).
- [15] R. Rinaldi, C. C. Wilson, *Solid State Communications* **97**, 395-400 (1996).
- [16] R. Rinaldi, G. Artioli, C. C. Wilson, G. McIntyre, *Phys Chem Minerals* **27**, 623-629 (2000).
- [17] R. Heinemann, H. Kroll, A. Kirfel, B. Barbier, *Eur. J. Mineral.* **15**, Bh.1, 78 (in German) (2003).
- [18] R. Heinemann, V. Staack, A. Fischer, H. Kroll, V. Thomas, A. Kirfel, *Am. Mineral.* **84**, 1400-1405 (1999).
- [19] Y. A. Abdu, H. Annersten, T. Ericsson, F. C. Hawthorne, *Hyperfine Interact.* **186**, 99-103 (2008).
- [20] S. Chatterjee, T. Saha-Dasgupta, *Phys. Rev. B* **81**, 155105 (2010).
- [21] G. Kresse and J. Hafner, *Phys. Rev. B* **47**, 558(1993); G. Kresse and J. Furthmuller, *Comput. Mater. Sci.* **6**, 15 (1996); G. Kresse and J. Furthmuller, *Phys. Rev. B* **54**, 11169 (1996).
- [22] J. Hubbard, *Proc. R. Soc. London, Ser. A* **276**, 238-257 (1963).
- [23] K. Binder, D. W. Heerman, *Monte-Carlo simulation in statistical physics :An Introduction*, Springer, Berlin (2002).
- [24] J. Ganguly, W. Cheng, H. ST. C. O'Neill, *Am. Miner.* **78**, 583-593 (1993).
- [25] R. Car, M. Parinello, *Phys. Rev. Lett.* **55**, 2471-2472 (1985).
- [26] Contribution for h vanishes for 50 : 50 Fe-Mg olivine.

Chapter 5

First-principles Simulations of Structural, Electronic and Magnetic properties of vacancy bearing Fe silicates

The phenomenon of charge ordering, which is generally observed in highly correlated materials involving transition metals, has drawn the attention of physicists since the days when it was first observed in 1939 by Verway in magnetite. This is because it encompasses within itself a number of novel and interesting phenomena, such as increase in electrical resistivity, superconductivity and colossal magnetoresistance. Anticipating the importance of charge ordering, in this chapter, we present our study of a charge ordered mineral, known as laihunite, which is an oxidation product of fayalite(Fe_2SiO_4). We have simulated the lattice structure of laihunite by introducing appropriate number of vacancies at the cationic sites as demanded by the reported chemical formula of laihunite and studied its structural, electronic and magnetic properties using first principle density functional theory(DFT). Our DFT simulated structure (which is compositionally close to naturally occurring laihunite compound) shows good agreement in the general trend in the change of Fe_2SiO_4 crystal structure upon vacancy introduction. Our study shows that the introduction of vacancy creates charge disproportionation of Fe ions into

This chapter is based on *Phys Chem Miner.* **38** 259 (2011)

Fe²⁺-like and Fe³⁺-like ions with a charge difference larger than 0.5, keeping the valences of other ions unaltered. Fe²⁺-like ions are found to occupy octahedral sites of specific symmetry while Fe³⁺-like occupy the other leading to charge ordering at zero temperature. We also study the magnetic ordering of Fe ions.

5.1 Introduction

As already discussed, the octahedral sites in olivine in general can be occupied by divalent cations M²⁺ (e.g. Fe²⁺, Mg²⁺, Co²⁺, Mn²⁺). Large number of studies have addressed site occupancies and ordering of divalent octahedral cation in olivines [8, 9, 10, 11]. We have also addressed the site preference problem in Mg-Fe olivine using first principles density functional calculations[12], as presented in chapter 3. In contrast, much less studies have been carried out for minerals bearing significant quantities of trivalent cations at the octahedral sites. Laihunite[13, 14, 15], an intermediate temperature oxidation product of fayalite[7](Fe₂SiO₄), which is the Fe rich end member of (Mg,Fe)₂SiO₄, is the best known example of such mineral. Published literature on laihunite compounds are of varying composition, but follow the general formula [16] □_xFe_{2-x}SiO₄ where □ represents vacancies and *x* can range from 0.24 to 0.5. To the best of our knowledge, though there exists few experimental studies on laihunite, the theoretical studies in understanding this defect structure are minimal. This class of mineral is particularly interesting since it provides the interesting situation of mixed valency of Fe ions, leading to possibility of charge disproportionation and charge ordering at Fe site that has drawn the attention of physicists since years, for example in the case of magnetite (Fe₃O₄)[17] and manganites (e.g. La_{0.5}Ca_{0.5}MnO₃[18]). In this chapter, we present a detailed study of the structural, electronic and magnetic properties of laihunite with *x*=0.5. For this purpose we start with a pure fayalite mineral with formula Fe₂SiO₄, in which we introduce vacancies to arrive at a compound with chemical formula □_{0.5}Fe_{1.5}SiO₄. The site preference of vacancy formation is determined through first-principles DFT calculations. Strong electron-electron correlation effect and the magnetism at Fe site in high spin state is achieved through the local spin density approximation (LSDA)+U calculations, as already explained

Table 5.1 Energy required for creation of vacancy at different atomic sites of fayalite.

site	energy(eV)	site	energy(eV)
M1	6.65	O1	9.99
M2	9.17	O2	9.80
Si	10.92	O3	9.86

in the Methodology section. The crystal structure of the vacancy introduced fayalite is then optimized to generate the crystal structure of laihunite. The electronic structure of the optimized structure has been studied in detail in terms of charge disproportionation and charge ordering at Fe sites. We also study the underlying magnetic ordering.

The following section contains the results of our first principles simulation which is divided into several sub-sections. Section II A describes the study of the site preference of vacancy formation while section II B describes the optimized crystals structure of laihunite, which is formed upon introduction of vacancies into fayalite. Section II C describes the electronic and magnetic structure of laihunite as calculated within the framework of DFT. The chapter concludes with discussion and summary in section III.

5.2 Results

5.2.1 Site preference of vacancy

Fayalite, an olivine structured mineral can be viewed as a distorted hexagonal close packed (HCP) array of oxygen ions (shown in Fig. 5.1A), with half of the octahedral sites and one-eighth of the tetrahedral sites occupied by Fe and Si respectively. As already discussed in chapter 3, an olivine structure mineral has two symmetry distinct octahedral sites: M1, on a centre of symmetry and M2, on a mirror plane. There is only one distinct tetrahedral site, and three distinct oxygen sites, O1 and O2 on the mirror plane and O3 in a general position. Fig. 5.1B shows the crystal structure of fayalite with all the inequivalent atoms marked. The formation energy of a single vacancy, i.e, the energy associated with

removing a single ion from the lattice to an isolated state, calculated using LSDA+U total energies with plane wave basis are tabulated in Table I for vacancies created on different sites of pure fayalite. The theoretical background for calculation of vacancy formation energy has been dealt with in great detail in chapter 2 of this thesis. We have employed Eqn 2.126 of chapter 2 while calculating the vacancy formation energy. As it is clearly seen from Table I, M1 site is the most preferred site for vacancy creation, followed by M2 site, while the most difficult site to create vacancy is Si. Among the oxygen sites, O2 is found to be more favorable compared to O3 and O1. The formation energies quoted in Table I, were obtained by considering single vacancy in one unit cell of fayalite. We have checked the reliability of our result by considering a supercell of $2 \times 2 \times 2$, the general trend is found to be the same. The computational effort prohibits us to go to larger supercells. In principle, to get an accurate estimate of vacancy formation energy, one should carry out calculations with increasing dimension of the cell and check the convergence of the defect energy. Since we are interested in finding out the general trend in terms of the most favorable position for vacancy formation rather than an accurate estimate of vacancy formation energy, the calculated numbers using one unit cell serve our purpose. The previous calculations [26] for Forsterite (Mg_2SiO_4) using atomistic method of modeling with interatomic potentials which carefully checked the convergence with increasing cell size also find M1 to be the most favorable position for vacancies.

5.2.2 Crystal structure of laihunite

In order to create laihunite with a formula $\square_{0.5}\text{Fe}_{1.5}\text{SiO}_4$ out of fayalite, one needs to introduce two vacancies in a unit cell of fayalite which contains four formula unit. Following our analysis presented in previous section, we choose M1 and M2 sites for creation of this double vacancies. There are in total four M1 sites and four M2 sites in a unit cell and double vacancies at M1 and M2 site can be created in six distinct ways. The distinct configurations are shown in Fig. 5.2 and the total energies corresponding to the optimized geometries of these configurations are listed in Table II. As found, in case of single vacancy, the creation of double vacancies is also favored at M1 sites. Analysis of configurations with double vacancies at M1 sites, show configuration 1 to be of lowest energy, while

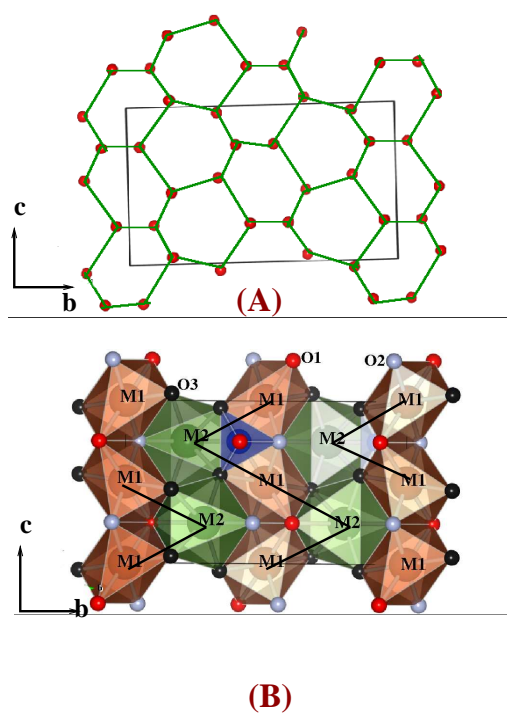


Figure 5.1 (A) Schematic diagram showing the approximate hexagonal closed packing of oxygen atoms in case of fayalite projected on to the bc plane. (B) The total structure of fayalite. Large, medium and small atoms designate Fe, Si and O atoms. The red (dark) octahedra are the $M1O_6$ octahedra and green (light) octahedra are $M2O_6$ octahedra. The three distinct oxygen atoms O1, O2 and O3 have been marked. The solid line depicts the zig-zag chain connecting the nearest neighboring M1 and M2 octahedra.

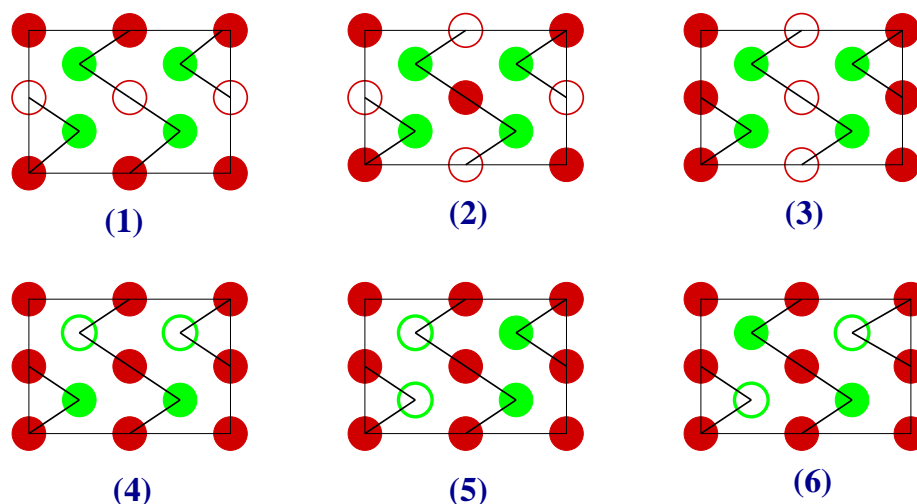


Figure 5.2 Schematic diagram showing different configurations with all possible ways in which two vacancies can be created at the metallic sites in fayalite. The Si and O degrees of freedom have been omitted out from the figure for clarity. Red (dark) and green (light) filled circles represent M1 and M2 sites respectively. The empty circles depict the vacant octahedral site.

the energy of the configuration where two vacancies sit in two neighboring M1 sites are significantly higher. This indicates that the vacancies do not favor cluster formation.

In the following, all the analysis are therefore carried out with configuration 1. The distortion of the HCP network of oxygen ions upon introduction of Fe^{2+} cations and Si ions at the octahedral and tetrahedral sites gives the fayalite crystal structure orthorhombic symmetry with $Pbnm$ space group. The introduction of vacancies in fayalite further reduces the symmetry. The optimized geometry in configuration 1 turned out to be that of triclinic. A comparison of the lattice constants between fayalite with and without vacancies show (see Table III) substantial contraction along b and c axis when vacancies are introduced, which as expected, leads to an overall reduction of the unit cell volume. While in fayalite there are six distinct classes of atoms, the lowering of symmetry in presence of vacancies gives rise to 14 different classes of atoms as listed in Table III. Table IV lists the corresponding atomic positions. Fig 5.3 shows the geometry optimized structure of configuration 1 with distinct class of various atoms marked. In case of fayalite the M2O_6 octahedra centered about Fe2 ions are larger in volume and

Table 5.2 Total energies corresponding to the six different configurations with double vacancies created at M1 and M2 sites in fayalite as shown in Fig. 5.2.

configuration	Energy(eV)	configuration	Energy(eV)
configuration1	-208.04	configuration4	-205.56
configuration2	-207.95	configuration5	-204.74
configuration3	-206.46	configuration6	-203.73

more distorted (measured in terms of root-mean-square deviation of the Fe-O bond length) compared to $M1O_6$ octahedra centered about Fe1 ion. The introduction of vacancies in case of $\square_{0.5}Fe_{1.5}SiO_4$ reverses this trend (see Table V), in the sense that the $M2O_6$ octahedra occupied by Fe3 and Fe4 become smaller in volume compared to $M1O_6$ occupied by Fe1 and Fe2. In Table V we also list these quantities corresponding to only available [13] crystal structure data of laihunite of composition $\square_{0.4}Fe_{1.6}SiO_4$. We find that although the concentration of the vacancies are different between computed configuration 1 and experimentally measured crystal, the general trend in terms of comparison of bond lengths and distortions between $M1O_6$ and $M2O_6$ octahedra show good agreement with each other. The lattice constants ($a=4.81 \text{ \AA}$, $b=10.19 \text{ \AA}$ and $c=5.80 \text{ \AA}$) and volume [$283.9 (\text{Å})^3$] of $\square_{0.4}Fe_{1.6}SiO_4$ also show good agreement with that of geometry optimized configuration 1 of $\square_{0.5}Fe_{1.5}SiO_4$ ($a=4.77 \text{ \AA}$, $b=10.08 \text{ \AA}$, $c=5.73 \text{ \AA}$ and volume = $275.1 (\text{Å})^3$).

5.2.3 Electronic and Magnetic Structure of fayalite with double vacancies at the metallic sites.

Basic Electronic structure- In this section we describe the electronic structure of configuration 1 which is basically the fayalite structure with double vacancies at M1 sites. In fayalite, the Fe atoms are found to be in high spin state, with a magnetic moment of $3.6 \mu_B$

Fig. 5.4A presents the LSDA+U density of states for the vacancy bearing fayalite in configuration 1 projected onto Fe-d, O-p and Si-sp states. The zero of the energy scale is set at the top of the valence band. It can be seen that there is negligible contribution from Si to the occupied part of the DOS. States

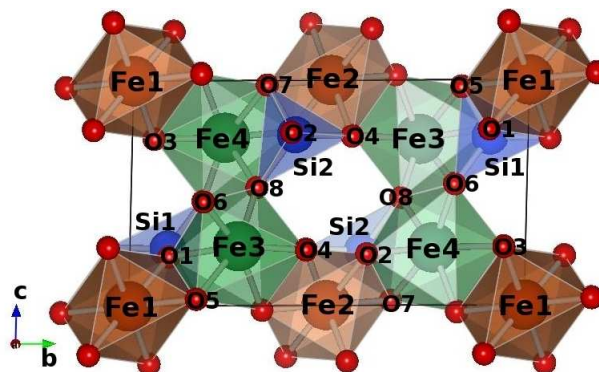


Figure 5.3 Optimized structure of configuration 1. The various categories of inequivalent atoms have been marked.

Table 5.3 The lattice constants and Wyckoff positions for each species for Fayalite in orthorhombic space group and configuration 1 in triclinic space group.

	$a(\text{Å})$	$b(\text{Å})$	$c(\text{Å})$	atom	class	coordinates
Fayalite	4.82	10.47	6.07	Fe1	4a	$(0,0,0), (1/2, 1/2, 0), (0,0, 1/2),$ $(1/2, 1/2, 1/2)$
				Fe2, Si, O1, O2	4c	$(x, y, 1/4), (x+1/2, -y+1/2, 3/4),$ $(-x, -y, 3/4), (-x+1/2, y+1/2, 1/4)$
				O3	8d	$(x, y, z), (x+1/2, -y+1/2, -z),$ $(-x, -y, z+1/2), (-x+1/2, y+1/2, -z+1/2),$ $(-x, -y, -z), (-x+1/2, y+1/2, z),$ $(x, y, -z+1/2), (x+1/2, -y+1/2, z+1/2)$
config. 1	4.77	10.08	5.73	Fe1	a	$(0,0,0)$
				Fe2	e	$1/2, 1/2, 0$
				Fe3, Fe4, Si1, Si2, O1	2i	$(x, y, z), (-x, -y, -z)$
				O2, O3, O4, O5, O6, O7, O8		

Table 5.4 Crystal structure data for configuration1.

	space group	a(A ⁰)	b(A ⁰)	c(A ⁰)	alpha	beta	gamma
	P-1	4.76656	10.07953	5.72763	88.5041	90	90
ATOM	X	Y	Z	ATOM	X	Y	Z
Fe1	0.0000	0.0000	0.0000	Fe2	0.5	0.5	0.0
Fe3	0.9923	0.2712	0.2596	Fe4	0.4923	0.2287	0.7403
Si1	0.4397	0.0943	0.2501	Si2	0.9397	0.4056	0.7498
O1	0.2233	0.8953	0.7627	O2	0.2766	0.3953	0.7627
O3	0.3252	0.9429	0.2381	O4	0.1747	0.4429	0.2381
O5	0.2721	0.1696	0.0276	O6	0.2984	0.1791	0.4592
O7	0.7721	0.3303	0.9723	O8	0.2015	0.6791	0.4592

Table 5.5 Structural comparison between fayalite, laihunite and vacancy bearing fayalite in configuration 1(double vacancies at M1 sites).

	Fayalite(Fe ₂ SiO ₄)	Laihunite	configuration1
M1-O (av. Bond length) (A ⁰)	2.15	2.19	2.11
volume of octahedra ((A ⁰) ³)	13.25	14.01	12.53
M1-O(RMS deviation)	0.05	0.07	0.06
M2-O (av. Bond length) (A ⁰)	2.18	2.04	2.02
volume of octahedra ((A ⁰) ³)	13.81	11.32	10.99
M2-O(R.M.S deviation)	0.10	0.09	0.08

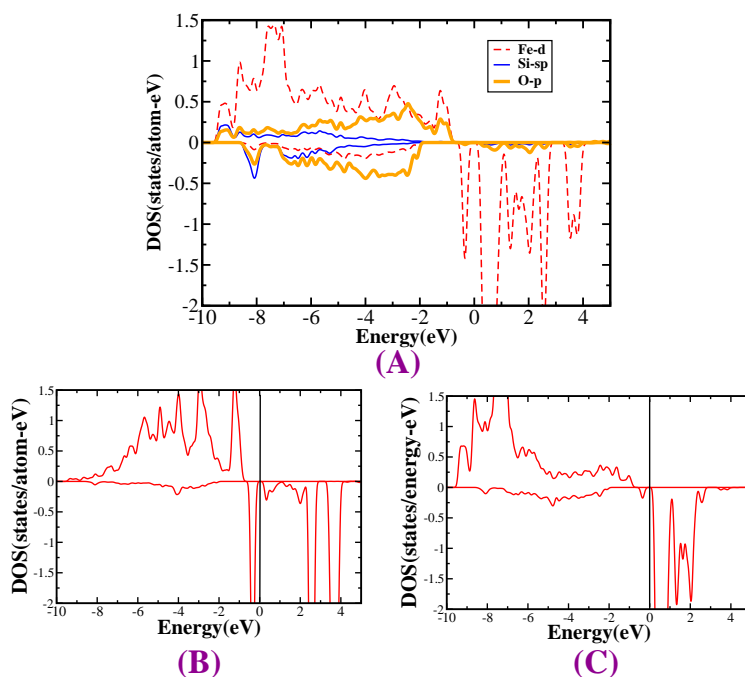


Figure 5.4 (A) Partial density of states for configuration1 as shown in Fig. 5.2 projected onto Fe-d, O-p and Si-sp states;(B) Partial DOS showing the Fe-d orbital for Fe at M1 site; (C) Partial DOS of Fe-d orbital for Fe at M2 site. Within each panel the upper(lower) sub-panel corresponds to majority(minority) spin. The negative of DOS has been plotted for the minority spin channel. The zero of the energy is set at the LSDA+U calculated Fermi energy (drawn as vertical dashed lines in (B) and (C)).

close to the Fermi level are dominated basically by O-p and Fe-d where they strongly hybridize. The d-p hybridized band extends from -9.5 eV to 4 eV.

Figs. 5.4B and 5.4C show the Fe-d density of states projected onto Fe1 and Fe2 atoms occupying M1 sites and Fe3 and Fe4 atoms occupying M2 sites, respectively. Focusing onto down spin channel, it is found to be nearly empty for Fe atoms occupying M2 sites while it is partially filled for atoms occupying M1 site. This gives rise to charge disproportionation between Fe ions occupying M1 (two in number) and M2 sites (four in number), with those occupying M1 sites being close to Fe^{2+} and those occupying M2 sites being close to Fe^{3+} . The charge difference between the two are found to be about 0.55. This leads us to conclude that the Fe ion in mixed valence state $\text{Fe}^{2.67+}$ in $\square_{0.5}\text{Fe}_{1.5}\text{SiO}_4$,

charge disproportionates in following matter: $6 \text{Fe}^{2.67+} \rightarrow 4 \text{Fe}^{3+} + 2 \text{Fe}^{2+}$. The magnetic moments of Fe sites occupying M1 and M2 sites are found to be $3.7 \mu_B$ and $4.3 \mu_B$ respectively, supporting the charge disproportionation between M1 and M2 sites. The preferential occupancy of Fe^{2+} like ions into M1 sites and that of Fe^{3+} like ions into M2 sites give rise to a charge ordered pattern as shown in Fig. 5.5. The charge density has been calculated in a narrow energy window close to the Fermi-level. Within this energy range, there is negligible contribution from Fe at M2 (which is close to the 3+ state), whereas for Fe at M1 (which is close to the 2+ state) there is a sharp peak in the down spin channel of the d-orbital. This peaking as already stated, is due to the presence of a single electron in the down spin channel for Fe1 and Fe2 in high spin d^6 -configuration. The charge density calculated in this energy interval therefore shows the accumulation of charge around M1 site, whereas the M2 site remains devoid of any charge. This charge ordering is driven by the structural distortion that happens due to introduction of vacancy. In our earlier communication we have shown that for a mixed Fe-Mg olivine system, Fe^{2+} prefers to occupy the smaller sized M1 sites which is driven by the delicate balance between size consideration and co-valency effect. While the Fe-O co-valency is similar between Fe^{2+} and Fe^{3+} , their ionic sizes are rather different: Fe^{2+} cation (0.76 \AA) is larger than Fe^{3+} cation (0.65 \AA). The introduction of vacancies on the other hand reduces the volume of M2O_6 octahedra substantially, making them smaller compared to M1O_6 octahedra. It is therefore mere size consideration that dictates the preference of M2 sites by Fe^{3+} like ions and M1 sites by Fe^{2+} like ions.

Magnetic Ordering- Finally, we turn on to magnetic ordering of Fe ions. The magnetic interaction between partially filled Fe ions mediated by oxygen ions are expected to be super-exchange driven anti-ferromagnetic interaction. In case of fayalite the antiferromagnetic order has been confirmed both experimentally and theoretically [28, 6]. There are however two anti-ferromagnetic configurations that are possible as shown in Fig. 5.6. In one case (configuration A) the Fe spins within the zig-zag chain consisting of neighboring M1-M2 sites are anti-ferromagnetically aligned while the inter-chain interaction is ferromagnetic. In the second case (configuration B), the intra-chain interaction is ferromagnetic while the inter-chain interaction is anti-ferromagnetic. The total energies corresponding

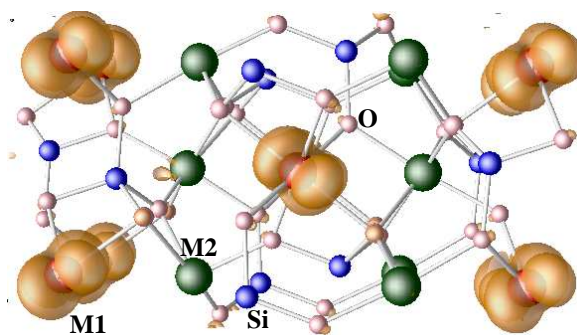


Figure 5.5 (Color on-line) Charge density plot for fayalite with double vacancies at M1 sites as in configuration 1. Contour height is set at $0.004/\text{Å}^3$.

to both magnetic configuration A and B are listed in Table VI corresponding to different vacancy configurations. In all case, the magnetic configuration B, which satisfies AFM inter-chain interaction between corner sharing FeO_6 octahedra and FM intrachain interaction between edge sharing FeO_6 octahedra are found to be stable. The same magnetic arrangement was obtained also for pure fayalite compound [6]. Note, this leads to strong AFM $\text{Fe}^{3+}\text{-O-Fe}^{3+}$ superexchange between corner-shared, interchain M1O_6 and M2O_6 octahedra while the edge-shared interactions between M1O_6 and M2O_6 octahedra within a given chain remains FM. Though the strong AFM nature of interchain $\text{Fe}^{3+}\text{-O-Fe}^{3+}$ superexchange is in agreement with the predictions of Kan and Coey [29], our DFT predicted magnetic configuration is different from that by Kan and Coey, which would lead to magnetic configurations with no specific spin arrangement within a given chain. We found that the magnetic structure proposed by Kan and Coey to be about 160 meV higher in energy than that given by the DFT predicted ground state magnetic structure (config. B).

5.3 Conclusion

We have carried out first-principles calculation of fayalite compound upon introduction of vacancy. Our study consists of structural optimization, study of electronic and magnetic structure. Our first-principles optimized geometry with two vacancies introduced at preferred M1 cationic sites in a unit cell of four

Table 5.6 Total energy of the three structures with double vacancies at M1 sites in the two types of possible anti-ferromagnetic configuration as shown in Fig. 5.2.

configuration	AF order	
	configuration A energy(eV)	configuration B energy(eV)
configuration1	-208.48	-208.62
configuration2	-208.57	-208.70
configuration3	-206.92	-207.02

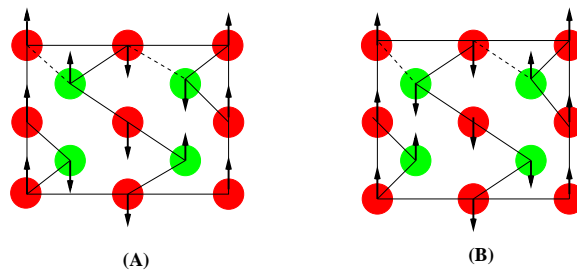


Figure 5.6 [The two possible anti-ferromagnetic order in fayalite] The two possible anti-ferromagnetic order in fayalite. Solid lines show the intra-chain and dashed lines show the inter-chain interactions. Red (dark) and green (light) filled circles represent M1 and M2 sites.

formula units leading to a chemical composition of $\square_{0.5}\text{Fe}_{1.5}\text{SiO}_4$ show good agreement with the structural details of naturally forming, vacancy bearing compound, laihunite of formula $\square_{0.4}\text{Fe}_{1.6}\text{SiO}_4$. This provides reliability of DFT calculations in description of complex minerals with defect structure. The study of electronic structure shows that the introduction of vacancy leads to charge disproportionation at Fe site, with Fe^{2+} like ions occupying octahedra of site symmetry M1 of the fayalite lattice and Fe^{3+} like ions occupying octahedra of site symmetry M2 of the fayalite lattice. This is caused by the specific site preference of the vacancy formation and the accompanying structural relaxation, which reverts the size relationship between M1O_6 and M2O_6 octahedra of the original fayalite lattice. The preferential occupancy of Fe^{2+} like and Fe^{3+} like ions in M1 and M2 sites leads to charge ordering within the zig-zag chain of M1-M2 at $T=0\text{K}$ which are found to be antiferromagnetically ordered. Finally, our first-principles prediction of charge ordered state in laihunite lists this compound in the category of compounds with interesting charge ordering properties like like manganites and magnetites, which should be experimentally verified. This may lead to study of charge order-disorder transition as a function of temperature, possible melting of charge-ordered phase by electric field to name a few. From the point of view of geological interest, our study will form the basis of study of vacancy diffusion in Fe bearing olivines, known as the transition metal extrinsic diffusion [30]. This kind of diffusion is determined by both chemical potential and temperature as opposed to pure intrinsic or extrinsic diffusion and therefore depends on the ratio of Fe^{2+} and Fe^{3+} which would change dynamically as the vacancy propagates. We present our study of vacancy diffusion in Fe containing olivines in the next chapter.

Bibliography

- [1] M. H. F. Sluiter, V. Vinograd and Y. Kawazoe, Phys. Rev. B **70** 184120 (2004).
- [2] R. M. Wentzcovitch, B.B. Karki, M. Cococcioni, S. de Gironcoli, Phys. Rev. Lett **92** 018501 (2004).
- [3] B. B. Karki, R. M. Wentzcovitch, S. de Gironcoli, S. Baroni, Phys. Rev. B **62** 14750 (2000).
- [4] B. B. Karki, M. C. Warren, L. Stixude, G. J. Ackland and J. Grain, Phys. Rev. B **55** 3465 (1997).
- [5] R. M. Wentzcovitch, J. L. Martins and G. D. Price, Phys. Rev. Lett **70** 3947 (1993).
- [6] M. Cococcioni, A. D. Corso, S. de Gironcoli Phys. Rev. B **67**, 094106 (2003).
- [7] J.R. Smyth, Am. Mineral. **60**, 1092 (1975).
- [8] S.A.T. Redfern, C.M.B. Henderson, K.S. Knight, B.J. Wood, European Journal of Mineralogy **9**, 287(1997)
- [9] S. Chakraborty, Journal of Geophysical Research-Solid Earth **102**, 12317(1997)
- [10] M. Müller-Sommer, R. Hock, A. Kirfel, Physics and Chemistry of Minerals **24**, 17(1997)
- [11] J. Chen, R. li, J.B. Parise, D.J. Weidner, Am. Mineral. **81**, 1519(1996)
- [12] S. Chatterjee, S. Sengupta, T. Saha-Dasgupta, K. Chatterjee, N. Mandal, Phys. Rev. B **79**, 115103(2009)

- [13] O. Tamada, B. Shen, N. Morimoto, *Mineralogical Journal* **11**, 382 (1983)
- [14] M. W. Schaefer, *Nature* **303**, 325(1983)
- [15] S. Matsuura, S. Sueno, N. Yurimoto, *Mineralogical Society of Japan, 1983 Annual Meeting Abstracts with Program*, **D29**, 118(1983)
- [16] D. E. Janney, J. F. Banfield, *Am. Mineral.* **83**, 799 (1998).
- [17] E. J. W. Verwey, *Nature* **144** 327 (1939); E. J. W. Verwey, P. W. Haayman and F. C. Romeijan, *J. Chem. Phys.* **15** 181 (1947).
- [18] S-W. Cheong, S-W. and H. Y. Hwang, in *Colossal Magnetoresistive Oxides*, *Monographs in Condensed Matter Science*. (ed. Tokura Y.) Ch. 7 (Monogr. In Condensed Matter Sci, Gordon and Breach, Reading, UK, 2000).
- [19] P. Hohenberg and W. Kohn, *Phys. Rev.* **136**, B864 (1964); W. Kohn and L. J. Sham, *Phys. Rev.* **140**, A1133 (1965).
- [20] G.Kresse and J.Hafner, *Phys. Rev. B* **47**, 558 (1993); G.Kresse and D.Furthmüller, *Comput. Mater. Sci.* **6**, 15 (1996); *Phys. Rev. B* **54**, 11169 (1996).
- [21] O.K. Andersen and O. Jepsen, *Phys. Rev. Lett.* **53**, 2571 (1984).
- [22] P.E Blöchl, *Phys. Rev. B* **50**, 17953 (1994); G.Kresse and D.Joubert, *ibid*, **59**, 1758 (1999).
- [23] J.Hubbard, *Proc. R. Soc. London A* **276**, 238 (1963).
- [24] V.I. Anisimov *et al.* *Phys. Rev. B* **48**, 16929 (1993).
- [25] W. Pickett *et. al.* *Phys. Rev. B* **58**, 1201 (1998); V. Anisimov *et. al.* *Phys. Rev. B* **54** 4387 (1996).
- [26] N.C. Richmond, J.P. Brodholt, *Am. Mineral.* **85**, 1155 (2000).
- [27] Since the octahedra are in general distorted, there are further splittings within individual t_{2g} and e_g blocks. They are, however, much smaller compared to t_{2g} - e_g splitting.

- [28] R. Müller, H. Fuess and P. J. Brown, *Journal de Physique*, Colloque C7, supplment au no.12, page C7-249 (1982).
- [29] X. Kan, J. M. D. Coey, *Am. Mineral.* **70**, 576 (1985).
- [30] Sumit Chakraborty, *Journal of Geophysical Research* **102**, 12317 (1997).

Chapter 6

Vizualizing frozen point defect tracks in Fe containing olivines.

Trajectories made by point defects, like vacancies, during migration potentially contain a wealth of valuable informations [1] about the environment within which diffusion has taken place. For instance, in the case of free diffusion, the tracks are nearly isotropic, while in the case of directed diffusion, which occurs in the presence of temperature or stress gradient, elongated tracks are produced. Infact, a study of diffusion tracks left by proteins on cell membrane[2] , is known to yield information about the cell cytoskeletal network.

But, the main challenge here lies in the direct, *in-situ* determination of the vacancy migration, which is known to be a difficult task. Hence, the other option is to look for indirect methods for determination of vacancy migration tracks. We have devised one such indirect method using a combination of first-principles calculation and classical Monte-Carlo technique for vizualization of past tracks of vacancies imprinted within Fe-containing silicate minerals such as olivine and pyroxene. We have considered olivine as an example because it is computationally more tractable because of the comparatively smaller size of its unit cell as compared to other minerals in this class.

This chapter is based on *EPL* **98**, 29001 (2012)

6.1 Introduction

Olivine mineral as already stated, has a general formula M_2SiO_4 , M being a divalent cation. The unit cell is composed of SiO_4 tetrahedral units, which are arranged such that they produce two types of octahedral voids differing in geometry, named as M1 and M2, which are partially occupied by metal cations. For the present study we focus on Fe-Mg olivine. From geological studies on olivines [3], it is well known that, on a macroscopic scale, vacancies become fully mobile only above 1300⁰C. Therefore, they are in a non-equilibrium state on macroscopic scale. However, within a temperature range of 1300 to 600⁰C, or so, vacancies are expected to move over shorter length scales, though such motion is not enough to equilibrate ionic occupancies[4]. It is precisely the situation we are interested in.

We have employed quantum mechanical density functional theory based simulation technique to determine local site-dependent parametrs such as : defect formation energies, site preferences of metallic ions and migration barriers for vacancy diffusion from one site to another in olivine. These parametrs in-turn act as inputs to a classical model Hamiltonian, which we use to simulate vacancy diffusion in olivine.

This Chapter is organized as follows : The next section deals with results obtained using ab-initio calculations. In this section we first present our results on vacancy formation energy at all cationic and anionic sites in olivine and the dependence of vacancy formation energy on the concentration of Fe in the olivine cell. This is followed by relative site preferences of the various chemical species such as Fe^{2+} , Fe^{3+} and Mg. In the last sub-section under section II, we report the barrier potentials for migration of vacancy. In Section III we present our 2D lattice gas model that we have devised to simulate vacancy diffusion in Fe containing olivine. In the following section, we present our results obtained after performing the Monte-Carlo simulation where we are able to indirectly vizualize the path of vacancy migration. Finally we conclude the chapter withn a brief summary of our results and also propose possible experimantal verification of our findings.

6.2 *Ab-initio* Results

6.2.1 Vacancy formation energy at all cationic and anionic sites and its dependence on Fe-content

We have carried out calculations of vacancy formation energies at all sites for both iron-free and iron bearing olivines, though the focus of our study will be on iron-bearing olivines. Similar calculations have been reported in literature[5] for Fe-free end member, Mg_2SiO_4 . The vacancy formation energy, as already mentioned previously, is obtained by subtracting the total energy of the vacancy-free structure from the sum of the energies of the vacancy bearing structure and the energy of the atom in isolation at which vacancy is created. Due to the presence of defect charges(q) in certain cases, defect-defect correction of the form $E(\text{correction}) = \alpha q^2 / \epsilon L$ is included, where α is the Madelung constant, L is the cell length, and ϵ is the dielectric constant. Fig. 6.1 shows the vacancy formation energies at various cation and anion sites, measured with respect to the formation energy at M1 site, the site at which the vacancy is formed most easily, for both iron-free and iron-bearing olivines. For iron-free olivine or Mg_2SiO_4 , the order in which vacancy prefers to be created at various sites is found to be $M1 > O3 > M2 > O2 > O1 > Si$. This trend is consistent with the results obtained[6] based on simulations using classically derived potential parameters. Upon introduction of Fe, the trend is found to be altered to $M1 > M2 > O3 > O2 > O1 > Si$. What is remarkable is that, upon introduction of Fe, vacancy is formed with much greater ease at M1 site compared to other sites, the formation energy at M1 site being smaller by 2-3 eV compared to other sites. The relative ease at which vacancy is formed at M1 site increases with increasing concentration of Fe, as is shown in Fig. 6.1, considering two different concentrations of Fe 25% and 50%, and formation energy differences between M1 and M2.

In addition, we also find that the absolute value of the formation energy depends crucially on the Fe content. This is illustrated in the right panel of Fig. 6.1, where vacancy formation energy at M1 site, the site in which vacancy is formed with maximum ease, is plotted as a function of Fe concentration. We find that there is a sharp drop in the formation energy from about 11 eV in iron-free case to about

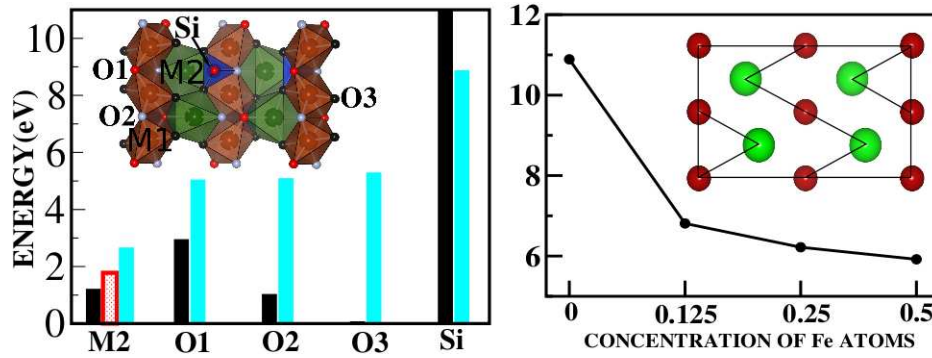


Figure 6.1 (Color online) Left panel: The vacancy formation energy at various cationic and anionic sites for iron-free as well iron-bearing olivines, measured with respect to that at M1 site. Black bar, dashed bar and cyan (light grey) bars represent iron-free olivine, iron bearing olivine with 25% Fe and with 50% Fe respectively. The inset shows the crystal structure of olivine, projected onto *bc* plane, with M1, M2, O1, O2, O3, Si sites marked. Right Panel: The vacancy formation energy at M1 site for various Fe concentrations of olivines. Inset shows the M-site only sublattice, with M1 (M2) sites marked as small (large) balls.

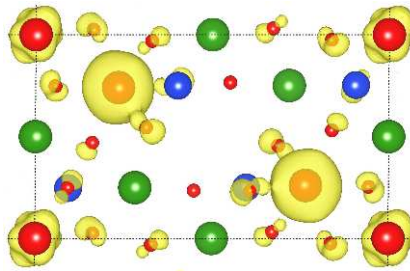


Figure 6.2 (Color online) Plot of magnetization density of olivine containing 37.5% of Fe (3 sites out of 8 M sites being occupied by Fe) and having a vacancy situated at the central M1 site of the lattice. Two of the M2 sites adjacent to vacancy as well as corner M1 sites are occupied by Fe, rest of the M sites being occupied by Mg.

7 eV by introduction of 12.5% of Fe. Upon increasing the Fe concentration further, the formation energy reduces further, attaining a value of 6 eV for 50% Fe concentration. The above analysis leads us to conclude that introduction of Fe, reduces the formation energy of vacancy substantially as well as increases the relative ease at which vacancy is formed at M1 site compared to other sites significantly.

The origin of this dramatic change in the vacancy formation energies lies in the fact that while Mg

can occur only in nominal valence 2+, both nominal valences of 2+ and 3+ are stable configurations for Fe. This causes the vacant site in Fe bearing olivine to be neutral as opposed to pure Mg olivine in which case the vacancy remains as a charged site. This is reflected in the calculated magnetic moments at Fe sites, for which we find that for each vacancy introduced in the unit cell, two of the Fe sites possess higher magnetic moments ($4-4.2 \mu_B$) compared to other Fe sites having magnetic moments in the range $3.5 - 3.8 \mu_B$. This indicates a charge disproportionation into $Fe^{+(2.5+\delta)}$ and $Fe^{+(2.5-\delta)}$ as shown in the magnetic density plot in Fig. 6.2. In the chosen configuration, shown in Fig. 6.2, the central M1 site is vacant, while two of the M2 sites adjacent to vacancy as well as corner M1 sites are occupied by Fe, rest of the M sites being occupied by Mg. We find that the magnetization density around the corner Fe sites being very different from that of the Fe's at the M2 sites, reflecting a charge disproportionated situation. Further evidence of the charge disproportionation to Fe^{2+} -like and Fe^{3+} -like valences, in the presence of vacancy, is obtained from the density of states plot projected onto different Fe sites, as presented in Fig. 6.3. The states in the majority spin channel are occupied for both the Fe sites, while in the minority spin channel, all the states are empty for one of the Fe atom and are partially occupied for the other Fe atom, establishing Fe^{3+} -like and Fe^{2+} -like valences of the two atoms respectively.

The oxygens connected to Fe atoms at M2 site also exhibit different magnetic moments compared to those connected to Fe atoms at corners due to large Fe-O covalency.

6.2.2 Relative site preference of Fe^{2+} , Fe^{3+} and Mg

In the next step, we decide on the relative site preferences of the different chemical ions at various M sites, by calculating total energies of various configurations. Fig. 6.3 summarizes all the results. The left most panel shows calculations for 25% of Fe in an unit cell, so that 2 sites out of 8 M sites in the unit cell are occupied by Fe, which upon introduction of vacancy at the M1 site, selected at the centre of the box, transforms to be Fe^{3+} like state with a magnetic moment of $\approx 4.2 \mu_B$. Comparison of the total energies between the configuration shown in top with Fe atoms occupying M1 sites and that shown in bottom with Fe atoms occupying M2 site shows that it is energetically preferable for Fe^{3+} like ions to occupy M2 site compared to M1 site by an energy of about 250 eV per Fe. For M2

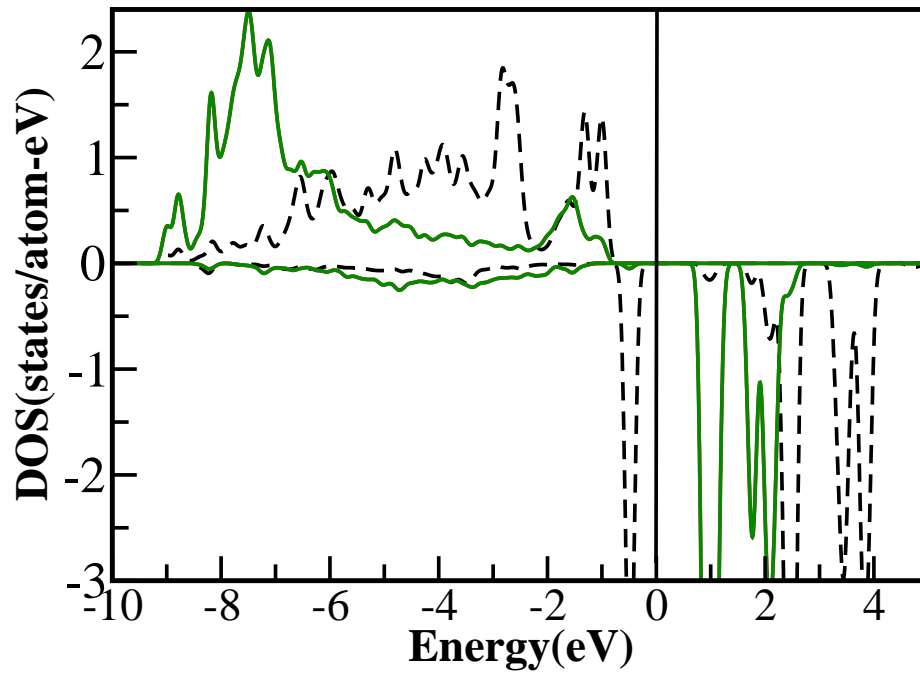


Figure 6.3 The spin-polarized density of states projected onto d -states of the Fe atom sitting at the M2 site(solid line) and that projected onto d -states of the Fe atom sitting at M1 site(dashed line). The partial densities of states are calculated by projecting onto a sphere of radius 1.302 Å for both the Fe sites.

sites, there are two possible ways in which it can be occupied by two Fe's, either at sites belonging to same chain (shown in top of the middle panel), another at sites belonging to different chains (shown in bottom of the middle panel). We note that in the former situation, the Fe³⁺ like ions are separated from the vacant site by a distance of ≈ 3.26 while for the later they are separated by a distance of ≈ 3.62 . Comparison of total energies shows that the former is preferable by an energy of 20 meV per Fe, indicating Fe atoms closest to vacancy transform to Fe³⁺-like valence. Finally, in the right panel, we consider the situation where three Fe atoms are present, two of them exhibiting Fe³⁺-like valence and one exhibiting Fe²⁺-like valence. Total energy calculations carried out considering Fe²⁺-like ion placed at M1 site as opposed to M2 sites, shows the former to be more stable by an energy of 24 meV. The above results put together indicates preference of Fe²⁺-like ions at M1, Fe³⁺-like at M2 and at the sites closest to vacant site which itself shows a preference of M1 site, while the Mg²⁺ ions have negligible site preference (confirmed by separate calculations). The preference for Fe²⁺-like ions at M1 and Fe³⁺-like at M2 has been discussed previously.[10]

6.2.3 Calculation of barrier potential

In order to simulate diffusion, one last piece of vital information in addition to the ones determined till now is the numerical values of the barrier potential that the vacancy has to face while moving from one site to the other. We considered a 50:50 olivine with 50% of Fe and 50% of Mg and considered the propagation of a single vacancy. The M sites are populated with Fe and Mg ions according to their preferences as determined in the previous section. A single vacancy is considered at one of the central M1 site within a two unit cell super-cell containing 8 f.u., as shown in Fig. 6.4. The Fe atoms placed at M2 sites, sitting next to vacancy are 3+ like while rest of the Fe atom within the cell are 2+ like. There are several possible paths between all adjacent M sites in the olivine structure. It is shown previously that the migration of vacancy in olivine is fastest along [001] direction with smallest barrier height. Following this idea we first considered the propagation of vacancy from M1 site to a neighbouring M1 site along [001] direction with initial and final configurations as shown in Fig. 6.4. The barrier height was computed employing nudged elastic band (NEB) method[7] using five different images other than

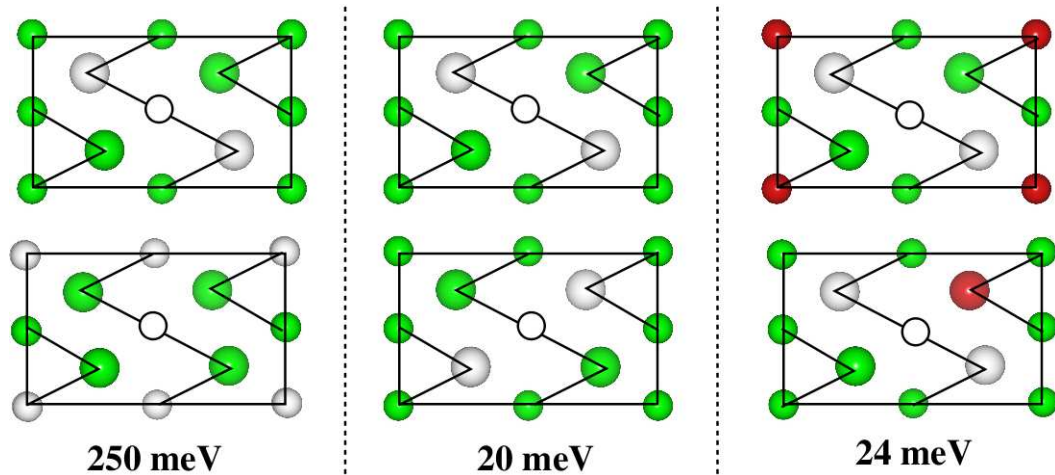


Figure 6.4 (Color online) Site preferences of Fe^{2+} -like and Fe^{3+} -like ions in olivine in presence of a single vacancy in the 4 f.u. unit cell. The vacant site is indicated by an empty circle, the Mg atoms by green (light grey), Fe^{3+} -like atoms by white and Fe^{2+} -like atoms by red (dark grey) balls. Left panel: Configurations with 2 Fe^{3+} -like ions at M2 (top) and M1 (bottom) sites. Middle panel: Configurations with 2 Fe^{3+} -like ions at M2 sites near (top) and far (bottom) to vacant site. Bottom panel: Configurations with 2 Fe^{3+} -like ions at M2 sites and a Fe^{2+} -like ion at M1 (top) and M2 site (bottom) site. The energy difference between bottom and top configurations are listed at the bottom of each panel.

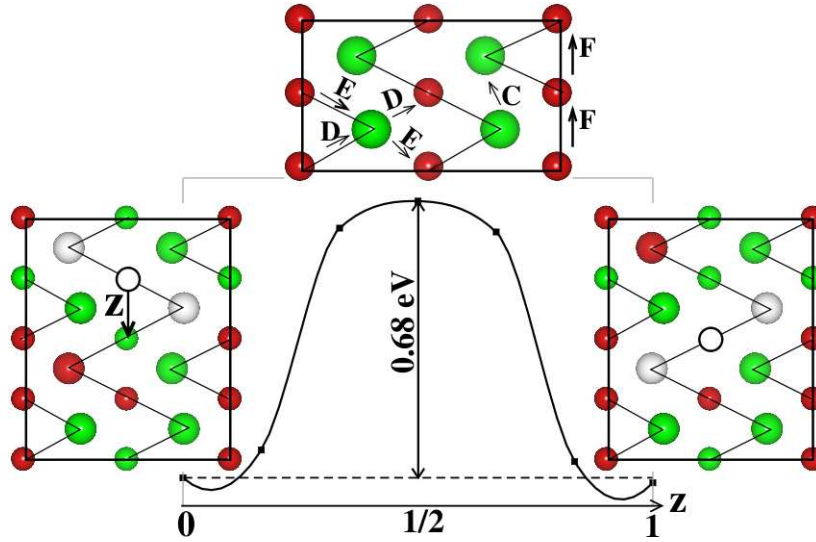


Figure 6.5 Barrier height of vacancy propagation along [001] direction in a 50:50 Fe-Mg olivine, as obtained in a NEB calculation. The initial and final configurations are shown in left and hand insets, respectively. Various paths of vacancy propagation (except A and B which are perpendicular to the plane of the figure) are shown in the top inset.

the initial and final image. The barrier height came out to be about 0.68 eV which is very similar to that obtained for pure Mg olivine.[5] This leads us to conclude that introduction of Fe although influences the vacancy formation energy significantly, its influence on the barrier height is minimal. The barrier heights considering other paths, e.g, between two M1 sites along [100] direction (A), between two M2 sites along [100] direction (B), that between two M2 sites within [001] planes, migration connecting M1 and M2 sites (D and E) are found to be about 8, 12, 2, 3 and 6 times larger than the barrier height for propagation connecting two M1 sites along [001] direction.

6.3 The 2D lattice gas model and the Monte-Carlo simulation.

Based on the results of our quantum chemical calculations, we introduced a 2D lattice gas model which we studied by means of Monte Carlo technique.[8] We model the site preference of various metallic ions in a 2D M-only lattice (cf right inset in Fig. 6.1) within a spin-like model. We considered a pseudo-spin variable $S_i = +1$ (-1) for Fe(Mg). $S_i = 0$ denotes vacant site. The fact that Fe can have 2+

or 3+ -like valence with two different site preferences, is taken care of by introducing another variable ξ_i , which can take values +1 (-1) for Fe sites of valences 2+ -like (3+ -like) and otherwise is +1. A model Hamiltonian involving the above defined pseudo-spins can then be written as follows:

$$H = J \sum_{i,j \in NN} S_i S_j + D \sum_i (1 - S_i^2) - h \sum_i S_i - h_s \left[\sum_{i \in M1} f_i(S_i, \xi_i) - \sum_{i \in M2} f_i(S_i, \xi_i) \right]$$

where the summation in the forth term extends over M1 and M2 sublattices, for the rest of the terms the summation extends over all the sites in the lattice. The function f_i takes values $+a/-a$ for $(S_i, \xi_i) = (+1,+1)/((+1,-1)$, b for $S_i = 0$ and 0 for $S_i = -1$. $h_s a$ and $h_s b$ therefore governs the strong site preference exhibited Fe and vacancy, respectively. J is the chemical interaction between first nearest neighbors (NN), h gives the difference of chemical potentials between Fe and Mg. The chemical potential for vacancy is given by the parameters in D . The unknown parameters in the model Hamiltonian, H , are obtained by mapping the DFT total energies for various different configurations with different arrangements of occupations of M1 and M2 sites by Fe, Mg and vacancy onto H . Such an approach has been proved to be successful in studying crossover partitioning problem in olivine.[11] We started with some initial distribution of Fe and Mg atoms at sites on a 2D M-only lattice and studied the evolution of vacancy propagation using Monte Carlo algorithm. During the Monte Carlo move, the vacancy propagation from one site to a neighboring site, is determined by the site-specific vacancy formation energy and the migration barrier, and comparing to the Boltzmann factor. In the above sense, this is different from standard Metropolis algorithm, for which only the energy difference between initial and final states matters.

6.4 Vizualization of vacancy track.

Using the 2D lattice gas model as presented in the previous section we next try to simulate the diffusion of a single vacancy in the body of the olivine crystal. The results of such a simulation is highly interesting. The vacancy, as is shown in the detailed quantum chemical calculations, transforms valences of neighboring Fe atoms to Fe³⁺-like valences, which makes up for the charge depletion concomitant with

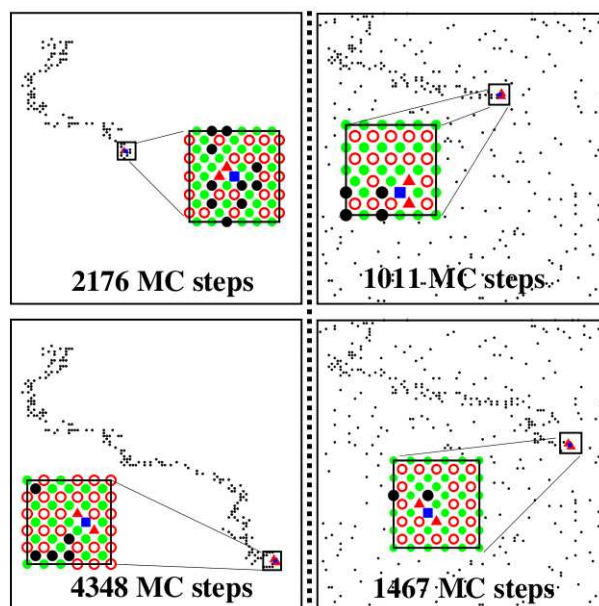


Figure 6.6 (Color online) Snapshots of M-only lattice at two different MC step. Shown are only positions of wrong Fe sites. The region around the vacancy, marked with a box, is shown in the zoomed view with all M sites shown explicitly. The green and black balls denote positions of Mg and Fe^{2+} like ions at wrong (M2) sites, respectively. The red (dark grey) annular rings indicate Fe^{2+} like ions at M1 while the triangle and square indicate the positions of Fe^{3+} like ions and vacancy, respectively. Left panels: For perfectly ordered starting configuration. Right panels: Partially ordered starting configuration.

the removal of a metallic ion. The Fe^{3+} -like ions due to its strong site preference tend to occupy M2 sites, which otherwise is a *wrong* site for Fe with its nominal valence of 2+. As the vacancy diffuses away from the neighborhood, the Fe^{3+} -like sites transform back to Fe^{2+} -like sites, since Fe^{3+} -like sites also show preference to be close to vacant site. As a result, Fe atoms, now in its 2+-like valence, remain stranded in an unfavorable position, since there is no scope for Fe atom to return to its favorable location, M1, which is not vacant anymore. The vacancy, therefore, leaves behind a series of wrong Fe sites (Fe atoms occupying M2 sites) as it propagates through the lattice, which forms a trace of its propagation track. Visualization of such a track, requires distinction of M1 and M2 sites as well as detection of chemical species at a given site. Understandably, visualization of the track is most clean, if one starts from a perfectly ordered case with all Fe (Mg) atoms occupying M1(M2) sites as shown in left panels in Fig. 6.5, for a simulation on a 200×200 lattice with 50% Fe occupancy. Starting with partially ordered situation with wrong Fe sites to start with, makes the visualization difficult, though wrong Fe sites produced by vacancy propagation would have a distinct track-like feature, while the other wrong Fe sites would be randomly distributed. Such a scenario is shown in right panels of Fig. 6.5, where the initial configuration was chosen such that it had 250 wrong Fe sites out of total 1000 Fe sites. Increasing disorder makes the detection of vacancy track (“signal”) from the randomly occupied sites due to disorder (“noise”) difficult.

While we have used the example of olivine to illustrate our point in this Letter, a similar situation is expected to prevail in pyroxene. Since in pyroxene site disorder of Fe and Mg occupancy is smaller than olivine due to the larger energy differences,[10] we expect detection of vacancy tracks to be even easier.

6.5 Summary and possible experimental verification

In summary, the present study shows: (a) the presence of vacancy creates Fe^{2+} -like and Fe^{3+} -like ions which have two different site preferences, with Fe^{3+} -like ions occupying sites closest to vacancy (b) presence of Fe substantially enhances the preference of vacancy formation at M1 site, and most

importantly it proposes (c) creation of wrong sites as the trail of the vacancy as it passes by. The creation of trail of wrong sites enables to track the vacancy path, thereby offering an alternative way of visualizing point defects. Note, though the site preference problem in olivine, has been studied earlier,[10] those were either in absence of vacancy or carried out in pure Fe system, therefore did not had the interesting situation of mixed valency and creation of wrong sites, as in the present case.

We believe that tracks such as those shown in Fig.6.6 should be observable in experiment where one needs to (a) distinguish between Fe and Mg, which have distinct electron energy loss spectroscopy (EELS) obtained spectra,[12] and (b) determine whether Fe is at an M1 or M2 site; a feat which is achievable using present day high-resolution transmission electron microscopy (HRTEM) techniques. Though this is a challenging experiment, but forms an emerging field in experimental science and observation of such tracks have been already attempted in the context of other systems. For example, the study[13] by Gao *et. al* on binary oxide, imaged the structure change during oxygen vacancy migration in CeO₂ induced by electric field using HRTEM. Further, the EELS experiments were carried out to show the change of chemical valence of the Ce ions. The application of such approach to olivine will be certainly a worthwhile experiment to carry out.

Bibliography

- [1] N. Wax, *Selected Papers on Noise and Stochastic Processes* (Dover Pubns., New York 1954).
- [2] R. Das *et al.*, PLoS Computational Biology, 5, e1000556, (2009).
- [3] A. Putnis (1992) *An introduction to mineral sciences* Cambridge Univ Press, Cambridge.
- [4] R. N. Schock *et al.*, J Geophys Res-Solid, 94, 5829, (1989); R. Heinemann *et al.*, Eur. J. Mineral. **19**, 15 (2007).
- [5] A. M. Walker *et al.* Phys. Earth Plan. Inter. **172** 20 (2009); F. Bejina *et al.* Phys. Earth Plan. Inter. **172** 13 (2009).
- [6] N.C. Richmond, J.P. Brodholt, Am. Mineral. **85**, 1155 (2000)
- [7] G. Henkelman *et al.*, J. Chem. Phys. **113** 9901 (2000); G. Henkelman and H. Jonsson, *ibid*, **113** 9978 (2000).
- [8] K. Binder and W. Heermann Monte Carlo Simulation in Statistical Physics: An Introduction, Springer (2002).
- [9] P. Kratzer, arXiv:0904.2556v1
- [10] S. Chatterjee *et al.*, Phys. Rev. B **79**, 115103 (2009); S. Chatterjee and T. Saha-Dasgupta, Phys. Rev. B **81**, 155105 (2010).
- [11] S. Chatterjee *et al.*, Phys Chem Miner. **38** 259 (2011).

- [12] H. Shuman, *Ultramicroscopy* **6** 163 (1981); P.A. van Aken *et al.*, *Phys Chem Minerals* **25** 323 (1998).
- [13] Gao *et. al.* *Micron* 41, 301 (2010).

Chapter 7

Conclusion and scope for future study.

The main aim of this thesis was to study the structural, electronic and magnetic properties of silicate minerals, using first principles density functional theory and also to simulate properties involving longer time-scales, such as the equilibration and diffusion properties using classical Monte-Carlo technique.

The silicate mineral which we have mostly paid attention to is olivine. This is because it has a comparatively simpler structure and hence easier to simulate. The other interest we had in examining this mineral was to give a theoretical explanation to the various disputes in the experimental community revolving around certain properties of this mineral. We have also studied pyroxene to a lesser extent, which happens to be a major constituent of the upper mantle of the earth along with olivine.

A similarity between olivine and pyroxene is that, they both have two different octahedral sites, namely M1 and M2, which are partially occupied by cations. Although these cations may be of different kinds, we have paid special attention to Fe containing Mg-olivine and Mg-pyroxene. This is because Fe being a transition metal ion, has very high electron-electron correlation and may appear in more than one oxidation state. These properties may bring about drastic effects in the properties of these minerals. We would like to stress here that most of the theoretical results reported till date are dedicated to Fe-free olivine. But we have consistently involved Fe in our calculation, because natural olivine contains about 12.5 % of Fe and we believed and also proved that presence of Fe can make a big difference in the properties of the olivine mineral. Hence, to be able to compare theoretical results and experimental

findings, one should incorporate Fe into the system.

This thesis is divided into two parts. The first two projects (chapter 3 and chapter 4) are dedicated to defect-free silicate minerals. In the next two chapters (chapter 5 and chapter 6) we have studied the effect of vacancy on Fe containing silicate minerals.

In the following we summarize the major findings of the present thesis.

(a) Site preference of Fe in olivine and pyroxene

In this project, we found the important role played by co-valency in determining the site preference of Fe in olivine and pyroxene. As discussed in great details in chapter 3, M1 and M2 are the two sites which are the contenders for hosting Fe. The two main properties of these octahedra, that help in deciding the site preference are, their size/volume and the corresponding covalency of Fe in these sites. We find that in the case of pyroxene, both size and co-valency work hand in hand to make Fe prefer M2 site. This has also been observed experimentally and hence helps put our theory on firm footing. When we extend this theory to the case of olivine, where site preference of Fe is somewhat disputed, we find that size-wise Fe prefers M2 site, whereas the Fe-O co-valency is larger at M1 site. Since the size difference between M1 and M2 is not significant, co-valency wins and Fe prefers to sit at M1 site in the case of olivine.

(b) Temperature dependence of site preference of Fe in olivine

It has long been debated among experimental groups, whether the site preference of Fe changes beyond a certain temperature. We have tried to resolve this issue using a combination of first principles density functional calculation and classical Monte-Carlo technique. We have proposed a model Hamiltonian in this regard, the parameters of which were obtained from DFT calculation. Our calculation finds that there is a strong preference of Fe for M1 site at very high and very low temperatures. This is because the M1 and M2 octahedral volumes are similar at these temperatures and hence co-valency has a stronger effect. At intermediate temperatures, around 600⁰ C, the difference between M1 and M2 becomes significant, that gives a tough competition to co-valency. However, no-where in the whole temperature range does the size difference between M1 and M2 become so large as to create a "cross-over".

(c) Structural, electronic and magnetic properties of vacancy bearing Fe silicates

Charge disproportionation and ordering are the two phenomena that has intrigued physicists for a long time. In this project, we have theoretically investigated using quantum mechanical density functional based tools, a mineral which is compositionally close to the laihunite structure found naturally, by introducing appropriate number of vacancies at the cationic sites of Fe_2SiO_4 . Our theoretically developed structure very well mimics the reported trends in structural changes on introduction of vacancy, hence showing that our theory is capable of reproducing results involving very complicated defect structures of minerals. Incorporation of vacancy leads to some of the Fe in its nominal 2+ oxidation state to change to nominal 3+ oxidation state, in order to maintain the overall charge neutrality of the system. Our calculations find that these two different species of Fe prefer two different octahedral sites, leading to charge ordering. We have further studied the underlying magnetic order.

(d) Visualizing frozen point defect tracks in Fe containing silicate minerals. Vacancy migration tracks contain a wealth of information, but its direct, *in situ* determination is a challenging task. Here, we have developed a method for indirect determination of the imprints of vacancy migration track in the case of Fe containing silicate minerals. With the introduction of vacancy, two of Fe^{2+} sitting in the neighborhood of the vacancy change valence to nominal 3+, in order to maintain over-all charge neutrality. The crystal now has two different species of Fe, in nominal 2+ and 3+ oxidation states, which were found to have two different site preferences, Fe^{2+} preferring M1 and Fe^{3+} preferring M2. Our calculations found that vacancy- Fe^{3+} system move together as a cluster in the crystal, i.e, as the vacancy migrates, it converts two of the nearest Fe^{2+} to 3+ state, which has a preference for M2 site. Now as the vacancy diffuses away, these Fe^{3+} now sitting in the M2 site, convert back to Fe^{2+} which although prefers M1 site are stuck up in unfavorable M2 site. Hence the trail of the vacancy diffusion track appears in the form of Fe^{2+} stuck at wrong M2 site.

7.1 Scope for future work

This thesis presents initial results of our venture into the world of geo-sciences, using combined ab-initio and classical simulation tools. We have addressed only a few interesting problems, which leaves a lot of scope for future work. To mention a few :

In our project on temperature dependence of site preference of Fe in olivine, we have borrowed the crystal structure data of olivine at different temperatures from Redfern *et al.* and Heinemann *et al.*. The ideal situation would be the one where we had simulated our own structure at different temperatures. This could be done either classically or quantum mechanically. For a classical simulation, we require good force fields which should capture the very delicate co-valency Fe-O effect in addition to other properties. Such a kind of force field does not exist in the literature, and the development of one such would be invaluable in the study of olivine mineral. A quantum mechanical approach would require performing Car-parinello molecular dynamics simulation, which although very expensive, may be attempted. Since the site preference of Fe at each temperature has a dependence on the crystal structure, it would be nice if we can generate our own crystal structure making the calculations completely independent of experiments which will also enable us to comment on the thermodynamic and elastic properties of the olivine crystal.

As an extension to the vacancy diffusion problem, the diffusion of Li can be investigated, which is a tracer element, in olivine. The similarity between vacancy and Li is that, they both are deficit of charge, vacancy by +2 and Li by +1, when they sit in the cationic sites meant for divalent cations like Mg^{2+} and Fe^{2+} . As a result they change the valence of Fe atoms in their neighborhood to maintain the overall charge neutrality. Li being small in size is attributed with the property that it may migrate through both interstitial sites and cationic sites.

In the whole thesis we have paid our attention to olivine crystal structure only, in addition to pyroxene. These two minerals as stated earlier are the major constituents of the upper mantle of the earth. As we go deeper down, because of the increase of pressure, the atoms in these minerals re-arrange themselves to give rise to denser packing. It would be worthwhile to study the effect of pressure and

hence the elastic properties of these mineral structures.

Mineral named wadsleyite is reported to hold a lot of water, and may co-exist with a hydrous melt at transition zone pressure-temperature conditions. This mineral is found in the lower mantle and is a high-pressure polymorph of olivine. Compared to olivine, this silicate mineral has three kinds of octahedral units named M1, M2 and M3 and the SiO_4 tetrahedral units appear in pairs. The microscopic origin of its large water retention capacity, would be interesting to study.